

AD-A039 346

NAVAL POSTGRADUATE SCHOOL MONTEREY CALIF

F/G 8/3

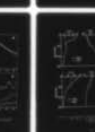
THE ROLE OF STRONG ATMOSPHERIC FORCING EVENTS IN THE MODIFICATI--ETC(U)

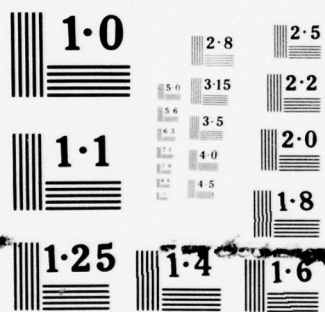
DEC 76 N T CAMP

UNCLASSIFIED

NL

1 OF 2
ADA
039346





NATIONAL BUREAU OF STANDARDS
MICROCOPY RESOLUTION TEST CHART

AD A 039346

2 (2)

NAVAL POSTGRADUATE SCHOOL

Monterey, California



THESIS

THE ROLE OF STRONG ATMOSPHERIC FORCING
EVENTS IN THE MODIFICATION OF THE UPPER OCEAN
THERMAL STRUCTURE DURING THE COOLING SEASON

by

Norman Thomas Camp

Department of Oceanography

December 1976

Thesis Advisor:

R. L. Elsberry

Approved for public release; distribution unlimited.

AD No. _____
DDC FILE COPY



REPORT DOCUMENTATION PAGE		READ INSTRUCTIONS BEFORE COMPLETING FORM
1. REPORT NUMBER	2. GOVT ACCESSION NO.	3. RECIPIENT'S CATALOG NUMBER
4. TITLE (and Subtitle) The Role of Strong Atmospheric Forcing Events in the Modification of the Upper Ocean Thermal Structure during the Cooling Season.		5. TYPE OF REPORT & PERIOD COVERED Ph.D. Dissertation December 1976
7. AUTHOR(s) 10 Norman Thomas Camp		6. CONTRACT OR GRANT NUMBER(s) 9 Doctoral thesis,
9. PERFORMING ORGANIZATION NAME AND ADDRESS Naval Postgraduate School Monterey, California 93940		10. PROGRAM ELEMENT, PROJECT, TASK AREA & WORK UNIT NUMBERS
11. CONTROLLING OFFICE NAME AND ADDRESS Naval Postgraduate School Monterey, California 93940		12. REPORT DATE 11 December 1976
14. MONITORING AGENCY NAME & ADDRESS (if different from Controlling Office) Naval Postgraduate School Monterey, California 93940		13. NUMBER OF PAGES 175
		15. SECURITY CLASS. (of this report) Unclassified
16. DISTRIBUTION STATEMENT (of this Report) Approved for public release; distribution unlimited.		15a. DECLASSIFICATION/DOWNGRADING SCHEDULE 12 173p.
17. DISTRIBUTION STATEMENT (of the abstract entered in Block 20, if different from Report)		
18. SUPPLEMENTARY NOTES		
19. KEY WORDS (Continue on reverse side if necessary and identify by block number) Mixed layer Extratropical cyclone Thermal structure Entrainment Sea-surface temperature Turbulent kinetic energy Mixed-layer models Non-penetrative convection		
20. ABSTRACT (Continue on reverse side if necessary and identify by block number) The role of strong atmospheric forcing events in determining the evolution of the upper ocean during the fall and early winter cooling season was investigated. The historical series of surface and near-surface marine observations at three mid-latitude ocean weather ships [PAPA (OWS P), NOVEMBER (OWS N), and VICTOR (OWS V)] support the hypothesis that the integrated effects of these events dominate this evolution. For example, periods when the mechanical		

cont

→ forcing was greater than the long-term mean accounted for approximately 35% of the time in the record examined at the three stations. However 85%/68%/57% of the sea-surface temperature change at OWS N/OWS P/OWS V occurred during these periods.

Forty-nine data sets were examined and modeled during periods of intense fall and winter forcing. The significant thermal structure modifications observed during these strong events were simulated successfully using three modifications of the Kraus and Turner (1967) one-dimensional model. Evidence is presented which demonstrates that the amount of mechanically-generated turbulent kinetic energy available for entrainment decreases as the mixed-layer depth increases. Furthermore, in agreement with Gill and Turner (1976), these case studies suggest that only a small percentage of the convectively-generated turbulent kinetic energy is available for increasing the potential energy of the ocean by entrainment.

ACCESSION for	
RTS	White Section <input checked="" type="checkbox"/>
DOC	Butt Section <input type="checkbox"/>
UNANNOUNCED	<input type="checkbox"/>
JUSTIFICATION	
BY	
DISTRIBUTION/AVAILABILITY CODES	
Dist.	AVAIL. AND/OR SPECIAL
A	.

The Role of Strong Atmospheric Forcing
Events in the Modification of the Upper Ocean
Thermal Structure During the Cooling Season

by

Norman Thomas Camp
Lieutenant Commander, United States Navy
B.Ed., Rhode Island College, 1962
M.S., Naval Postgraduate School, 1972

Submitted in partial fulfillment of the
requirements for the degree of

DOCTOR OF PHILOSOPHY

from the

NAVAL POSTGRADUATE SCHOOL
December 1976

Author

Norman Thomas Camp

Approved by:

Dale F. Leipper

D. F. Leipper
Professor of Oceanography
Committee Co-Chairman

R. L. Elsberry

R. L. Elsberry
Assoc. Professor of Meteorology
Committee Co-Chairman
Thesis Advisor

R. G. Paquette

R. G. Paquette
Professor of Oceanography

C. Cornstock

C. Cornstock
Professor of Mathematics

J. J. von Schwind

J. J. von Schwind
Assoc. Professor of Oceanography

E. B. Thornton

E. B. Thornton
Assoc. Professor of Oceanography

R. H. Bourke

R. H. Bourke
Asst. Professor of Oceanography

R. L. Haney

R. L. Haney
Assoc. Professor of Meteorology

Approved by:

Dale F. Leipper

Chairman, Department of Oceanography

Approved by:

Jack R. Burdick

Academic Dean

ABSTRACT

The role of strong atmospheric forcing events in determining the evolution of the upper ocean during the fall and early winter cooling season was investigated. The historical series of surface and near-surface marine observations at three mid-latitude ocean weather ships [PAPA (OWS P), NOVEMBER (OWS N), and VICTOR (OWS V)] support the hypothesis that the integrated effects of these events dominate this evolution. For example, periods when the mechanical forcing was greater than the long-term mean accounted for approximately 35% of the time in the record examined at the three stations. However 85%/68%/57% of the sea-surface temperature change at OWS N/OWS P/OWS V occurred during these periods.

Forty-nine data sets were examined and modeled during periods of intense fall and winter forcing. The significant thermal structure modifications observed during these strong events were simulated successfully using three modifications of the Kraus and Turner (1967) one-dimensional model. Evidence is presented which demonstrates that the amount of mechanically-generated turbulent kinetic energy available for entrainment decreases as the mixed-layer depth increases. Furthermore, in agreement with Gill and Turner (1976), these case studies suggest that only a small percentage of the convectively-generated turbulent kinetic energy is available for increasing the potential energy of the ocean by entrainment.

TABLE OF CONTENTS

I.	INTRODUCTION - - - - -	13
A.	PURPOSE OF THE STUDY - - - - -	13
B.	FUNDAMENTAL HYPOTHESIS - - - - -	14
C.	SPECIFIC OBJECTIVES OF THE STUDY - - - - -	14
D.	OVERVIEW OF THE THESIS - - - - -	16
II.	REVIEW OF MIXED LAYER MODELING THEORIES - - - - -	17
A.	GOVERNING EQUATIONS - - - - -	17
B.	THE ONE-DIMENSIONAL HYPOTHESIS - - - - -	19
C.	TURBULENT FORM OF THE BASIC EQUATIONS - - - - -	20
D.	THE BULK MODEL HYPOTHESIS - - - - -	22
E.	BOUNDARY CONDITIONS - - - - -	25
F.	THE INTEGRATED MASS, MOMENTUM, AND ENERGY BUDGETS - - - -	27
G.	CLASSES OF MIXED LAYER MODELS - - - - -	32
	1. The Prototype Turbulent Bulk Model - - - - -	32
	2. The Prototype Inertial Bulk Model - - - - -	34
H.	NON-PENETRATIVE FREE CONVECTION - - - - -	36
I.	DISSIPATION ENHANCEMENT - - - - -	39
J.	VERTICAL DIFFUSION - - - - -	41
K.	SALINITY EFFECTS - - - - -	42
III.	CHARACTERISTICS OF THE ATMOSPHERIC FORCING AND OCEANIC RESPONSE AT OCEAN WEATHER SHIPS (OWS) PAPA (P), NOVEMBER (N), AND VICTOR (V) - - - - -	43
A.	DATA SOURCES - - - - -	43
B.	FORMULAS FOR COMPUTING ATMOSPHERIC FORCING - - - - -	44
C.	CHARACTERISTIC ATMOSPHERIC AND OCEANIC CONDITIONS AT THE WEATHER STATIONS - - - - -	45

IV.	RESPONSE OF THE UPPER OCEAN TO STRONG ATMOSPHERIC FORCING: OBSERVATIONS AND SIMULATIONS - - - - -	51
A.	INTRODUCTION - - - - -	51
B.	PARAMETERIZATION OF THE MODELS - - - - -	52
C.	INPUT DATA - - - - -	53
D.	CHARACTERISTICS OF THE ATMOSPHERIC FORCING AND OCEANIC RESPONSE AT OWS P - - - - -	56
E.	IMPORTANCE OF NON-PENETRATIVE CONVECTION - - - - -	83
F.	IMPORTANCE OF NON-LOCAL EFFECTS - - - - -	91
G.	RELATIVE PERFORMANCE OF THE EFT, KT, AND KIM MODELS AT OWS P, OWS N, AND OWS V - - - - -	96
H.	RELATIVE IMPORTANCE OF THE SURFACE AND ENTRAINMENT HEAT FLUXES - - - - -	104
V.	ROLE OF STRONG ATMOSPHERIC FORCING EVENTS IN THE SEASONAL EVOLUTION OF THE UPPER OCEAN - - - - -	108
A.	INTRODUCTION - - - - -	108
B.	CHARACTERISTICS OF THE MARINE ATMOS- PHERE AT THE OCEAN WEATHER STATIONS - - - - -	108
C.	COMPARISON OF THE LONG-TERM MEAN FORCING AND OCEANIC RESPONSE AT THE OCEAN WEATHER STATIONS - - - - -	122
D.	IMPORTANCE OF LARGE ATMOSPHERIC FORCING EVENTS IN DETERMINING THE SEASONAL EVOLUTION OF THE MIXED LAYER - - - - -	131
E.	IMPORTANCE OF THE STRONG ATMOSPHERIC FORCING EVENTS AT THE THREE OCEAN WEATHER STATIONS - - - - -	141
VI.	CONCLUSIONS - - - - -	155
	APPENDIX A COMPUTATIONAL FORMULAS FOR SURFACE FORCING - - - - -	160
	APPENDIX B THE NUMERICAL SCHEME FOR THE ONE-DIMENSIONAL TURBULENT BULK MODELS - - - - -	164
	BIBLIOGRAPHY - - - - -	170
	INITIAL DISTRIBUTION LIST - - - - -	173

LIST OF TABLES

Table		
2-1	R_i^* as a function of wind speed (U_{10}) and initial layer depth (h_o) - - - - -	37
3-1	Availability of data at the ocean weather stations - - - -	43
4-1	Model and data comparison at OWS P for the period 7-19 October 1954 - - - - -	66
4-2	Same as Table 4-1 except for the period 22 November - 12 December 1957 - - - - -	73
4-3	Same as Table 4-1 except for the period 1-15 September 1966 - - - - -	80
4-4	Same as Table 4-1 except for OWS V during the period 7-19 October 1963 - - - - -	89
4-5	Comparison of mean and RMS errors of the models at the three ocean weather stations - - - - -	100
4-6	Comparison of MLT predictions by the EFT model at the ocean weather stations - - - - -	103
5-1	Statistical characteristics of the histograms of wind (u_*), turbulent kinetic energy (u_*^3), and turbulent heat flux (Q_a) - - - - -	112
5-2	Variability of atmospheric and oceanic parameters at OWS P - - - - -	114
5-3	Same as Table 5-2 except for OWS V - - - - -	115
5-4	Same as Table 5-2 except for OWS N - - - - -	116
5-5	Long-term mean forcing and mixed layer response at OWS P (24 year average) - - - - -	123
5-6	Same as Table 5-5 except for OWS V (15 year average) - - - - -	124
5-7	Same as Table 5-5 except for OWS N (23 year average) - - - - -	125

5-8	Atmospheric forcing and response at OWS P for the years 1959 and 1963 - - - - -	136
5-9	Atmospheric forcing and sea-surface temperature response at OWS P - - - - -	145
5-10	Same as Table 5-9 except for OWS V - - - - -	146
5-11	Same as Table 5-9 except for OWS N - - - - -	147
5-12	Characteristic forcing and response during events with peak-to-mean ratios greater than 1.0 - - - - -	149
5-13	Same as Table 5-12 except for peak-to-mean ratios greater than 1.5 - - - - -	150
5-14	Same as Table 5-12 except for peak-to-mean ratios greater than 2.0 - - - - -	151

LIST OF FIGURES

Figure		
2-1	Schematic of the oceanic mixed layer - - - - -	23
3-1	Long-term mean atmospheric forcing and oceanic thermal response at OWS P, OWS V, and OWS N - - - - -	47
3-2	Major features of the ocean thermal structure in the North Pacific. (A) Pacific Subarctic Region (B) Pacific Subtropic Region (after Tully, 1964) - - - - -	48
4-1	Atmospheric forcing and observed and predicted mixed layer response at OWS P during the period 7-19 October 1954 - - - - -	58
4-2	Observed and predicted (EFT model) thermal structure for the period 7-19 October 1954, with vertical diffusion neglected ($A_v = 0$) - - - - -	60
4-2a	Same as Figure 4-2 except vertical diffusion included ($A_v = .5 \text{ cm}^2 \text{ sec}^{-1}$) - - - - -	61
4-3	(A) Relative importance of the vertical heat fluxes and (B) Potential energy modifications calculated by the EFT model during the period 7-19 October 1954 - - - - -	64
4-4	Same as Figure 4-1 except for the period 22 November 1957 - 12 December 1957 - - - - -	69
4-5	Same as Figure 4-2a except for the period 22 November 1957 - 12 December 1957 - - - - -	70
4-6	Same as Figure 4-3 except for the period 22 November 1957 - 12 December 1957 - - - - -	72
4-7	Same as Figure 4-1 except for the period 1-15 September 1966 - - - - -	77
4-8	Same as Figure 4-2a except for the period 1-15 September 1966 - - - - -	78
4-9	Same as Figure 4-3 except for the period 1-15 September 1966 - - - - -	79
4-10	Values G_*-D_* normalized by $\rho_o w_*^3$ as a function of depth and wind speed for the EFT, KT, and KIM models - - - - -	82

4-11	Same as Figure 4-1 except for OWS V during the period 7-19 October 1963 - - - - -	85
4-12	Same as Figure 4-2a except for OWS V during the period 7-19 October 1963 - - - - -	86
4-13	Same as Figure 4-3 except for OWS V during the period 7-19 October 1963 - - - - -	87
4-14	Same as Figure 4-1 except for OWS N during the period 9-29 November 1965 - - - - -	92
4-15	Same as Figure 4-2a except for OWS N during the period 9-29 November 1965 - - - - -	93
4-16	Same as Figure 4-3 except for OWS N during the period 9-29 November 1965 - - - - -	94
4-17	Predicted vs. observed mixed layer depths (MLD) at OWS P - - - - -	97
4-18	Same as 4-17 except for OWS N - - - - -	98
4-19	Same as 4-17 except for OWS V - - - - -	99
4-20	Relative magnitude of the cumulative heat fluxes and total potential energy change at the three ocean stations. (A) Cumulative net surface heat flux (ΣQ_n) vs. cumulative entrainment heat flux ($\Sigma w^{TT}(-h)$) (B) Total potential energy change ($\Sigma \Delta PE$) vs. ocean heat content change (ΔH). All points calculated by EFT model for total duration of data set - - - - -	106
5-1	Histograms of wind speed (u_*) and turbulent kinetic energy flux (u_*^3) at OWS P, OWS N, and OWS V. Vertical dashed lines represent the mean of the distribution - - - - -	110
5-2	Histograms of upward turbulent heat flux (Q_a) at OWS P, OWS N, and OWS V. The vertical dashed lines represent the mean of the distribution - - - - -	111
5-3	Cumulative percentage of turbulent kinetic energy (TKE), surface cooling, and observation at OWS P, OWS N, and OWS V. (See text for explanation) - - - - -	118
5-4	Percentage of $u_*^3/Q_a/u_*$ as a function of percentage of observations - - - - -	120

5-5	Typical mid-season temperature profiles at the three ocean weather stations - - - - -	130
5-6	Mid-October temperature profile at OWS P - - - - -	133
5-7	Atmospheric forcing and oceanic response at OWS P for the 1959 cooling season - - - - -	134
5-8	Same as Figure 5-7 except for the 1963 cooling season - - - - -	135
5-9	Characteristic of events - - - - -	143

ACKNOWLEDGEMENTS

The author wishes to express his thanks to Dr. Russell Elsberry for his time, patience, and guidance throughout this research, and to Drs. Dale Leipper, Robert Haney, and Roland Garwood for many helpful discussions.

The author also offers his gratitude to the personnel of the W. R. Church Computer Center, especially Sharon Raney, consultant, who kept track of all the numbers and wrote the plotting package.

Last, but certainly not least, the author expresses his gratitude to his family (Judith, Bradley, Megan, Charlie, and Happy) for their understanding and patience while this work was being done.

1. INTRODUCTION

A. PURPOSE OF THE STUDY

The fundamental objective of this study was to investigate the role of strong atmospheric forcing events in the modification of the upper ocean thermal structure during the fall and early winter cooling seasons. Simpson (1969) has demonstrated that the significant air-sea exchanges (heat, moisture, and momentum) in mid-latitudes are concentrated almost entirely into synoptic-scale forcing events. For example, during a three-month period of strong winter storms at ocean weather station CHARLIE (52.8N, 35.5W) in the Atlantic, 84% of the evaporation took place in only 30% of the time intervals. The mechanical energy and sensible heat exchange were similarly concentrated. Additionally, these large forcing events were identified with the travelling extratropical cyclone families that dominate the mid-latitude weather maps over ocean regions.

Simpson's analysis was directed, however, toward understanding the role of the large heat fluxes in modifying the cyclones themselves. The response of the upper ocean to these large heat and energy fluxes was not considered. In fact information, found in the literature, regarding the formation and destruction of transient thermoclines by these large atmospheric forcing events is rather qualitative in nature. A detailed investigation to determine the significance of these large storms to the total evolution of the upper ocean thermal structure is therefore needed. It was the purpose of this study to partially fulfill this need.

B. FUNDAMENTAL HYPOTHESIS

Denman and Miyake (1973) investigated the response of the upper ocean during a 12-day period (13-24 June 1970) at ocean weather station PAPA (50N, 145W) characterized by the passage of several summer storms. They demonstrated that the mixed layer response correlated with these storms was significantly larger than the changes in the thermal structure observed before and after the storms. The success with which Denman's (1973) numerical version of the Kraus and Turner (1967) mixed-layer model predicted the upper ocean response during this period demonstrated that the response was largely one-dimensional. That is, the heat budget of the mixed layer was closely determined by the vertical heat fluxes only.

The heat and mechanical energy fluxes reported by Simpson (1969) were significantly larger than the fluxes observed by Denman and Miyake (1973). Therefore, the fundamental hypothesis underlying this research is that significant upper ocean thermal structure modifications take place during strong atmospheric forcing events in the fall and early winter. Furthermore, these responses are largely one-dimensional and are principally the result of mechanical mixing and convective adjustment of the upper layers. We may therefore apply one-dimensional modeling techniques to examine the relative importance of the vertical mixing and convective processes during these strong fall and early winter events.

C. SPECIFIC OBJECTIVES OF THE STUDY

The specific objectives of this study were to examine the response of the upper ocean during a large number of strong atmospheric forcing events during the fall and early winter cooling season and attempt to:

- (1) determine the nature of the structural modifications that occur during these strong forcing events;
- (2) determine the extent that a modified version of the Kraus and Turner (1967) one-dimensional mixed-layer model is capable of simulating upper ocean response during these events;
- (3) establish the principal physical mechanisms that cause these modifications, and quantify the relative importance of mechanical mixing and convection;
- (4) establish the significant characteristics of the atmospheric forcing during these events;
- (5) determine what percentage of the total seasonal mixed layer response may be explained during these strong events.

These objectives represent a substantial departure from previous research designed to understand the modifications that take place in the upper ocean thermal structure. It is the first study designed to demonstrate that strong atmospheric forcing events dominate the fall and early winter erosion of the thermocline. Additionally, it is the first research that attempts to simulate the response of the upper ocean during these strong fall and winter events.

The formulation of a new one-dimensional mixed layer model is not an objective of this thesis. To a large extent the modern one-dimensional theories, developed during the past decade, have had only a few isolated tests with real data. This research will therefore be directed toward validating a number of modern mixed layer models with a large number of data sets gathered at the three North Pacific ocean weather stations. It will be demonstrated that the Kraus-Turner (1967) one-dimensional theory may be modified to adequately simulate these strong fall and winter forcing events. Additionally, the modified Kraus-Turner model will be used to isolate and examine the relative importance of mechanical mixing and convection at the three ocean weather stations.

D. OVERVIEW OF THE THESIS

In the next chapter the fundamental principles governing the evolution of the upper ocean will be reviewed and the important assumptions used in this thesis examined in detail. This chapter will further serve as a review of recent mixed-layer modeling theories. The ocean areas studied in this research included the regions occupied by ocean weather ships PAPA (50N, 145W), NOVEMBER (30N, 140W), and VICTOR (34N, 164E) in the North Pacific Ocean. In Chapter III the general characteristics of the atmospheric forcing and upper ocean thermal structure found at these three locations will be described. The analysis techniques, employed in this thesis, will be examined in Chapters IV and V. In Chapter IV several mixed-layer models will be employed to examine a large number of data sets in an attempt to accomplish the first three objectives. In Chapter V information relating to the final two objectives will be extracted from the historical surface and near-surface marine observations at the three ocean weather stations using a new analysis technique. Finally, in Chapter VI, the significant findings of this research will be presented and discussed relative to their importance in understanding and predicting upper ocean thermal structure modifications.

II. REVIEW OF MIXED-LAYER MODELING THEORIES

A. GOVERNING EQUATIONS

The changes that occur in the upper ocean are governed by the conservation laws of mass and momentum, by the equation of state for sea water, and the laws of thermodynamics. In this section the equations representing these physical laws will be examined, simplified, and transformed into parameterized expressions from which numerical solution may be obtained. Since many of the important objectives are based on the results of mixed layer models, a careful review of the mixed layer theories will be presented.

The conservation of momentum and mass are represented by the Navier-Stokes equation of motion, invoking the Boussinesq approximation, and the condition of incompressibility.

$$\frac{\partial u_i}{\partial t} + u_j \frac{\partial u_i}{\partial x_j} + \epsilon_{ijk} \Omega_j u_k = \frac{1}{\rho_0} \frac{\partial p}{\partial x_j} \delta_{ij} + \nu \frac{\partial^2 u_i}{\partial x_j^2} - \frac{\rho}{\rho_0} g \delta_{i3} \quad (2-1)$$

$$\frac{\partial u_i}{\partial x_i} = 0 \quad (2-2)$$

where $i, j = 1, 2, 3$

and $u_i = (u_1, u_2, u_3) = (u, v, w)$

$x_j = (x_1, x_2, x_3) = (x, y, z)$

Since the Boussinesq approximation assumes hydrostatic equilibrium for the reference state of the ocean, the pressure (p), and the density (ρ) represent departures from this state. The reference density is approximated, with sufficient accuracy, by a specified constant value ρ_0 .

(1.026 gm/cm³). Additionally, ϵ_{ijk} is the permutation tensor, Ω_j is the earth's rotation vector, δ_{ij} is the Kronecker delta, ν is the kinematic viscosity, and g is local gravity. Cartesian coordinates will be used throughout the development and the z -axis will be taken as positive up from the sea surface.

In the upper ocean the density is primarily a function of temperature (T), and salinity (s), such that a simplified equation of state may be assumed:

$$\rho(x_i, t) = \rho_0 \{1 - \alpha [T(x_i, t) - T_0] + \beta [s(x_i, t) - s_0]\} \quad (2-3)$$

where

$$\alpha = -\frac{1}{\rho} \frac{\partial \rho}{\partial T}, \quad \text{and} \quad \beta = \frac{1}{\rho} \frac{\partial \rho}{\partial s}.$$

The coefficients, α and β , are taken as constants throughout this thesis as $\alpha = 2.5 \times 10^{-4} (\text{°C})^{-1}$, and $\beta = 7.5 \times 10^{-4} (\text{°/oo})^{-1}$.

It will be assumed that the frictional generation of heat and molecular heat transfer processes are negligible compared with typical values of radiant solar energy and the turbulent heat fluxes exchanged between the ocean and atmosphere. Therefore a simplified form of the first law of thermodynamics may be expressed as:

$$\frac{\partial T}{\partial t} + u_j \frac{\partial T}{\partial x_j} = \frac{1}{\rho_0 C_p} \frac{\partial R(z)}{\partial z} \quad (2-4)$$

According to Jerlov (1968), the total downward irradiance in the spectral range of 300-2500 nm decreases to 50% of its surface value in the first meter of the ocean, virtually irrespective of the water type considered.

Therefore, in this study, the absorption of short wave radiation below the initial meter will be approximated by:

$$R(z) = R_0 e^{\gamma z} \quad (2-5)$$

where γ represents a total extinction coefficient (taken as 0.3 m^{-1}). R_0 represents the surface absorption, $R_0 = .5 Q_s$, where Q_s is the total solar flux at the surface.

The final expression necessary to complete the system is the equation for conservation of salt. Once again neglecting molecular diffusion, it may be simply represented as:

$$\frac{\partial s}{\partial t} + u_j \frac{\partial s}{\partial x_j} = 0 \quad (2-6)$$

B. THE ONE-DIMENSIONAL HYPOTHESIS

The basic assumption of the one-dimensional hypothesis is that the ocean is horizontally homogeneous in all its properties (u_j , s , T). This assumption restricts the domain of applicability to time and space scales over which the vertical fluxes of mass and momentum dominate the horizontal fluxes. Because of the sparsity of open ocean measurements this assumption is difficult to verify a priori. However, the one-dimensional hypothesis is desirable at this point because three-dimensional models are not only far more complicated and expensive, but the frequency of observations (especially oceanic) prohibits proper initialization, calibration, and validation.

C. TURBULENT FORM OF THE BASIC EQUATIONS

The turbulent components are introduced into the basic equations through the Reynolds decomposition technique, whereby the variables are expressed as a time averaged mean and a fluctuation about the mean (i.e. $T = \bar{T} + T'$). The prime denotes the fluctuation and the overbar represents the mean;

$$\bar{T} = \frac{1}{\Delta t} \int_{-\frac{\Delta t}{2}}^{\frac{\Delta t}{2}} T \, dt, \quad (2-7)$$

for example. The integral time scale, Δt , should be short compared with the time in which the mean field properties are changing, but long relative to the time scale of the fluctuations.

Applying this technique to the basic set of equations (neglecting the mean vertical motion \bar{w}) results in the following:

$$\frac{\partial \bar{c}}{\partial t} + i f \bar{c} = - \frac{\partial \overline{w'c'}}{\partial z} \quad (2-8)$$

$$\frac{\partial \bar{T}}{\partial t} = \frac{1}{\rho_o C_p} \frac{\partial}{\partial z} (R(z) - \rho_o C_p \overline{w'T'}) \quad (2-9)$$

$$\frac{\partial \bar{s}}{\partial t} = - \frac{\partial \overline{w's'}}{\partial z} \quad (2-10)$$

Equation (2-8) is the equation of mean motion expressed in complex notation ($c = u + iv$) with the geostrophic component removed. Equations (2-9) and (2-10) are the conservation relations for mean temperature (\bar{T}) and salinity (\bar{s}), while expressions $\overline{w'c'}$, $\overline{w'T'}$, and $\overline{w's'}$ represent the turbulent fluxes of momentum, temperature, and salt respectively. The parameterization of these fluxes will be accomplished,

in part, by examining the turbulent kinetic energy budget for the upper ocean, which is derived from the Navier-Stokes equation.

If (2-1) is multiplied by u_i and subjected to Reynolds decomposition, the resulting expression will represent the conservation of total kinetic energy. The conservation of mean kinetic energy is formulated by the decomposition of (2-1) multiplied by the time averaged mean velocity \bar{U}_i . The turbulent kinetic energy equation is obtained by subtracting the mean from the total equation and the resulting expression is:

$$\frac{\partial}{\partial t} \left(\frac{\overline{q^2}}{2} \right) + \frac{\partial}{\partial z} \left[\overline{w' \left(\frac{p'}{\rho_0} + \frac{q^2}{2} \right)} \right] = - \overline{u'_\alpha w'} \frac{\partial \bar{U}_\alpha}{\partial z} - g \frac{\overline{w' \rho'}}{\rho_0} - \epsilon \quad (2-11)$$

where

$$q^2 = u_i' u_i',$$

$$u_\alpha = (u, v),$$

and

$$\epsilon = \nu \left(\frac{\partial u_i'}{\partial x_j} \right)^2$$

The first term on the left is the local time rate of change of turbulent kinetic energy while the second, the divergence term, specifies the vertical redistribution of the turbulent kinetic energy $\overline{w'(p'/\rho_0 + q^2/2)}$ by the turbulence. This energy is generated primarily by breaking waves at the surface and by the Reynolds stresses acting on the mean flow. The right hand terms represent the three ways in which turbulent kinetic energy is either gained or lost. The first of these, which is usually positive, is the rate at which mean kinetic energy is converted to turbulent kinetic energy by the working of the Reynolds stresses $-\rho_0 \overline{u'_\alpha w'}$ against the mean velocity gradient $\frac{\partial \bar{U}_\alpha}{\partial z}$. The second, the covariance

between the fluctuations in density and the vertical velocity, may be positive or negative. If the basic density distribution is statically unstable, then fluid elements moving upwards tend to be less dense than those descending, and a release of potential energy takes place by free convection ($-g \overline{w'\rho'}/\rho_0 > 0$). If, on the other hand, the density distribution is stable, the reverse is true and $-g \overline{w'\rho'}/\rho_0 < 0$. This covariance then represents the rate at which turbulent kinetic energy is expended by mixing the less dense fluid downward, thus increasing the potential energy. The last term (ϵ) is the rate at which turbulent kinetic energy is dissipated by viscosity and always represents a loss. To solve the system (2-8) - (2-11) requires specification of the vertical structure of the properties and the boundary conditions imposed on the domain. Moreover, this involves parameterization of turbulent processes and additional simplifications will be necessary to make the problem tractable.

D. THE BULK MODEL HYPOTHESIS

In this thesis the one-dimensional dynamic processes that affect the evolution of the upper ocean will be studied in terms of the energetics associated with the turbulent kinetic budget. The parameterization of these energetics is accomplished by idealizing the upper ocean structure with the assumptions of the bulk model hypothesis (depicted in Fig. 2-1). The quantities C_s , T_s , S_s represent the vertically averaged values of velocity, temperature, and salinity, defined for example as

$$C_s = \frac{1}{h + \delta} \int_{-h-\delta}^0 c \, dz \quad (2-12)$$

With this concept, the density structure (T_s , S_s) directly below the wind blown ocean surface is assumed vertically homogeneous to a depth of

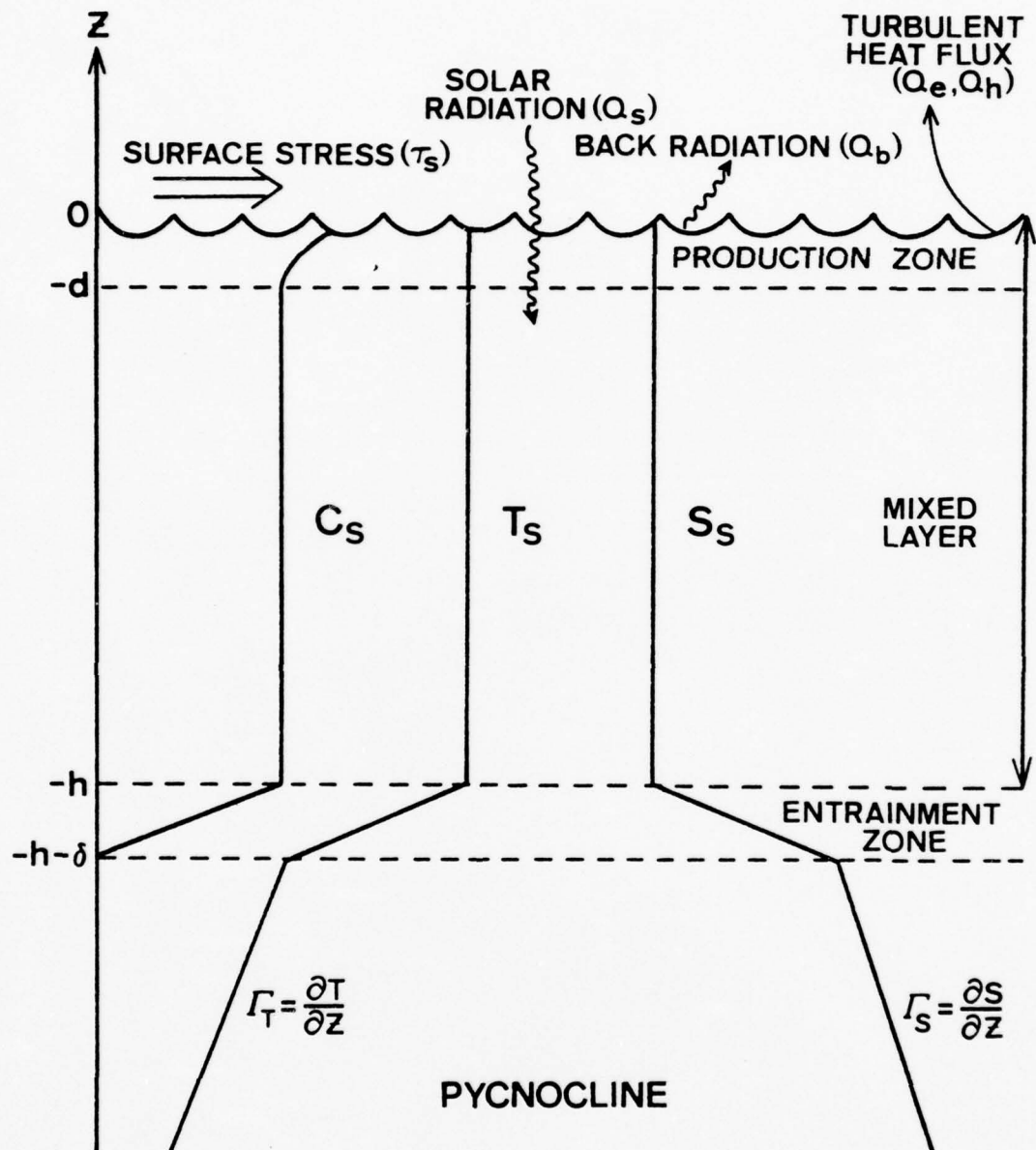


Figure 2-1. Schematic of the oceanic mixed layer.

$z = -h$. Below this level there is a discontinuity in the density followed by a stable density profile. The mean velocity structure is modeled as being vertically uniform and fully turbulent in the mixed layer and negligibly small and nonturbulent below. Deviations from this vertical structure occur at the top and bottom of the layer where shear zones are formed. These shear zones are formed at the top due to the action of the wind on the water, and at the bottom due to the slab-like motion of the mixed layer over the quiescent water in the pycnocline. The surface shear zone is known as the production zone, where turbulent kinetic energy is generated by the working of the Reynolds stresses against the mean velocity gradient. The bottom shear zone is an entrainment zone of thickness δ . There is a vertical flux of mass and momentum at the top ($z = -h$) while none leaks out the bottom ($z = -h-\delta$). It is further assumed that the Reynolds stresses are also capable of generating turbulence in this zone. Thus the bulk model concept assumes that variations from the structure of the upper ocean depicted in Fig. 2-1 may be neglected and the vertical mean quantities may be predicted, with sufficient accuracy, by specification of the turbulent transfer processes at the boundaries.

To maintain these homogeneous profiles throughout the mixed layer a continual vertical flux of turbulent energy is necessary throughout the layer. When there is a convergence of turbulent energy at $z = -h$, the entrainment zone is destabilized and the excess turbulent kinetic energy is expended by entraining fluid from below as the layer deepens. With a downward buoyancy flux at the surface (excess heating or precipitation), it is possible that an insufficient flux of turbulent kinetic energy may be available to mix the fluid homogeneously to the existing mixed layer depth. In this case a new mixed layer depth is established at the level

where the downward vertical turbulent flux vanishes. Since this level is higher than the previous layer depth, this formation is called layer retreat. The turbulent motions below this level are assumed to be shut off from the energy source, and become nonturbulent by viscous forces on a dissipation time scale. It is therefore envisioned that the mixed layer is being constantly re-established from the surface, and that shallowing mixed layers are not the result of the interface moving upward, but are the consequence of net surface heating and an insufficient downward flux of turbulent kinetic energy.

E. BOUNDARY CONDITIONS

The boundary conditions will be specified as a function of time and the overbar on the mean quantities will be dropped. The surface stress is denoted as τ_s and

$$-\overline{w'T}(0) = \frac{\tau_s + i0}{\rho_0} \quad (2-13)$$

$$\text{while} \quad \left(\frac{R(z)}{\rho_0 C_p} - \overline{w'T} \right) (0) = \frac{Q_s - Q_a}{\rho_0 C_p} \quad (2-14)$$

The term Q_a is the sum of the turbulent fluxes of latent (Q_e) and sensible (Q_h) heat and the effective long wave back radiation (Q_b). The short wave solar energy (Q_s) is always taken as a positive value.

The surface flux of salt is

$$-\overline{w's}(0) = s(E-P) \quad (2-15)$$

where P is the rate of precipitation, and E is the evaporation rate.

The boundary conditions at the bottom of the mixed layer are derived by integrating (2-8) - (2-10) over the entrainment zone ($-h-\delta \leq z \leq -h$). Thus

$$\overline{w'c'}(-h) = - \frac{\partial h}{\partial t} \Delta c$$

where $\Delta c = c(-h) - c(-h-\delta)$

Since only one-dimensional effects are considered in this model, $\frac{\partial h}{\partial t}$ is the time rate of change of the mixed layer depth (h) due to turbulent processes. As this expression implies an upward momentum flux for $\frac{\partial h}{\partial t} < 0$ (an impossibility in this system), it is rewritten as

$$\overline{w'c'}(-h) = - \Lambda \frac{\partial h}{\partial t} \Delta c \quad (2-16)$$

where Λ is the Heaviside unit step function defined as

$$\Lambda = \begin{cases} 0, & \text{if } \frac{\partial h}{\partial t} \leq 0 \\ 1, & \text{if } \frac{\partial h}{\partial t} > 0 \end{cases} \quad (2-17)$$

The fluxes of heat and salt at the base of the mixed layer are similarly derived and are

$$\left(\frac{R(z)}{\rho_o C_p} - \overline{w'T'} \right) (-h) = \frac{R_o e^{-\gamma h}}{\rho_o C_p} + \Lambda \frac{\partial h}{\partial t} \Delta T \quad (2-18)$$

$$\overline{w's'}(-h) = -\Lambda \frac{\partial h}{\partial t} \Delta s \quad (2-19)$$

F. THE INTEGRATED MASS, MOMENTUM, AND ENERGY BUDGETS

Equations (2-8) - (2-10) may now be integrated over the mixed layer to form the mass and momentum budgets of the region. The results are:

$$\frac{\partial C_s}{\partial t} + f C_s = \frac{1}{h} \left[\frac{\tau_s + i o}{\rho_o} - \Lambda \frac{\partial h}{\partial t} C_s \right] \quad (2-20)$$

$$\frac{\partial T_s}{\partial t} = \frac{1}{h} \left[\frac{Q_s - Q_a - R_o e^{-\gamma h}}{\rho_o C_p} - \Lambda \frac{\partial h}{\partial t} \Delta T \right] \quad (2-21)$$

$$\frac{\partial S_s}{\partial t} = \frac{1}{h} \left[s(E-P) - \Lambda \frac{\partial h}{\partial t} \Delta s \right] \quad (2-22)$$

These equations are subject to simple interpretation. Equation (2-20) shows that the mean motion of the mixed layer is modified in time by rotation and the vertical fluxes of momentum at the surface and base of the slab. The surface flux may add or subtract momentum depending on the relative directions of τ_s and C_s . During the period when the mixed layer is deepening the flux of momentum at the base is always a sink for energy ($\Delta c \equiv C_s \geq 0$) and represents the energy necessary to impulsively accelerate the entrained fluid to the velocity of the mixed layer. For deepening mixed layers the density, specified by (2-21) and (2-22), will normally increase due to the turbulent flux of density at the surface and base of the mixed layer, while it normally decreases for shallowing layers. For stable temperature and salinity structures, deepening layers normally become cooler and more saline while the reverse is true for the retreating case.

To close this system the time rate of change of the mixed layer depth ($\partial h / \partial t$) must be specified. This may be accomplished through the

integration of the turbulent kinetic energy equation over the mixed layer. It is at this point where most modern one-dimensional bulk models differ and the procedure will be given careful consideration.

One may start by defining the terms of (2-11) as follows:

$$G_* = -\rho_o \int_{-h-\delta}^0 \left\{ \frac{\partial}{\partial z} \left[\overline{w' \left(\frac{p'}{\rho_o} + \frac{q^2}{2} \right)} \right] + \overline{u'_\alpha w'} \frac{\partial \overline{U}_\alpha}{\partial z} \right\} dz \quad (2-23)$$

$$D_* = \rho_o \int_{-h-\delta}^0 \epsilon dz \quad (2-24)$$

$$P_* = \rho_o \int_{-h-\delta}^0 \overline{w' b'} dz \quad (2-25)$$

$$S_* = \rho_o \int_{-h-\delta}^0 \frac{\partial}{\partial t} \left(\frac{\overline{q^2}}{2} \right) dz \quad (2-26)$$

The first term (G_*) represents the total contribution to the turbulent kinetic energy budget by mechanical production processes. The second expression (D_*) is the total dissipation in the layer by viscous forces. The rate at which potential and turbulent kinetic energy are being exchanged is represented by P_* , where $\overline{w' b'}$ is the turbulent flux of buoyancy.

$$\overline{w' b'} = -g \frac{\overline{w' \rho'}}{\rho_o} = g(\alpha \overline{w' T'} - \beta \overline{w' s'}) \quad (2-27)$$

Finally, S_* is the rate at which the turbulent kinetic energy budget for the layer is changing, and is commonly known as the storage term. The integrated form of (2-11) may be simply expressed as

$$P_* + G_* - D_* - S_* = 0 \quad (2-28)$$

Kraus and Turner (1967) were the first to formulate a mixed-layer model based upon (2-28), except they neglected the storage term and assumed the density a function of temperature only. In deriving an expression for P_* , the assumption that temperature and salinity remain vertically homogeneous throughout the mixed layer, and the relationships represented by (2-9) and (2-10), require that the vertical fluxes of heat and salt be a linear function of depth. With this restriction the trapezoidal rule may be applied to these fluxes and an expression for P_* derived as

$$\begin{aligned}
 P_* &= \rho_o g \alpha \int_{-h}^0 \overline{w'T'} dz - \rho_o g \beta \int_{-h}^0 \overline{w's'} dz = \\
 &- \frac{\rho_o g h}{2} \left\{ \left[\frac{Q_s - Q_a - R_o F(\gamma h)}{\rho_o C_p} + \Lambda \frac{\partial h}{\partial t} \Delta T \right] \right. \\
 &\left. + \frac{\beta}{\alpha} [s(E-P) + \Lambda \frac{\partial h}{\partial t} \Delta s] \right\} = \frac{B_o h}{2} + \frac{h \Delta b}{2} \Lambda \frac{\partial h}{\partial t}, \quad (2-29)
 \end{aligned}$$

where

$$B_o = \rho_o g \alpha \left[\frac{Q_s - Q_a - R_o F(\gamma h)}{\rho_o C_p} - \frac{\beta}{\alpha} s(E-P) \right], \quad (2-30)$$

$$\Delta b = \rho_o g \alpha \Delta T - \rho_o g \beta \Delta s, \quad (2-31)$$

and

$$F(\gamma h) = \frac{2}{\gamma h} [1 - e^{-\gamma h}] - e^{-\gamma h} \quad (2-32)$$

The process modeled by $\frac{h\Delta b}{2} \Lambda \frac{\partial h}{\partial t}$ represents the amount of turbulent kinetic energy expended to deepen the mixed layer and increase the potential energy of the column of water (raise the center of gravity) by entraining denser fluid from below. $\frac{B_o h}{2}$ is the turbulent kinetic energy (released potential energy) generated when $B_o < 0$ and free convection occurs. When $B_o > 0$, it represents the energy expended during forced convection to mix the buoyant surface water downward and increase the potential energy.

The function $F(\gamma h)$ reflects the penetration of solar energy to some depth with the property that $F(\gamma h) \rightarrow 0$ as $\gamma h \rightarrow \infty$ (complete absorption in the layer), and $F(\gamma h) \rightarrow 1$ as $\gamma h \rightarrow 0$ (complete penetration through the layer). Substituting (2-29) into (2-28) results in an expression for the time rate of change of the mixed-layer depth in terms of G_* , D_* , S_* and the surface fluxes of heat and salt;

$$\Lambda \frac{\partial h}{\partial t} = \frac{1}{(\Delta T - \frac{\beta}{\alpha} \Delta s)} \left[\frac{Q_a - Q_s + R_o F(\gamma h)}{\rho_o C_p} + \frac{\beta}{\alpha} (E - P) + \frac{2(G_* - D_* - S_*)}{\rho_o g \alpha h} \right] \quad (2-33)$$

When the right hand side is positive a deepening mixed layer is predicted. When the terms are negative the Heaviside function is equal to zero and a diagnostic equation is formed to obtain the depth to which the layer retreats. The methods by which S_* , G_* , and D_* are parameterized will now be described.

The storage term is parameterized in a manner described by Kim (1976). The vertical mean turbulent kinetic energy of the layer, postulated as being quasi-invariant in time, is defined as

$$C_m^2 = \frac{1}{h} \int_{-h}^0 \overline{q^2} dz \quad (2-34)$$

and the storage term parameterized as

$$S_* = \frac{1}{2} \rho_o C_m^2 \frac{\partial h}{\partial t} \quad (2-35)$$

Kim further assumes that

$$C_m^2 = m_1 w_*^2 \quad (2-36)$$

where m_1 is a nondimensional constant, and

$$w_* = \left(\frac{\tau_s}{\rho_o} \right)^{1/2} \quad (2-37)$$

is the friction velocity of the water.

The parameterization of the total mechanical production of turbulent kinetic energy may be accomplished by integration of (2-23) over the mixed layer, with the integration intervals depicted in fig. 2-1.

$$G_* = -\rho_o \left\{ \left[w' \left(\frac{p'}{\rho_o} + \frac{q^2}{2} \right) \right]_0^{\infty} + \int_0^{\infty} \overline{u'_\alpha w'} \frac{\partial \overline{U}_\alpha}{\partial z} dz + \int_{-h-\delta}^{-h} \overline{u'_\alpha w'} \frac{\partial \overline{U}_\alpha}{\partial z} dz \right\} \quad (2-38)$$

The first two terms represent the mechanical production at the surface due to atmospheric perturbations and breaking waves (term 1), and the work performed against the mean velocity gradient by the Reynolds stresses (term 2). The third term is the shear production in the entrainment zone as the layer deepens. Niiler (1975) carefully performed these integrations to show that the contribution of the first two terms is

proportional to the cube of the friction velocity (w_*), while the third is approximately $\Lambda \frac{\partial h}{\partial t} \frac{|C_s|^2}{2}$. Therefore

$$G_* = m_2 \rho_o w_*^3 + m_3 \rho_o \Lambda \frac{\partial h}{\partial t} \frac{|C_s|^2}{2} \quad (2-39)$$

and the nondimensional constants m_2 and m_3 are both of order unity.

The total integrated turbulent kinetic budget is obtained by substituting (2-29), (2-35), and (2-39) into (2-28).

$$\begin{aligned} & \underbrace{\frac{\rho_o m_1 w_*^2}{2} \frac{\partial h}{\partial t}}_I + \underbrace{\frac{h \Delta b}{2} \Lambda \frac{\partial h}{\partial t}}_{II} \\ & = \underbrace{m_2 \rho_o w_*^3}_{III} + \underbrace{\frac{m_3 \rho_o |C_s|^2}{2} \Lambda \frac{\partial h}{\partial t}}_{IV} - \underbrace{\frac{B_o h}{2}}_V - \underbrace{D_*}_{VI} \end{aligned} \quad (2-40)$$

G. CLASSES OF MIXED LAYER MODELS

1. The Prototype Turbulent Bulk Model

Most modern mixed layer models can be classified as to which terms of (2-40) are used to predict changes in the mixed layer properties. Kraus and Turner (1967), hereafter KT, formulated the prototype turbulent bulk model, assuming a balance between terms II, III, and V in (2-40) and neglecting the rest as follows:

$$\frac{h \Delta b}{2} \Lambda \frac{\partial h}{\partial t} = \rho_o w_*^3 - \frac{B_o h}{2} \quad (2-41)$$

When the sum of the terms on the right are positive, the layer deepens according to

$$\frac{\partial h}{\partial t} = \frac{2\rho_o w_*^3 - B_o h}{h\Delta b} \quad (2-42)$$

However, during periods of weak winds and surface heating, the right hand side becomes negative and

$$h_r = \frac{2\rho_o w_*^3}{B_o} \quad (2-43)$$

is a prognostic equation which calculates the retreating mixed layer depth proportional to the Monin-Obukhov length scale (L). Incidentally, Kitaigorodski (1960), using a steady state model and dimensional analysis, reasoned that this should be the proper length scale.

Kraus and Turner demonstrated that this model was capable of simulating the annual evolution of the mixed layer with a saw tooth heating function and constant wind stress. Denman and Miyake (1973) applied a numerical version of KT to a 12-day period at ocean station PAPA with favorable results. Using observed forcing they were able to simulate both the daily and weekly changes in mixed layer temperature and depth during a period of moderate synoptic scale winds, apparently without any significant effects from vertical or horizontal advection. On the other hand, Dorman (1974) applied the same model to cases of spring heating and fall cooling at ocean station NOVEMBER with limited success, and attributed the model's poor performance to horizontal advection.

However, these few simulations are not conclusive evidence for the validity of the one-dimensional bulk model (in particular KT) and

a primary objective of this work will be to attempt a large number of experiments to gather such evidence. In addition to KT, the model of Kim (1976) and the model of Elsberry, Fraim, and Trapnell (1976), hereafter KIM and EFT, will be evaluated. Both of these models assume the dominance of surface production and are therefore of the KT type.

Kraus and Turner originally determined that KT predicted excessive mixed layer depths when mechanical production and free convection were considered together. They concluded that either their parameterization of mechanical production was in error or the effects of dissipation could not be neglected, or both. Turner (1969) found that the fraction of the total energy, imparted during an impulsive wind event, that is used to increase the potential energy by entrainment was larger than $\rho_o w_*^3$, as originally reasoned by Kraus and Turner from dimensional analysis. He suggested that much of the kinetic energy goes into drift currents and is eventually used to deepen the layer; however he did not specify the mechanism for this deepening.

2. The Prototype Inertial Bulk Model

In an attempt to explain the rapid deepening of the mixed layer in response to strong impulsive forcing, as reported by Turner (1969), Pollard, Rhines, and Thompson (1973), hereafter PRT, formulated a model quite different from KT. Assuming the density was a function of temperature only, they neglected the turbulent kinetic energy budget and considered only the time rate of change of total kinetic (\overline{KE}) and potential (\overline{PE}) energy as follows:

$$\frac{\partial \overline{PE}}{\partial t} + \frac{\partial \overline{KE}}{\partial t} = \tau_s u(o) \quad (2-44)$$

Further, they implied that at the onset of heavy winds the mixed layer would respond and move as a slab, and through the mechanism of mean flow instability the mixed layer would deepen. They postulated that the mean flow would remain unstable as long as the bulk Richardson number (R_i^*) was less than or equal to unity.

$$R_i^* = \frac{g\alpha h \Delta T}{|C_s|^2} \leq 1 \quad (2-45)$$

The PRT model predicts continual deepening as long as $\tau_s u(o)$ is positive and $R_i^* \leq 1$. If $\overline{w'c'}(o) = -w_*^2 + io$, a particular solution for (2-19) is

$$C_s = \frac{w_*^2}{fh} [\sin ft - i(1 - \cos ft)] \quad (2-46)$$

At time $t = \pi/f$ (half the inertial period), $\tau_s u(o)$ becomes negative, the energy flow to increase h ceases, and since the water cannot unmix, h must remain constant and $R_i^* > 1$. The PRT model predicts a maximum mixed layer depth for a constant w_* as

$$h_{\max} = \frac{1.7 w_*}{\sqrt{fN}} \quad (2-47)$$

where $N^2 = g\alpha\Gamma_T$ and N is the Brunt-Väisälä frequency.

Nilner (1975) concluded that the PRT model, in reality, assumes a balance between terms II and IV in (2-40). If $m_3 = 1$, then this balance simply reduces to (2-45). The model is most effective in causing mixed-layer depth changes during periods of relatively shallow mixed layers and strong impulsive winds. However, a major difficulty with this

model is that it fails to account for the gradual deepening that takes place during periods of weak forcing or when the initial layer depth is greater than h_{\max} . It is entirely possible that the deepening of the mixed layer may occur as a combination of KT and PRT and that the geophysical situation (magnitude of the wind, layer depth, and ocean stability) will dictate which process will dominate.

In section IV the one-dimensional bulk models of KT, EFT, and KIM will be applied to data sets obtained during the autumn and winter season in the North Pacific. The PRT model was not included in this study because the calculations shown in Table 2-1 indicate that the bulk Richardson number remains greater than unity during all but a small number of observations during these periods ($h_0 > 30$ m). In performing these calculations it was assumed that at time $t = 0$, $h = h_0$, and both PRT and KT type deepening occur simultaneously. Additionally surface heat fluxes were neglected, a constant temperature gradient was assumed, and ΔT was approximated by $\frac{h\Gamma_T}{2}$. The values of R_i^* (as a function of wind speed) are calculated at $t = \pi/f$. Therefore values of $R_i^* < 1$ indicate situations when the PRT model would have deepened a greater amount than the KT model. Also, it has not been clearly established that the mean flow positively becomes unstable at $R_i^* = 1$ and, in fact, the instability may be initiated at much lower values (see Turner, 1973, pp. 97-102).

H. NON-PENETRATIVE FREE CONVECTION

Returning to the KT model two difficulties are yet to be resolved. The first of these involves the percentage of turbulent kinetic energy generated during free convection that is actually utilized for entrainment. Kraus and Turner followed Ball (1960) and assumed that 100 percent

TABLE 2-1. R_i^* as a function of wind speed (U_{10}) and initial layer depth (h_o).

U_{10} (m/sec)	$h_o = 30$ m	$h_o = 40$ m	$h_o = 50$ m	$h_o = 60$ m
1	4.2×10^4	1.3×10^5	3.2×10^5	6.7×10^5
5	70.0	2.2×10^2	5.2×10^2	1.0×10^3
10	5.6	15.1	35.0	70.0
15	1.9	3.9	8.0	15.0
20	1.1	1.9	3.2	5.6
25	1.0	1.2	1.8	2.9
30	.8	1.0	1.3	1.8
35	.7	.8	1.1	1.4
40	.7	.8	.9	1.1
45	.7	.7	.8	1.0
50	.7	.7	.8	.9

is used. However, laboratory work by Deardorff, Willis, and Lilly (1969), and a more recent field experiment by Farmer (1975) indicate that only a small fraction of this energy (1-3%) is actually converted to potential energy through entrainment. Furthermore, Gill and Turner (1975) demonstrated that a fraction equal to 0.15 was adequate to achieve annual cyclic steady state in the potential energy balance. The reason becomes evident by considering a simple case where solar radiation is neglected and density is a function of temperature only. Then,

$$\frac{\partial PE}{\partial t} = -\rho_o g \alpha \int_{-h}^0 \overline{wT} dz \quad (2-48)$$

or

$$\frac{\partial PE}{\partial t} = -\frac{\rho_o g \alpha h}{2} \left[\frac{Q_a}{\rho_o C_p} - \Lambda \frac{\partial h}{\partial t} \Delta T \right] \quad (2-49)$$

Writing (2-33) as

$$\Lambda \frac{\partial h}{\partial t} \Delta T = r \frac{Q_a}{\rho_o C_p} + \frac{2(G_* - D_* - S_*)}{\rho_o g \alpha h} \quad (2-50)$$

where r is the fraction of convectively-generated turbulent kinetic energy utilized for entrainment, (2-49) becomes

$$\frac{\partial PE}{\partial t} = -\frac{\rho_o g \alpha h}{2} (1-r) \frac{Q_a}{\rho_o C_p} + G_* - D_* - S_* \quad (2-51)$$

The KT model assumes $r = 1$ and neglects D_* and S_* .

$$\frac{\partial PE}{\partial t} = G_* = \rho_o w_*^3 \quad (2-52)$$

Equation (2-52) demonstrates clearly that a cyclic steady state balance is impossible in the KT model and, except when the wind stops blowing, the potential energy increases continually. The consequences are excessive mixed layer depths and downward heat flux into the deep layers.

As the entrainment process takes place, a continual downward heat flux into the deeper layers occurs. Before the seasonal thermocline may be reestablished, during the spring and summer heating cycle, this heat must be removed by non-penetrative free convection (cooling without deepening). The KT model cannot accomplish this process and, when integrated over several annual cycles, will eventually erode away the thermocline. Therefore, the conclusion is drawn that non-penetrative free convection ($r < 1$) must be an integral part of any mixed layer model and, following Gill and Turner (1975), a value of $r = 0.15$ will be used in all the models evaluated in this thesis (including KT). The theory explaining how such a large percentage (85%) of the kinetic energy is lost is not complete. A certain amount is dissipated by viscosity, and atmospheric investigations such as Townsend (1968) and Stull (1975) indicate that internal waves generated by convection are capable of radiating energy away from the mixed layer interface into the gradient region.

1. DISSIPATION ENHANCEMENT

The second difficulty with KT is that excessive deepening is predicted, even when free convection is neglected. This is a consequence of not properly parameterizing dissipation. A tank experiment by Thompson and Turner (1975) demonstrated that the entrainment rate produced by a stirring grid is not directly related to the velocity of the stirrer, but to the turbulent velocity near the interface. They reasoned

that the turbulent kinetic energy density decays with depth and that less is available for mixing as the layer deepens and the entrainment zone gets further away from the surface production zone.

The first model to include this process was that of Elsberry, Fraim, and Trapnell (1976). Total dissipation was assumed to increase exponentially as a function of layer depth, h , and a scale depth, Z , and

$$G_* - D_* = \rho_o w_*^3 e^{-h/Z} \quad (2-53)$$

In this model $G_* - D_*$ is nearly equal to the downward energy flux from the atmosphere (according to KT) if the mixed layer is shallow ($h \ll Z$) while it tends towards zero for very deep layers.

A more recent model by Kim (1976) also uses a depth dependent dissipation parameterization and additionally includes the storage term.

$$G_* - D_* = 1.25 \rho_o w_*^3 - \rho_o D_b h \quad (2-53a)$$

where D_b is a constant background dissipation. The surface production term is parameterized according to Kato and Phillips (1969), and D_b calculated from the dissipation data of Grant, Moilliet, and Vogel (1968). Kim's model has the additional interesting property of being able to predict steady state in the potential energy balance for neutral conditions (no heating or cooling). For the KIM model (2-51) becomes

$$\frac{\partial PE}{\partial t} = -\frac{\rho_o g \alpha h}{2} (1-r) \frac{Q_a}{\rho_o C_p} + 1.25 \rho_o w_*^3 - \rho_o D_b h - \frac{1}{2} m_1 \rho_o w_*^2 \frac{\partial h}{\partial t} \quad (2-54)$$

and for $\frac{\partial PE}{\partial t} = 0$, and $Q_a = 0$

$$h = \frac{1.25 w_*^3 - \frac{1}{2} m_l w_*^2 \frac{\partial h}{\partial t}}{D_b}, \quad (2-55)$$

with solution

$$h = C e^{-\left(\frac{D_b t}{\frac{1}{2} m_l w_*^2}\right)} + \frac{1.25 w_*^3}{D_b} \quad (2-56)$$

and C is a constant determined by initial conditions.

Thus, neutral steady state is predicted for $t \gg \frac{m_l w_*^2}{2D_b}$; this means that a constant wind is only capable of deepening the layer to a depth described by (2-56).

J. VERTICAL DIFFUSION

The prototype turbulent bulk model has the undesirable tendency to predict abnormally large temperature gradients at the base of the mixed layer (see Denman and Miyake, 1973, Fig. 6). This is a consequence of the zero-flux condition imposed at the base of the entrainment zone. An attempt will be made in this research to overcome this difficulty by assuming that the thermocline is weakly diffusive. The temperature below the mixed layer will be specified by

$$\frac{\partial T}{\partial t} = A_v \frac{\partial^2 T}{\partial z^2} \quad (2-57)$$

where A_v is the vertical diffusion coefficient. The KT, KIM, and EFT will be evaluated with this diffusion tendency to determine its effectiveness.

K. SALINITY EFFECTS

An additional assumption, made throughout this thesis, is that the density structure is a function of temperature only and that buoyancy flux $(\overline{w'b'})$ is synonymous with heat flux $(\overline{w'T'})$. This assumption is necessary (but certainly not desirable) because the data used in this investigation included neither salinity structure information nor observed precipitation rates. The errors introduced into the system by this assumption are reflected by (2-33), and (2-40). These equations indicate that salinity changes may be an important consideration depending on the season, geographical location, and vertical depth scale over which the model is applied. An attempt will be made to determine to what extent this assumption affects model performance.

In summary, the fundamental principles governing the evolution of the mixed layer have been reviewed in some detail, and the assumptions of the one-dimensional bulk model specified. The expressions that will be used to examine the physical processes responsible for observed changes in the mixed layer are (2-21), (2-33), and (2-40).

III. CHARACTERISTICS OF THE ATMOSPHERIC FORCING AND OCEANIC STRUCTURE AT OCEAN WEATHER SHIPS (OWS) PAPA (P), NOVEMBER (N) AND VICTOR (V)

A. DATA SOURCES

One of the largest data sets for investigating the upper ocean thermal response to atmospheric forcing is the meteorological and oceanographic observations taken at ocean weather ships. To examine the physical mechanisms responsible for changing the thermal structure, it was decided to focus the analysis on the data gathered at Ocean Weather Ships PAPA (50N, 145W), NOVEMBER (30N, 140W), and VICTOR (34N, 164E) in the North Pacific. Furthermore, since the objective of this thesis is to examine these processes during the fall and early winter cooling season, only data collected during September through December will be considered.

The near-surface marine observations were provided by the National Weather Records Center and the three-hourly data included measurements of sea-surface temperature (T_w), air-temperature (T_a), dew point (T_d), wind speed (u_a), and visual estimates of total cloud cover (C). Table (3-1) lists the years when data were available and includes approximately 96% of the possible three-hourly records.

TABLE 3-1. Availability of data at the ocean weather stations.

Station	Atmospheric Observations	Mechanical BT's
P	1946, 1948-1970	1946, 1948-1970
N	1946-1951 1953-1954 1956-1970	1947-1950 1954-1970
V	1956-1970	1956-1970

Information regarding the evolution of the oceanic thermal structure was obtained through analysis of mechanical bathythermograph (MBT) records provided by the National Oceanographic Data Center. The years for which MBT data were available are also listed in Table (3-1); however, the frequency of these observations was highly variable, and usually numbered less than a few hundred per season.

B. FORMULAS FOR COMPUTING ATMOSPHERIC FORCING

Examination of (2-21), (2-31), and (2-38) indicates that the atmospheric forcing necessary for modeling the response of the upper ocean includes a measure of turbulent kinetic energy flux (w_*^3), the effective solar radiation (Q_s), the turbulent fluxes of sensible (Q_h) and latent heat (Q_e), and the net back radiation (Q_b). These variables may be estimated using the measured atmospheric parameters in the following bulk aerodynamic formulas:

$$u_* = \sqrt{C_D} (u_a \times 10^2) \text{ (cm/sec)} \quad (3-1)$$

$$Q_e = 3,767 C_D (0.98 E_w - E_a) u_a \text{ (ly/day)} \quad (3-2)$$

$$Q_h = 2,488 C_D (T_w - T_a) u_a \text{ (ly/day)} \quad (3-3)$$

$$Q_b = 1.14 \times 10^{-7} (273.16 + T_w)^4 (0.39 - 0.05 \sqrt{E_a}) (1 - 0.6 C^2) \text{ (ly/day)} \quad (3-4)$$

where u_* is the friction velocity of the atmosphere and is related to w_* by

$$w_* = \left(\frac{\rho_a}{\rho_w} \right)^{1/2} u_* \quad (3-5)$$

The non-dimensional drag coefficient (C_D) was assumed constant (1.3×10^{-3}) throughout this study and the saturation vapor pressure of the marine atmosphere (E_w) in direct contact with the ocean was estimated

from the observed sea-surface temperature. The final quantity (E_a) is the saturation vapor pressure of the atmosphere at a height of approximately 10 meters and was estimated from the dewpoint temperature. Additionally a daily estimate of the effective solar radiation was computed from the formula developed by Seckel and Beaudry (1973). A more complete description of the empirical formulas is presented in Appendix A, along with a discussion of their underlying assumptions.

C. CHARACTERISTIC ATMOSPHERIC AND OCEANIC CONDITIONS AT THE WEATHER STATIONS

Before proceeding to the details of modeling the upper ocean, the general character of the marine atmospheric forcing and oceanic response at the ocean weather stations will be examined to place this study in perspective.

During the fall and winter, the mean atmospheric circulation at OWS P and OWS V is dominated by a large barometric low pressure system (Aleutian Low), and the mean flow is generally westerly. The mean surface winds at OWS N are under the influence of the subtropic high and are generally northeasterly. However, the most outstanding feature of the mid-latitude atmosphere in the North Pacific is the fluctuations in the atmosphere associated with the frequency and intensity of travelling extratropical cyclones.

An analysis of historical storm tracks, presented in the U.S. Navy Marine Climatic Atlas (1957), indicates that OWS V and OWS P lie in close proximity to the preferred path of the major storm centers, while OWS N is located a considerable distance to the south. The influence that these storms have on air-sea interactions is therefore expected to be most pronounced at OWS V and OWS P and weakest at OWS N.

Figures 3-1 present a comparison of the long-term mean atmospheric forcing and oceanic thermal response at the three ocean stations. The atmospheric forcing and sea-surface temperature were computed from the three-hourly surface and near-surface observations while the bathythermograph file was used to establish the mixed-layer depth (defined as the depth at which the temperature was 0.2°C less than the sea-surface temperature). Each point represents the daily average of all available data (see Table 3-1) smoothed by a 7-day running mean (for display purposes only).

These figures are presented merely to illustrate the relative magnitude and variability of the atmospheric forcing and oceanic response that we might anticipate at the three stations. An important observation that should be made is that the air-sea interactions in the North Pacific are highly dependent upon geographical location. Since we are interested in evaluating model performance under a variety of geophysical situations, these three stations appear ideally suited for this study. It is also important to observe that there is a significant correlation between the strong, variable forcing and large oceanic response at OWS P and OWS V and the relatively weak, steady forcing and response at OWS N. In Chapter V a detailed analysis of these data will be performed, designed to understand the principal mechanisms by which these evolutions take place.

The North Pacific has been divided into distinctive ocean regimes (Tully, 1964) based on similarities in the characteristic temperature and salinity structures in these regions. OWS P is located in the Pacific Subarctic region while OWS V and OWS N are located in the Pacific Subtropic. Figures 3-2 illustrate schematically the major features of the ocean structure to be found in these regions.

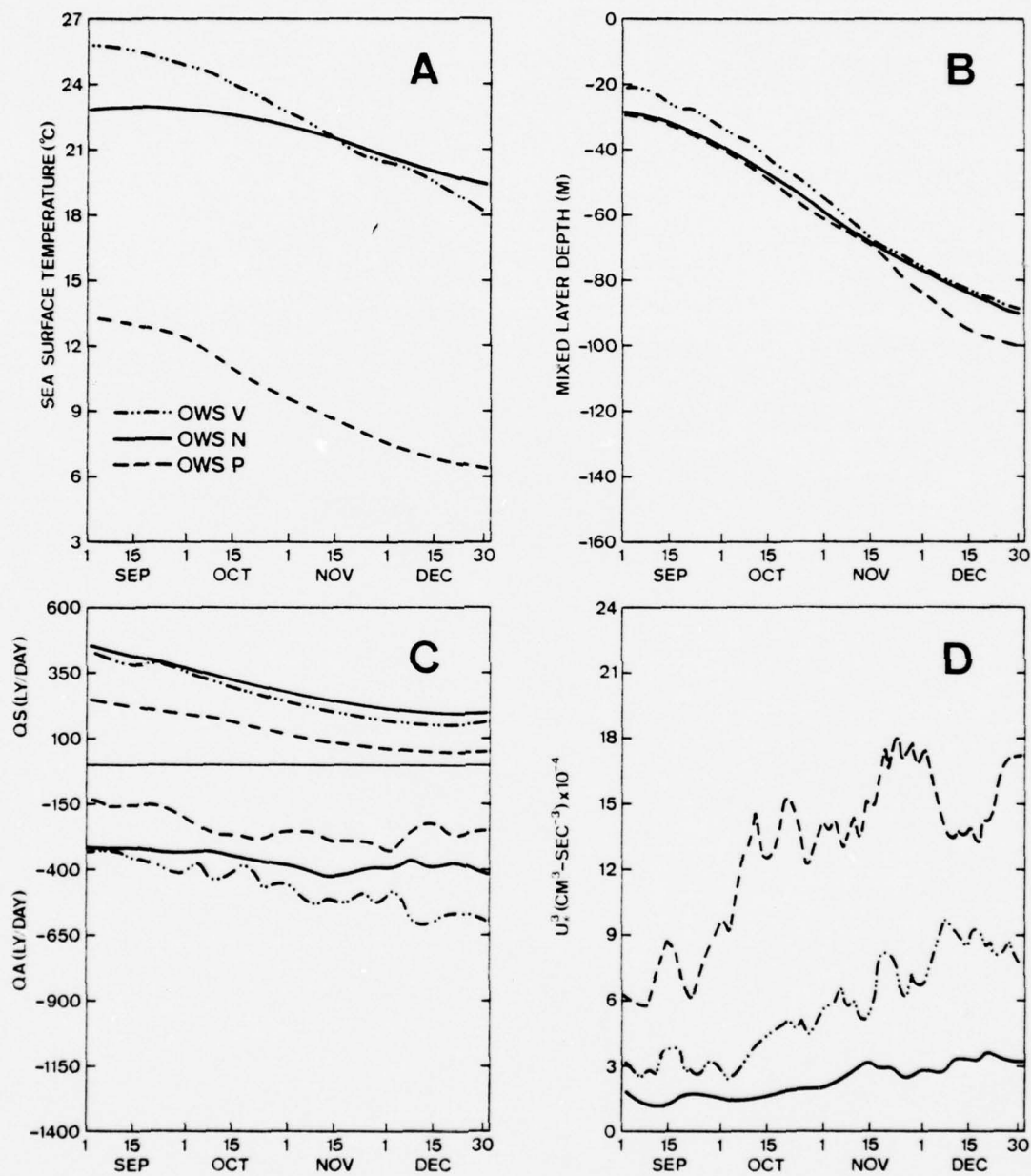


Figure 3-1. Long-term mean atmospheric forcing and oceanic thermal response at OWS P, OWS V, and OWS N.

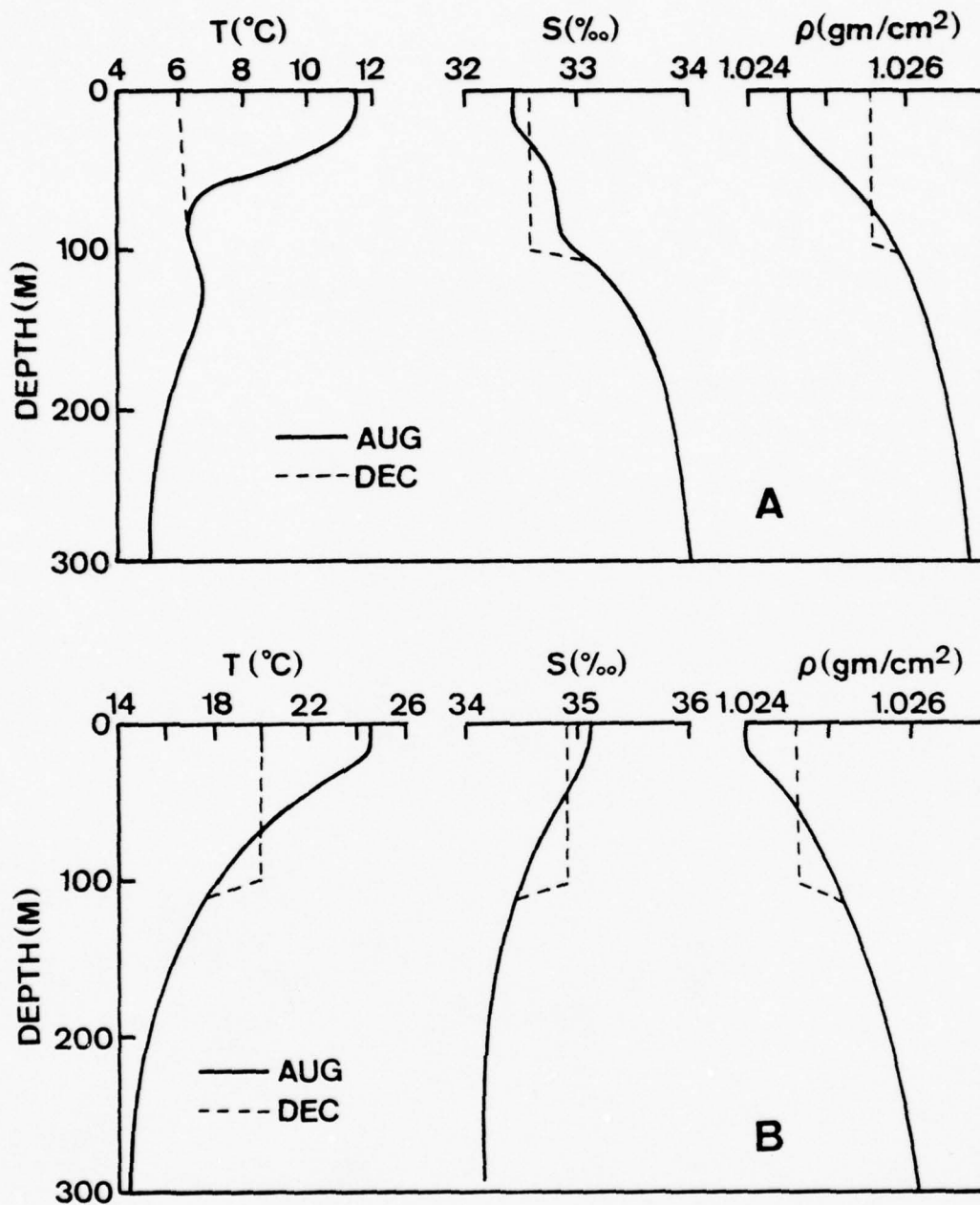


Figure 3-2. Major features of the ocean thermal structure in the North Pacific. (A) Pacific Subarctic Region (B) Pacific Subtropic Region (after Tully, 1964).

The Pacific Subarctic region is distinguished by excess precipitation ($E-P < 0$), large upward surface heat fluxes, and strong mechanical forcing through most of the cooling season. These quantities interact to create a unique temperature and salinity structure and the most distinctive feature to be noted in Fig. 3-2A is the existence of a stable salinity gradient in the upper ocean. Throughout this region the density structure is a function of both the temperature and salinity structure in the upper 100 m, with the salinity becoming increasingly more important at depths approaching the permanent halocline.

At OWS N and OWS V very similar temperature and salinity structures are observed (Fig. 3-2B) which are very different from OWS P. The Subtropic region is characterized by large surface heat fluxes and values of $E-P > 0$ through most of the cooling season. Consequently both temperature and salinity decrease with depth in the upper ocean and the density structure is primarily a function of the temperature structure in this region.

OWS P offers a unique opportunity to examine and model the effects that intense winter storms have on the upper ocean thermal structure. The largest vertical flux of turbulent kinetic energy (Fig. 3-1D) may be expected at this station throughout the season, and makes this an ideal location for examining the parameterizations of dissipation postulated by Kraus and Turner (1967), Kim (1976), and Elsberry, et al. (1976). Additionally, it should prove instructive to determine if the major thermal structure changes may be accounted for with a model that assumes that the density structure may be represented by only the temperature structure, and surface buoyancy flux by only the heat flux.

The study of the processes which control the evolution of the upper ocean at OWS V and OWS N offers an opportunity to examine these mechanisms

under different conditions than at OWS P. OWS V will be characterized by the largest upward surface heat fluxes (Fig. 3-1C) observed at any station together with large and variable energy fluxes. Therefore, both mechanical mixing and free convection may be expected to play important roles in modifying the thermal structure.

OWS N, on the other hand, is an excellent location for testing the model's performance under rather weak and steady forcing. Because of the characteristic ocean structure in the subtropics, neglecting salinity should not introduce any severe limitations on model performance at either OWS V or OWS N (see Dorman, 1974).

IV. RESPONSE OF THE UPPER OCEAN TO STRONG ATMOSPHERIC FORCING: OBSERVATIONS AND SIMULATIONS

A. INTRODUCTION

In this chapter we investigate the oceanic thermal response associated with strong autumn and early winter atmospheric forcing events at the three ocean weather stations. Denman and Miyake (1973) presented data from OWS P (13-24 June 1970) which illustrated the behavior of the upper ocean during the passage of several synoptic-scale weather systems. Further, they were able to simulate the major features of the mixed layer response to these summer storms using a numerical version of the Kraus-Turner model (1967). However, the response of the upper ocean to the strong fall and winter storm events has not been adequately investigated and has never been successfully simulated.

The atmospheric forcing associated with the strong events that occur during the fall and early winter seasons is typically much more energetic than the forcing observed during the strong summer events. In addition to large downward fluxes of mechanical energy, the fall and winter events are frequently characterized by large upward turbulent fluxes of latent and sensible heat. Therefore, mechanical mixing and convection play an increasingly important interactive role in the mixed layer evolution during the autumn and early winter seasons.

The principal objectives of this chapter are to examine data sets representing air-sea interactions at OWS P, OWS N, and OWS V to:

1. show that significant upper ocean thermal structure modifications occur during periods of strong fall and early winter forcing at the three ocean weather stations;

2. demonstrate that a modified version of the Kraus-Turner model (parameterized to account for dissipation enhancement and non-penetrative convection) is capable of simulating a large percentage of these changes;
3. establish the relative importance of the mechanical and convective processes that characterize the strong fall and early winter forcing events at the three ocean weather stations.

In this research the three one-dimensional, bulk models (specifically KT, EFT, and KIM), discussed in Chapter II, were evaluated at the three ocean weather stations. Successful simulation of the response of the upper ocean depends upon adequate parameterization of the principal physical processes which govern the response. The relative capabilities of the three models in simulating the mixed layer evolutions will be discussed in terms of the importance of properly parameterizing dissipation enhancement and non-penetrative convection.

B. PARAMETERIZATION OF THE MODELS

A modification of the algorithm presented by Thompson (1976) was developed to parameterize the KT, EFT, and KIM models in a consistent manner. The scheme was designed to calculate the potential energy changes resulting from the vertical fluxes of heat and turbulent kinetic energy that occur in the upper ocean. The sources and sinks of turbulent kinetic energy, specified in (2-40), are parameterized according to the KT, EFT, and KIM models. The modifications of the thermal structure by these vertical heat and energy fluxes are accomplished in a manner described in detail in Appendix B.

The time rate of change of the mixed layer temperature ($\frac{\partial T}{\partial t}$) and depth ($\frac{\partial h}{\partial t}$), specified by (2-21) and (2-33), are specified by the

vertical redistribution of heat by the turbulent energy fluxes. In Thompson's algorithm the temperature profile is stored in N equally-spaced grid intervals $[-(n-1)\Delta Z, -n\Delta Z]$, where $n=1,2,\dots,N$ and $\Delta Z = 2.5$ m. At each time step ($\Delta t = 1$ hr) the mixed-layer temperature is taken to be the temperature in the first interval. The scheme does not explicitly calculate the mixed-layer depth and it is simply defined (in the model and the BT data) as the depth at which the temperature is 0.2°C less than the mixed layer temperature.

The basic algorithm was evaluated by Thompson (1976) for the case of mechanical mixing with no radiation, and for surface cooling with no mechanical forcing. Numerical results from this scheme were equivalent to the analytical calculations for these cases. A desirable property of Thompson's algorithm is that it conserves heat and potential energy at each time step. This property is important because it allows us to isolate and compare the relative importance of mechanically generated turbulent kinetic energy and free convection in the modification of the upper ocean thermal structure.

C. INPUT DATA

The atmospheric forcing (w_*^3 , Q_s , Q_e , Q_h , Q_b) was estimated from the routine meteorological observations using the bulk formulas described in Chapter III and Appendix A. The turbulent energy fluxes (w_*^3 , Q_e , Q_h) were calculated every three hours and linearly interpolated to hourly values corresponding to the integration time-step used in the models. The calculated daily value of effective long-wave radiation (Q_b) was distributed uniformly over the 24 hours. The value of net short wave radiation (Q_s), however, varied as a function of the solar altitude. To approximate this effect, the estimated daily value was distributed sinusoidally from sunrise to sunset.

Since the forcing was calculated from the observed surface and near-surface parameters, there was no feedback possible between the ocean and the atmosphere. The models were purposely run in this uncoupled state to insure that each model received the same forcing. The different model responses may, therefore, be compared in terms of the differences in the internal physical mechanisms specified by each model. Additionally, since any errors in the forcing are introduced in each model, they should not adversely affect the relative comparison of the different model results.

The models were initialized using mechanical BT data from the NODC historical file at the three ocean weather stations. In choosing data sets for testing the performance of the models, the lack of BT data was the most limiting factor. During many strong forcing events the BT data were completely missing. Therefore, some data sets could only be initialized using observations which were available before the events and the results of the models validated using data obtained a few days after the events had passed. After examining many data sets, it was observed that the morning BT (within 2 hrs of 0800) provided a reliable indicator of the trend in the mixed-layer depth and temperature during the strong fall and winter events. The individual morning BT observations were examined and a number of simple gross error checks were made to insure that the observations were realistic. The trend in the sea-surface temperature in the BT observations was compared with the trend in the bucket temperature reported in the marine deck. If these two trends were not comparable, the data set was rejected. Additionally, the trend in the mixed-layer depth was examined to insure that it was compatible with the character of the computed atmospheric forcing. Finally, to guard against any single BT observation seriously biasing the results (especially the initial observation), the profiles used in the model were smooth by hanning. This

morning sampling rate prohibits resolution of model performance during time scales of less than one day. Therefore the analysis will focus on the relative capabilities with which the models simulate the general trend in the mixed layer changes on time scales of a few days to a few weeks.

Some of the variation in the mixed-layer depth in the individual BT observations can be attributed to internal waves with periods ranging from the Brunt-Väisälä period (1-10 min in the upper ocean) to the local inertial period (between 15.7 hrs at OWS P to 24 hrs at OWS N). The atmospheric events investigated in this study were primarily selected to include periods with impulsive increases in the wind speed. Inertial waves, investigated by Pollard (1970), and Pollard and Millard (1970), which are generated by these moving atmospheric disturbances probably account for some of the differences in mixed-layer depth between the model and data. However, since these internal oscillations have relative small effects on the sea-surface temperature, they are easily distinguishable from the changes over several days that are due to the turbulent processes parameterized in the models.

A total of 49 data sets (20 at OWS P, 16 at OWS N and 13 at OWS V) were finally accepted and modeled using the KT, KIM, and EFT models. The scale depth, Z , for the EFT model (see Eq. 2-53) was calibrated to six data sets (two from each ocean weather station). A value of $Z = 50$ m gave the best fit to the mixed layer depth, in these calibration experiments, and was used in all further applications of the EFT model. It should be noted, however, that none of the data sets chosen for presentation were among the six calibration sets.

In this chapter a total of five data sets will be presented (three from OWS P, and one each from OWS V and OWS N). They are illustrative of

the different atmospheric forcing and oceanic response characteristics that were observed at the three ocean weather stations during this study. The first four data sets were selected during periods when the mixed layer response appeared to be largely one-dimensional. That is to say, the local heat budget was maintained and a one-dimensional mixed-layer model, adequately parameterized to account for dissipation enhancement and partially-penetrative convection, was capable of simulating the mixed layer response. The relative performance of the three models will be examined using these data sets to gain insight into the problem of properly parameterizing the important vertical processes. The final data set was selected to illustrate the capability of the one-dimensional model during periods when non-local processes (e.g., advection) play a significant role in the evolution of the thermal structure.

D. CHARACTERISTICS OF THE ATMOSPHERIC FORCING AND OCEANIC RESPONSE AT OWS P

In this section three data sets from OWS P are examined to illustrate the characteristics of the upper ocean thermal response under the following set of atmospheric and oceanic conditions:

1. abnormally strong, impulsive mechanical forcing events occurring relatively early in the fall when the mixed layer is shallow;
2. steady atmospheric forcing (equal to the climatological average) occurring in the late fall when the mixed layer is deep;
3. alternate periods of strong and weak mechanical forcing, in the early fall, while the ocean is being heated.

The first example was selected from the period 7-19 October 1954. It is representative of the large upper ocean thermal structure modifications that were observed during periods of strong, impulsive mechanical

forcing events occurring early in the cooling season (10 of the 20 data sets at OWS P had similar forcing). Figures 4-1 to 4-2A present the relationships between the atmospheric forcing, the observed mixed layer response, and the relative performance of the KT, EFT, and KIM models in simulating the response.

In Fig. 4-1A the atmospheric forcing is represented as daily averages of the surface stress (τ_s), the effective insolation (Q_s), the sum of the latent and sensible heat (Q_T), and the net heat exchange at the sea surface (Q_n). In this chapter a positive heat flux represents an upward flux. To illustrate the relative strength of the forcing during this experiment it was determined that 70% of the turbulent kinetic energy and 81% of the net surface heat fluxes for the month of October 1954 were exchanged during the period 7-19 October (42% of the month). Furthermore, comparing the forcing received during October 1954 with the long-term mean forcing for October (see Fig. 3-1) showed that the turbulent kinetic energy flux was 120% larger than normal while the net surface heat flux was about average during October 1954.

The surface stress is characterized by three distinct peaks (events) centered on 11, 14, and 17 October 1954. The net surface cooling (Q_T) has only one peak on 11 October 1954 which does not occur with the largest peak in the stress. The magnitude of Q_T , as specified by (3-2) and (3-3), depends to a large degree upon the magnitude of the air-sea temperature and vapor pressure differences, in addition to the wind speed. These air-sea differences were smaller during the second event than during the first and third events.

The response of the mixed layer during this period is depicted in Fig. 4-1B, along with the response of the KT, EFT, and KIM models. The

BEST AVAILABLE COPY

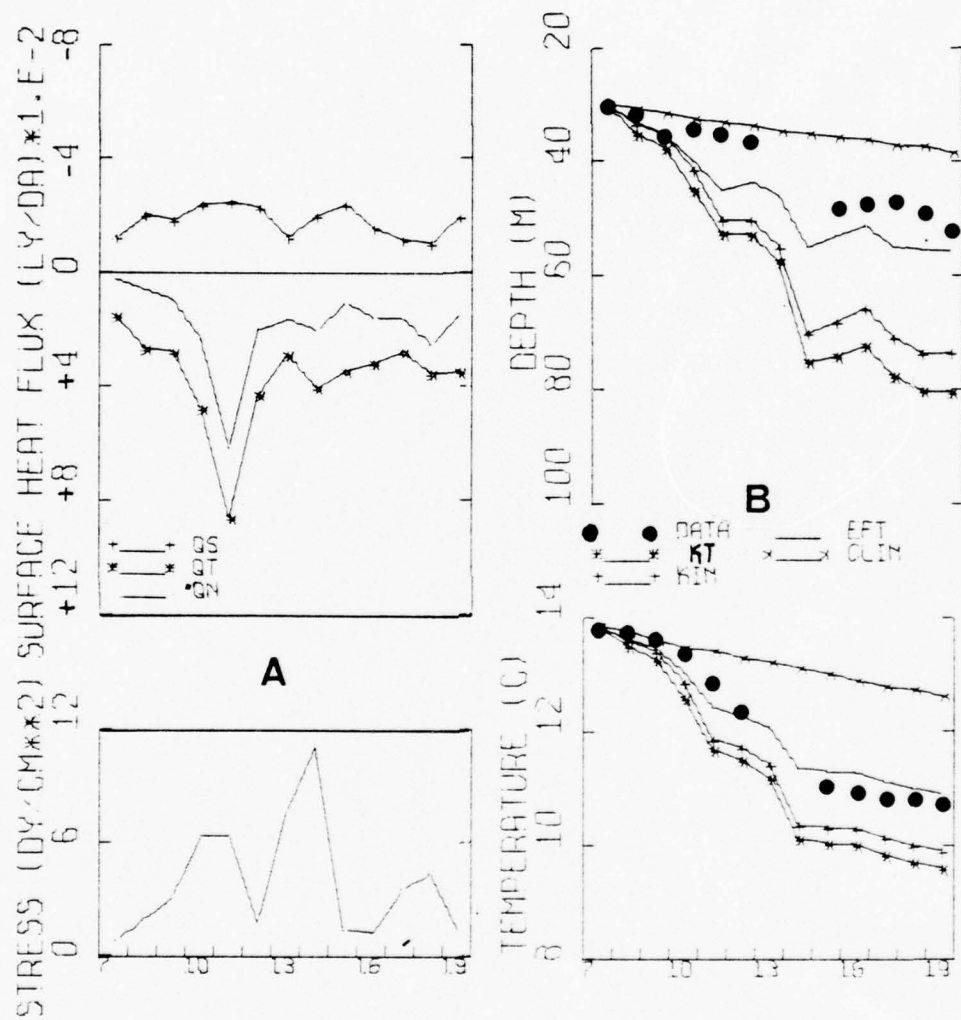


Figure 4-1. Atmospheric forcing and observed and predicted mixed layer response at OWS P during the period 7-19 October 1954.

long-term mean trend (CLIM) is displayed as a basis for comparing the mixed layer response. During this experiment the observed mixed-layer depth and temperature (30-52 m, 13.9-10.8°C) were abnormally large compared with CLIM (30-39 m, 13.9-12.6°C). It should also be observed that the mixed layer response predicted by the EFT model compared favorably with the general trend in the data (30-55 m, 13.9-10.9°C). The KIM model (30-73 m, 13.9-9.9°C) and KT model (30-81 m, 13.9-9.6°C) predicted excessive deepening and cooling.

Figure 4-2 depicts the capability of the EFT model in predicting the thermal structure modifications during the period. The agreement between the data and model temperature profile is generally quite good with the exception of the abnormally large temperature gradient predicted below the mixed layer. In an attempt to correct this undesirable property, vertical diffusion was added to the models. The temperature change due to diffusion was specified according to:

$$\frac{\partial T}{\partial t} = A_v \frac{\partial^2 T}{\partial z^2} \quad (4-1)$$

where A_v is the vertical diffusion coefficient. A constant value of $A_v = 0.5 \text{ cm}^2\text{-sec}^{-1}$, as used by Haney and Davies (1976), gave acceptable results in the data sets modeled in this study. The diffusion tendency was calculated at each time step with the Euler scheme and added to the profile after the turbulent mixing processes were calculated. A zero-flux condition was assumed at the top and bottom of the profile. The resulting accumulation of heat at the bottom was not significant for the integrations performed in this study (less than a month in all cases).

Figure 4-2A shows the results of the EFT model including diffusion. It is clear that the model with diffusion more realistically represents

BEST AVAILABLE COPY

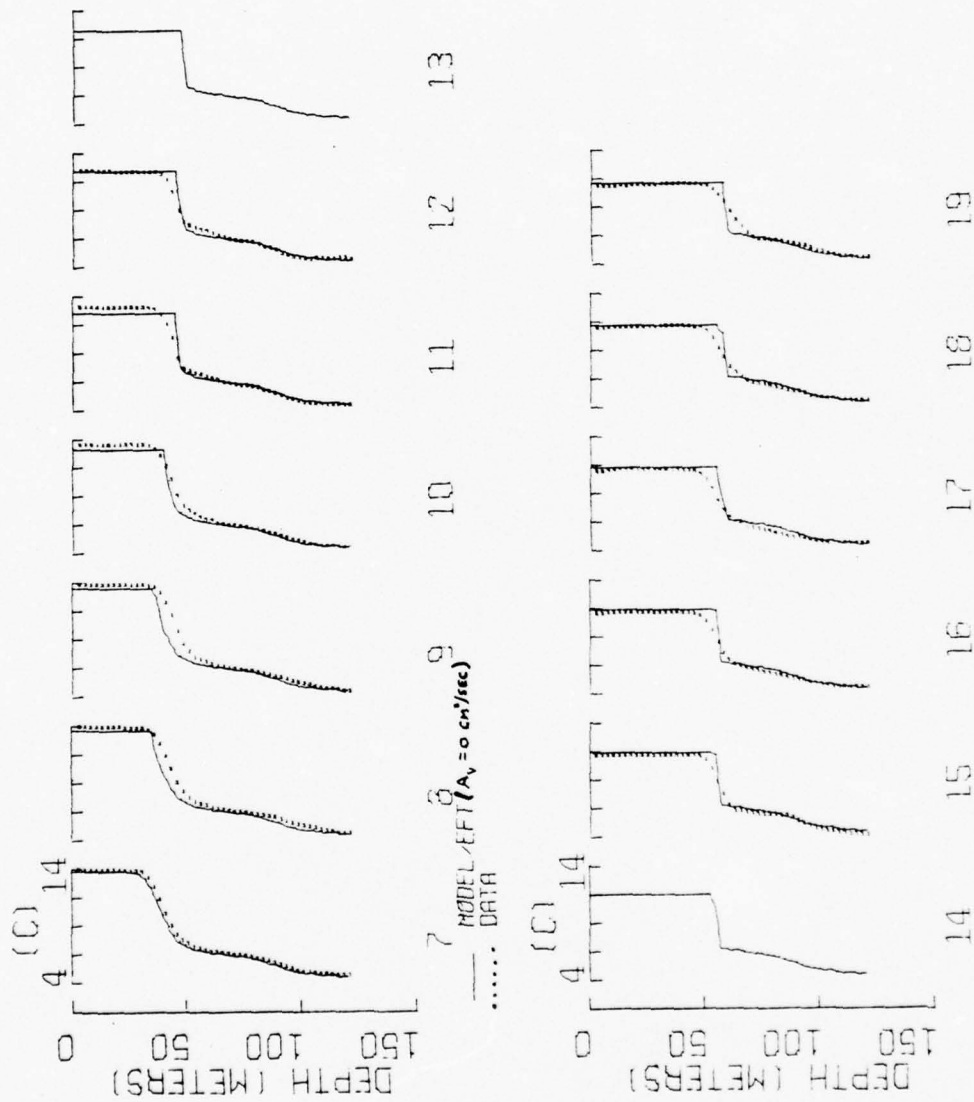


Figure 4-2. Observed and predicted (EFT model) thermal structure for the period 7-19 October 1954, with vertical diffusion neglected ($A_v = 0$).

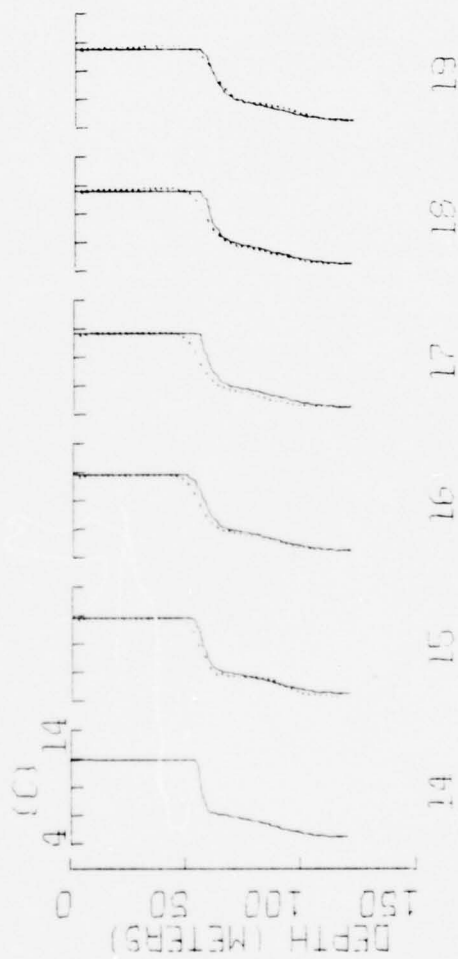
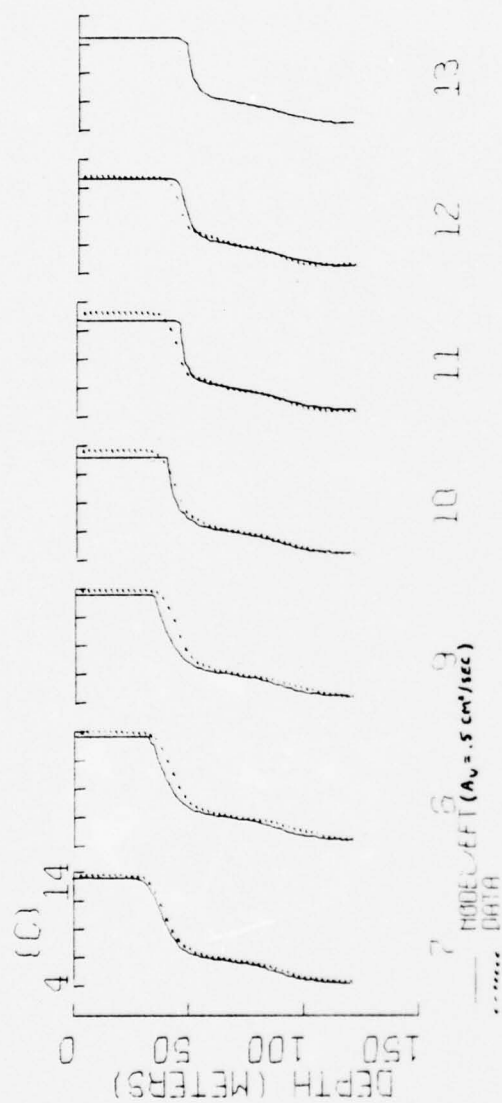
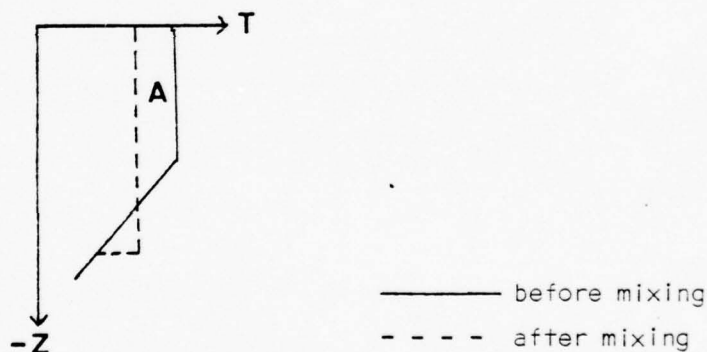


Figure 4-2a. Same as Figure 4-2 except vertical diffusion included ($A_v = .5 \text{ cm}^2 \text{ sec}^{-1}$).

the structure of the upper thermocline during this experiment. Additionally, the diffusion results in a predicted mixed layer which was 0.1°C cooler and 2 m shallower because of the additional downward heat flux. It was concluded that vertical diffusion was an effective means for preventing abnormally large temperature gradients, and hereafter was included as an integral part of all the models.

As indicated by (2-21) the temperature of the mixed layer is modified by the net heat flux at the air-sea interface (Q_n) and the downward entrainment heat flux at the base of the deepening mixed layer ($\overline{w'T'}(h) = -\Lambda \frac{\partial h}{\partial t} \Delta T$). Figure 4-3 depicts the relative magnitude of Q_n calculated from the marine observations and $\overline{w'T'}(h)$ calculated from the three models (for example BASE/EFT). Also included in this figure is an estimate of the entrainment heat flux from the data (BASE/OBS). BASE/OBS is the change



of heat content represented by area A in the schematic, less the contribution of the surface heat flux (Q_n). For instance if $Q_n > 0$, the contribution during the deepening would be to increase A and therefore Q_n must be subtracted. If $Q_n < 0$, Q_n is added to the heat content in area A. If the local heat balance is maintained during this evolution, then this calculation will be representative of the entrainment heat flux. Both measurement errors and non-local processes contribute to errors in this estimate of entrainment heat flux.

Figure 4-3A indicates that the cumulative entrainment heat flux calculated by the EFT model (-8350 ly) was in good agreement with BASE/OBS (-9200 ly). The KT (-16,850 ly) and KIM (-15,400 ly) models calculated unrealistically large entrainment heat fluxes because of the excessive mixed-layer depth predicted by these models. It should be noted, however, that the entrainment heat flux, calculated by the EFT model, is much larger in magnitude than the surface heat flux (+2400 ly) during this period. Therefore, according to (2-21), the principal mechanism accounting for the large sea-surface temperature change observed in the data was the downward flux of heat occurring during entrainment. The important implication is that during these large mechanically forced events, an accurate prediction of the sea-surface temperature depends, to a large extent, on the accurate specification of the entrainment heat flux. This is synonymous, in the models, with an accurate determination of the potential energy changes that result from mechanical mixing and convection (see Eq. 2-49).

Figure 4-3B depicts the changes in the potential energy as calculated by the EFT model. It should be observed in Figs. 4-1B and 4-3A that the curves representing $\frac{\partial h}{\partial t}$ and $\overline{w'T'(h)}$ are mirror images of the changes in potential energy due to mechanical mixing represented in Fig. 4-3B. It is significant to note, however, that in Fig. 4-1B the curve depicting $\frac{\partial T_s}{\partial t}$ is also similar in shape to $\frac{\partial h}{\partial t}$, $\overline{w'T'(h)}$ and $\frac{\partial PE}{\partial t}$ (the time rate of change of total potential energy). The similarity in the shape of these curves is characteristic of all data sets in which the vertical heat fluxes at the base of the layer dominated the heat budget of the mixed layer.

The differences in the performance of the EFT, KT and KIM models may be examined in terms of the potential energy budgets calculated by each

BEST AVAILABLE COPY

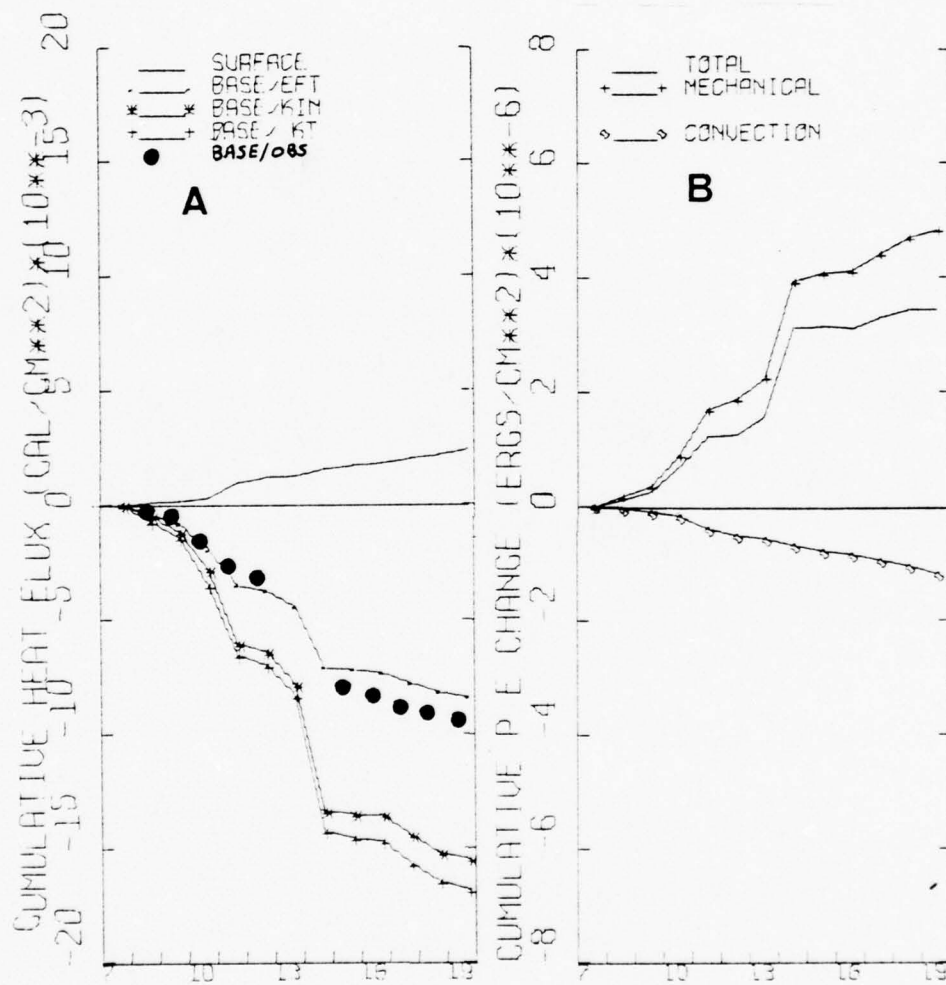


Figure 4-3. (A) Relative importance of the vertical heat fluxes and (B) Potential energy modifications calculated by the EFT model during the period 7-19 October 1954.

model. Table 4-1 presents a comparison between the total surface heat flux (ΣQ_n) and the total entrainment heat flux ($\Sigma \overline{w'T'}(h)$) estimated from the data and from the model results. The final three columns represent the total potential energy change ($\Sigma \Delta PE$), the total potential energy increase due to mechanical mixing ($\Sigma \Delta PE_m$), and the total reduction in potential energy due to convection ($\Sigma \Delta PE_c$). These three quantities are related as follows:

$$\Sigma \Delta PE = \Sigma \Delta PE_m + (1-r) \Sigma \Delta PE_c, \quad (4-2)$$

where r is the fraction of convectively-generated turbulent kinetic energy available for entrainment and is taken as 0.15.

Comparing $\Sigma \Delta PE_m$ for the three models it may be observed that in the KT and KIM models, considerably more turbulent kinetic energy is available for entrainment than in the EFT model. It should also be noted, comparing $\Sigma \Delta PE_m$ with $\Sigma \Delta PE_c$, that convection was not as important as mechanical mixing during this period. An examination of $\Sigma \Delta PE_c$ shows that the largest reduction in potential energy is calculated by the KT model because the mixed layer is deepest and therefore convection occurs over a deeper depth (see Eq. 2-51). The net result is that $\Sigma \Delta PE$ is largest in the KT model and smallest in the EFT model.

It may easily be demonstrated that the abnormally large mixed-layer depth and temperature changes predicted by the KT and KIM models are due to the large amount of turbulent kinetic energy available for entrainment. One may express (2-33) as

$$\left(\frac{\partial h}{\partial t}\right)_m = \frac{2(G_* - D_* - S_*)}{n\Delta b} \quad (4-3)$$

where $\Delta b = \rho_o g \alpha \Delta T$.

TABLE 4-1. Model and data comparison at OWS P for the period 7-19 October 1954.
(Asterisks indicate quantities that could not be computed.)

MODEL	ΣQ_n (Langley)	$\Sigma W'T'(-h)$ (Langley)	$\Sigma \Delta PE(x 10^{-6})$ (ergs-cm ⁻²)	$\Sigma \Delta PE_m(x 10^{-6})$ (ergs-cm ⁻²)	$\Sigma \Delta PE_c(x 10^{-6})$ (ergs-cm ⁻²)
KT	+ 2450	-16,850	+10.43	+11.65	- 1.44
KIM	+ 2450	-15,440	+ 8.41	+ 9.44	- 1.27
EFT	+ 2450	- 8,350	+ 3.71	+ 4.66	- 1.11
DATA	+ 2450	- 9,200	*	*	*

Thus the response to mechanical mixing, $(\frac{\partial h}{\partial t})_m$, is the ratio of the turbulent kinetic energy available for entrainment ($G_* - D_* - S_* = \Sigma \Delta PE_m$) to the amount of work necessary to entrain the denser fluid from below the mixed layer ($h\Delta b$). An examination of the models indicated that $h\Delta b$ increased throughout the period 12-19 October, and that it was largest in the KT model and smallest in the EFT model. Therefore, the excessive mixed layer depth response in the KT and KIM models relative to the EFT model and the data, was primarily due to the numerator of (4-3). The lack of dissipation enhancement in the KT model, and the linear parameterization in the KIM model, are inadequate during this experiment. However, the data $(\frac{\partial h}{\partial t})$ and $\frac{\partial T_s}{\partial t}$ in Fig. 4-1B) suggest that the exponential parameterization of the EFT model was reasonable during these events. Comparing $\Sigma \Delta PE_m$ between the KT and EFT models shows that the EFT model calculates a dissipation rate equal to 60% of the surface production rate. In the KIM model, however, dissipation and storage were only 35% of the surface production.

The mixed-layer depths and temperatures, predicted by the EFT model, were quite good, and $\Sigma \overline{w'T'}(h)$ estimated from the data was in close agreement with $\Sigma \overline{w'T'}(h)$ calculated in the EFT model. This suggests that the potential energy changes calculated by the EFT model should be reasonable compared with the potential changes occurring in the upper ocean (which are not easily calculated over short time periods).

It is important to recognize the important contribution of the entrainment heat flux during these large mechanically forced events. The sea-surface temperature is reduced during the fall and winter not only by surface cooling but also by the vertical re-distribution of the heat by mechanical mixing. The implication to modeling the upper ocean response

is that an accurate prediction of the changes in the mixed-layer depth is essential for an accurate prediction of the sea-surface temperature response.

The second case to be examined was chosen during the period 22 November-12 December 1957. It is representative of the upper ocean thermal response that occurs later in the season when, relative to the previous example, the mechanical forcing is weaker and less impulsive. In contrast to the previous case, however, the net surface cooling that occurred during this period was larger and, as will be demonstrated, plays a more important role in the evolution of the mixed layer. The surface stress, depicted in Fig. 4-4A, is rather steady during this period, with the exception of two weak events centered on 26 November and 6 December 1957. The net surface cooling is also steady with no large peaks. Comparisons between u_*^3 and Q_T with the climatological trend (Fig. 3-1) showed that the transfer of turbulent kinetic energy during this period was about average (104% of the normal value). However, more surface cooling occurred during this period than the average (120 ly/day more than climatology). The mechanical forcing in this data set is typical of 9 of the 20 data sets investigated at OWS P.

It may be observed from DATA in Fig. 4-4B that the response of the upper ocean thermal structure (58-78 m, 10.1-8.7°C) was very close to the long-term mean trend (58-77 m, 10.1-9.0°C). It should also be observed that this steady response was closely simulated by the EFT model (58-80 m, 10.1-8.6°C) while the KT (58-118 m, 10.1-8.0°C) and KIM (58-104 m, 10.1-8.0°C) models again predicted excessive deepening and cooling rates. The structure modifications predicted by the EFT model, shown in Fig. 4-5, also agree very closely with the data. The model not

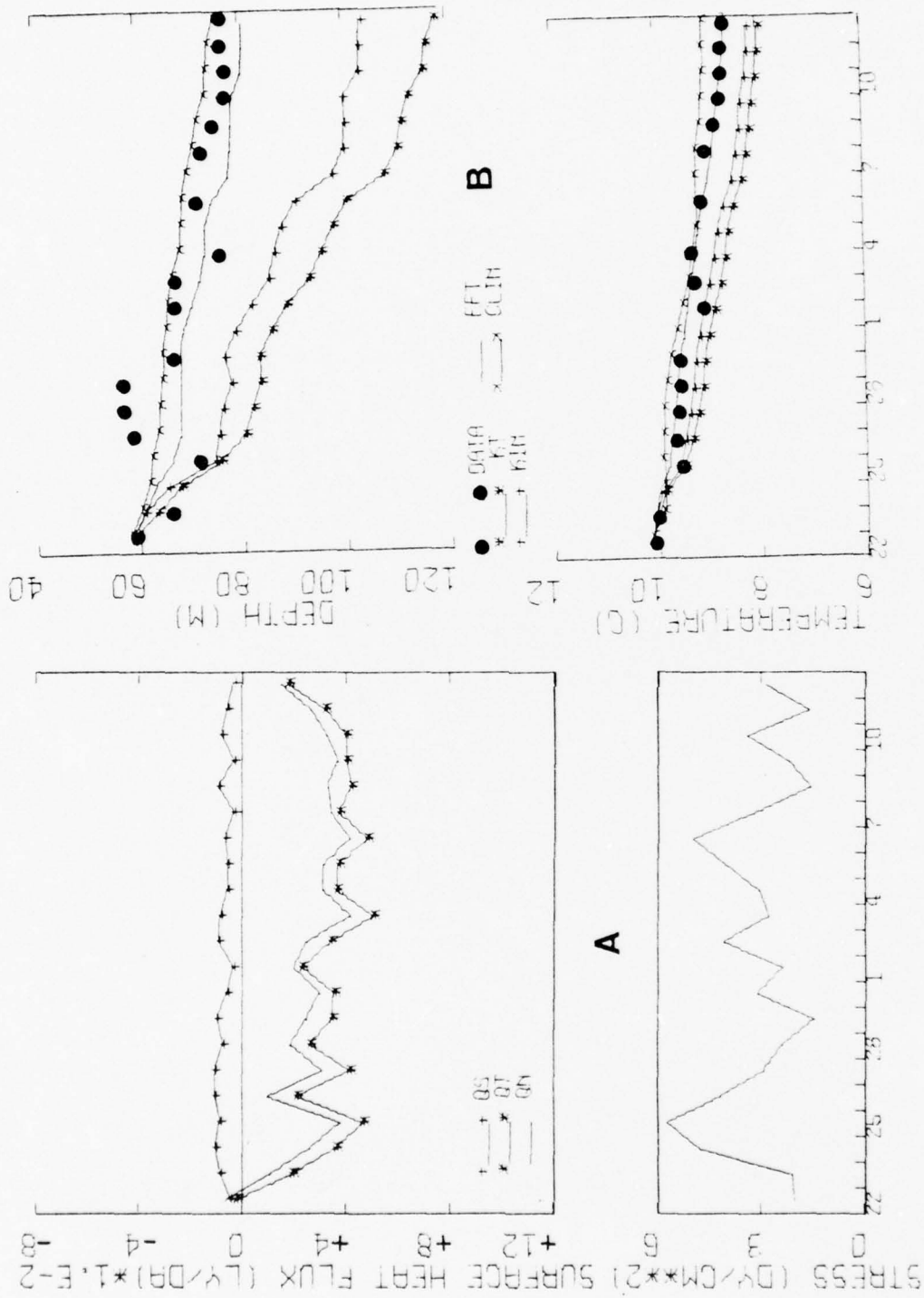


Figure 4-4. Same as Figure 4-1 except for the period 22 November 1957 - 12 December 1957.

BEST AVAILABLE COPY

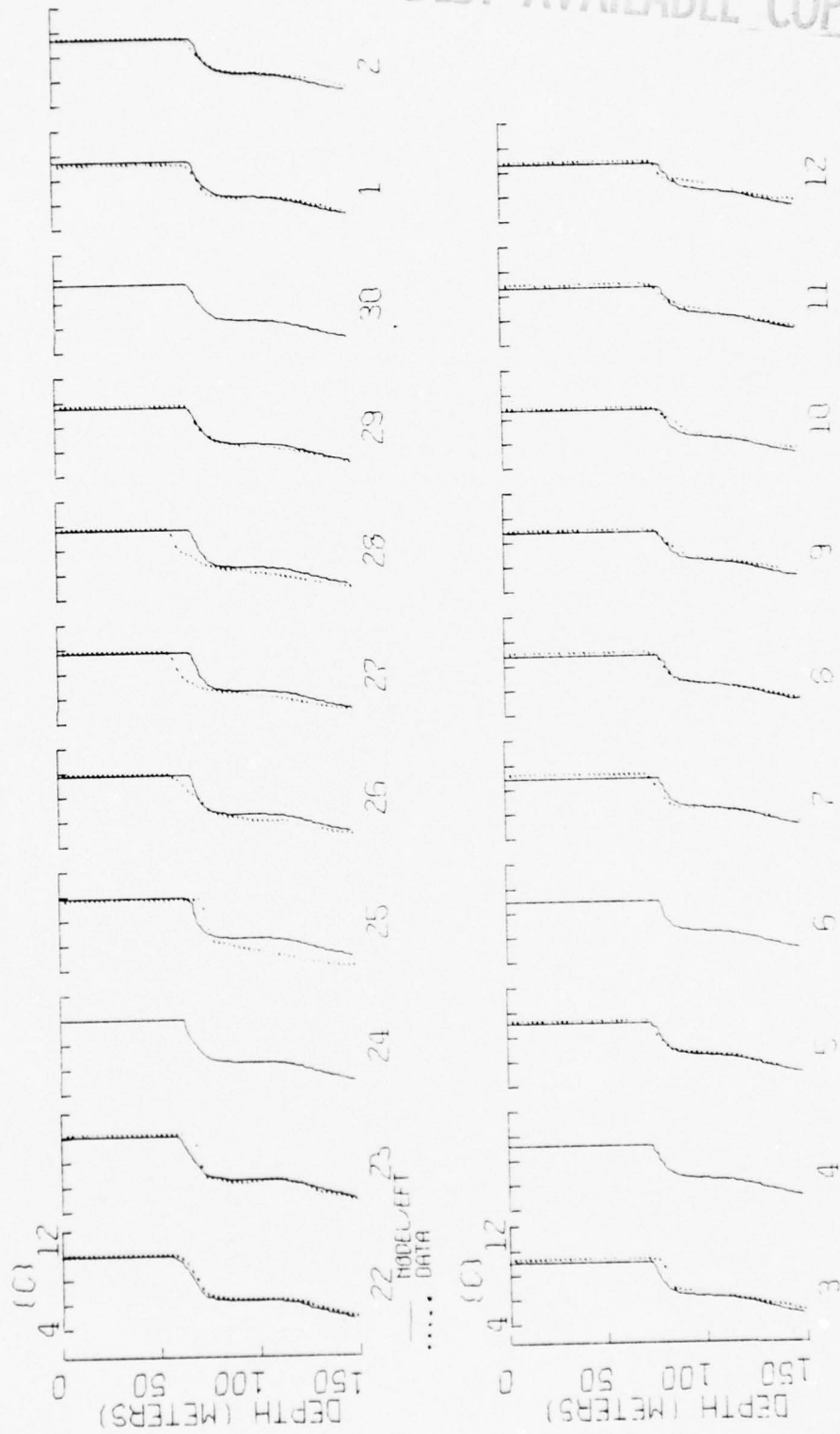


Figure 4-5. Same as Figure 4-2a except for the period 22 November 1957 - 12 December 1957.

only predicted approximately the correct mixed-layer temperature and depth, but accurately simulates the reduction in the temperature gradient (ΔT) immediately below the mixed layer. As shown by Gill and Turner (1976) the reduction of ΔT during these deepening events is primarily caused by non-penetrative convection. Equation (4-3) may be examined to verify that a reduction in ΔT results in the reduction of $h\Delta b$ and, therefore, an increase in $(\frac{\partial h}{\partial t})_m$. The reduction in ΔT is the principal mechanism by which convection interacts with mechanical mixing to permit further mechanical deepening of the mixed layer.

In Fig. 4-6A and Table 4-2 it should be observed that during this period the total net surface heat flux (+5497 ly) was considerably larger than the entrainment heat flux estimated from the data (-2972 ly), or calculated by the EFT model (-3481 ly). Note also that the entrainment heat flux calculated by the EFT model is again in good agreement with the estimate from the data. The KT (-10240 ly) and KIM (-8132) models again calculated abnormally large entrainment fluxes (because of inadequate dissipation) and as a consequence overestimated $\frac{\partial h}{\partial t}$.

The potential energy change observed in Fig. 4-6B and Table 4-2, calculated by the EFT model, is very different than in the previous data set (see Fig. 4-2B and Table 4-1). With the exception of the initial increase during the first few days, the general trend is for the potential energy to decrease during the period. As a result the characteristic shapes of the curves representing $\frac{\partial PE}{\partial t}$, $\frac{\partial h}{\partial t}$, and $\frac{\partial T_s}{\partial t}$ are not similar as in the previous example. This property is characteristic of the EFT model when convection plays a dominant role in the evolution of the upper ocean. The potential energy changes calculated by the KT and KIM models may be examined in Table 4-2 to see that a total increase in

BEST AVAILABLE COPY

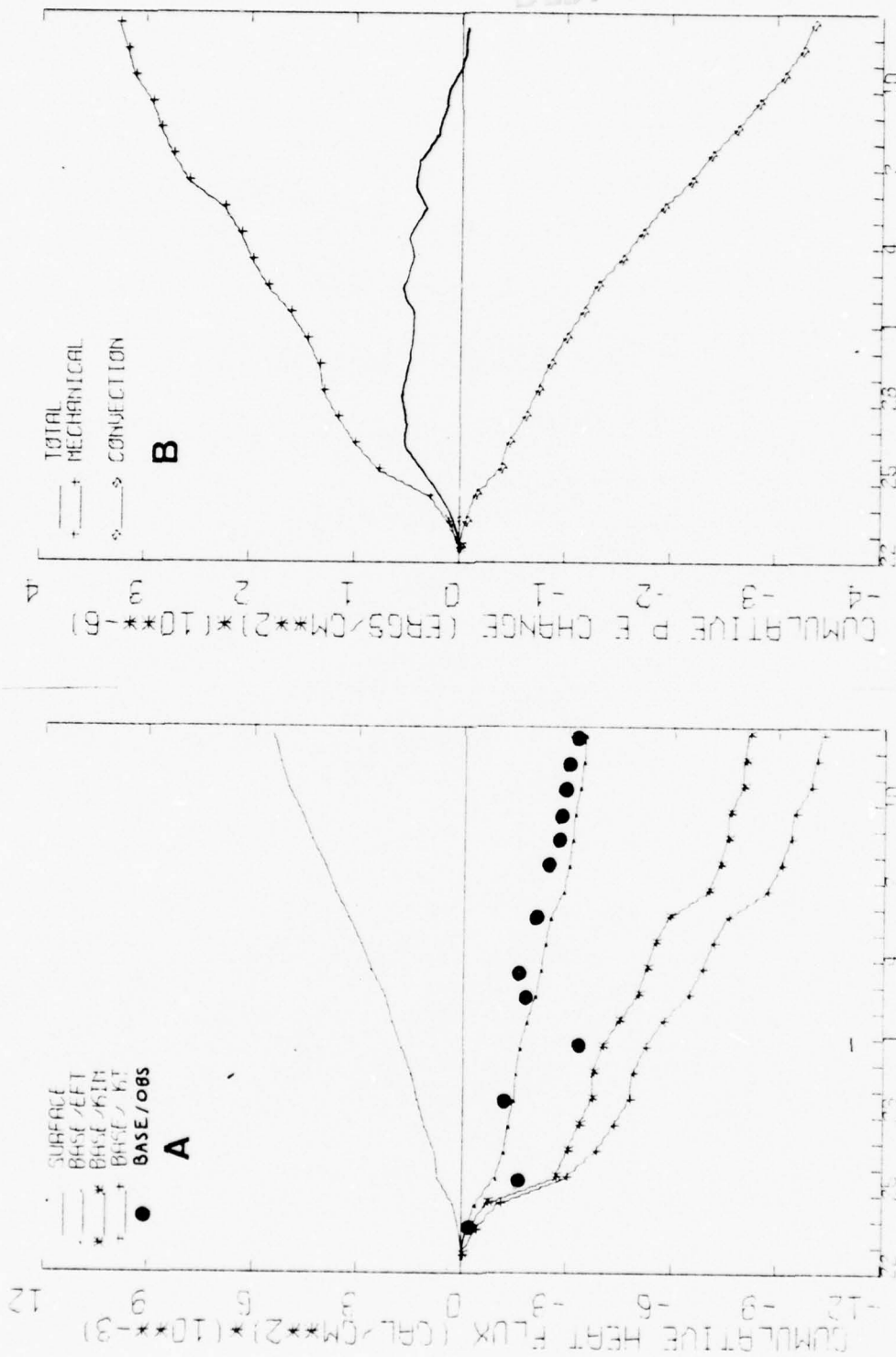


Figure 4-6. Same as Figure 4-3 except for the period 22 November 1957 - 12 December 1957.

TABLE 4-2. Model and data comparison at OWS P for the period 22 Nov - 12 Dec 1957.
(Asterisks indicate quantities that could not be computed.)

MODEL	ΣQ_n (Langley)	$\Sigma WTT(-h)$ (Langley)	$\Sigma \Delta PE(x 10^{-6})$ (ergs-cm ⁻²)	$\Sigma \Delta PE_m(x 10^{-6})$ (ergs-cm ⁻²)	$\Sigma \Delta PE_c(x 10^{-6})$ (ergs-cm ⁻²)
KT	+5497	-10,240	+6.93	+10.60	- 4.45
KIM	+5497	- 8,132	+4.06	+ 7.35	- 3.99
EFT	+5497	- 3,481	-0.07	+2.68	- 3.34
DATA	+5497	-2,972	*	*	*

potential energy resulted in both models. However a comparison of $\frac{\partial h}{\partial t}$, $\frac{\partial T_s}{\partial t}$, and $\Sigma \overline{w'T'}(-h)$ between the models and the data suggests that $\frac{\partial PE}{\partial t}$ calculated by the KT and KIM model is unreasonable. These comparisons further indicate that $\frac{\partial PE}{\partial t}$ calculated by the EFT model should be representative of $\frac{\partial PE}{\partial t}$ occurring in the upper ocean during this period.

The excessive deepening and cooling ratio predicted by the KIM and KT models may again be related to an inadequate parameterization of dissipation enhancement. In the EFT model the dissipation rate was 75% of the surface production rate while in the KIM model the dissipation and storage rate was only 55%. This is to be compared with the 60%/35% calculated in the EFT/KIM model in the previous example. The increased dissipation during this second case is the result of a deeper mixed-layer in this example (58-78 m) relative to the previous case (30-52 m), and the dissipation parameterizations defined by (2-53) and (2-53A). As with the previous example the large $\Sigma \Delta PE_m$ calculated by the KT and KIM models result in a serious overestimate of $\frac{\partial h}{\partial t}$ and $\frac{\partial T_s}{\partial t}$.

It should be observed in Tables 4-1 and 4-2 that for the EFT model $\Sigma \Delta PE_m$ was smaller in the second example than in the first. However, it may be observed in Figs. 4-1B and 4-4B that $\frac{\partial h}{\partial t}$ is comparable in both cases but $\frac{\partial T_s}{\partial t}$ was much smaller in the second case. One can see from Eq. (4-3) that since $G_* - D_*$ is smaller in the second case, $h \Delta b$ must also be smaller for $\frac{\partial h}{\partial t}$ to be comparable. Since h was also larger in the second case, the gradient at the base of the mixed layer must be

smaller, which may be confirmed in Figs. 4-3 and 4-5. If we simply express (2-20) as

$$\frac{\partial T_s}{\partial t} = \frac{\Sigma Q_n + \Sigma \overline{w'T'}(-h)}{h} \quad (4-4)$$

then the smaller decrease in the sea-surface temperature during the second case, relative to the first, is understandable. Comparing ΣQ_n and $\Sigma \overline{w'T'}(-h)$ in Tables 4-1 and 4-2 shows that the sum of the net surface and entrainment heat fluxes were smaller in the second case and, as previously mentioned, the mixed-layer depth was larger. Equation (4-4) would therefore explain the smaller $\frac{\partial T_s}{\partial t}$ in the second case. Equations (4-3) and (4-4) indicate that, for comparable forcing, a larger mixed layer response ($\frac{\partial h}{\partial t}$ and $\frac{\partial T_s}{\partial t}$) will take place when the layer is shallow than when it is deep. The important implication is that the large storms which take place early in the cooling season will have a much larger effect on the mixed-layer depth and temperature than those occurring relatively later.

The final data set to be presented in this section was selected for the period 1-15 September 1966. It is illustrative of conditions, in early September, when the mechanical forcing is characterized by alternate periods of relatively strong and weak forcing, and when net surface heating is occurring. Under these conditions the mixed layer frequently deepens during the strong forcing and retreats during the weak forcing periods (see Chapter II, Eq. (2-43) for a discussion of this process). It will be demonstrated that a proper parameterization of dissipation is essential to simulate this type of ocean response.

An examination of Fig. 4-7A shows that the mechanical forcing is characterized by three events, centered on September 4, 8, and 12, and the beginning of a fourth event on September 14. Further it should be observed from Fig. 4-7A and 4-9A that net surface heating takes place throughout most of this period, while the mixed-layer temperature is decreasing (Fig. 4-7B). Because net surface heating is occurring while $\frac{\partial T_s}{\partial t} < 0$, (4-4) shows that the decrease in the sea-surface temperature is entirely due to the entrainment heat flux. Therefore during periods characterized by net surface heating, the sea-surface temperature change is predictable only if the entrainment process is properly parameterized.

In response to this alternately weak and strong mechanical forcing, the predicted mixed layer depth alternately retreats and deepens (Fig. 4-7B). Figures 4-7B and 4-8 illustrate that the EFT model simulates the evolution of the mixed layer quite well during this period. As expected, the KT model consistently predicts a deeper, cooler mixed layer than the KIM and EFT models. However, during this period, contrary to the previous examples, the KIM model predicts a warmer and shallower mixed layer than the EFT model. The exception to this is during the periods following the first and second events. This suggests that less turbulent kinetic energy is available for entrainment in the KIM model than in the EFT model, except during the peaks in the forcing.

Table 4-3 may be examined to show that the three different predicted mixed layer responses are due to the different assumptions regarding dissipation enhancement. Comparing $\Sigma \Delta PE_c$ and $\Sigma \Delta PE_m$ it may be observed that convection played a relatively minor role during this period. The interesting observation is that $\Sigma \Delta PE_m$ is larger in the EFT model than in the KIM model (as the observations from Fig. 4-7B suggest). This is

BEST AVAILABLE COPY

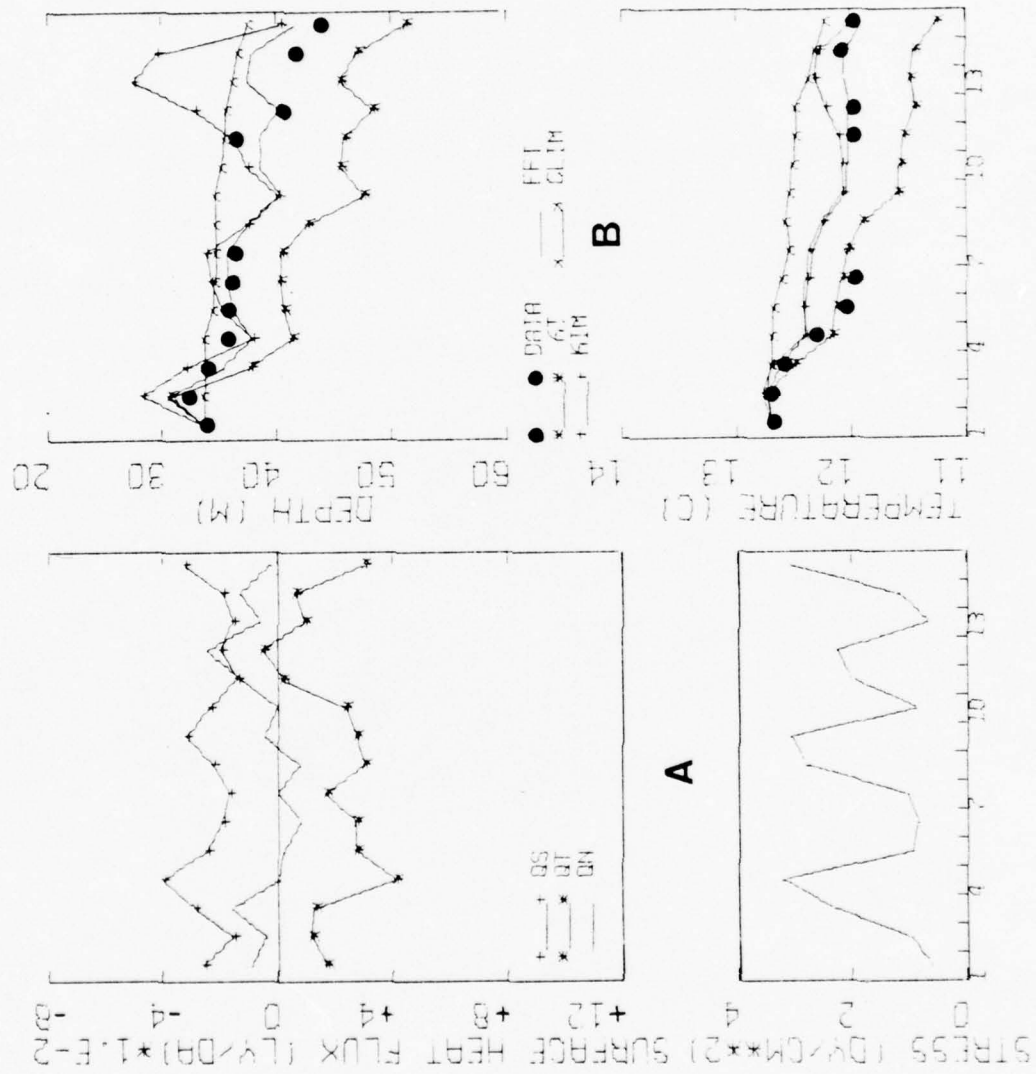


Figure 4-7. Same as Figure 4-1 except for the period 1-15 September 1966.

BEST AVAILABLE COPY

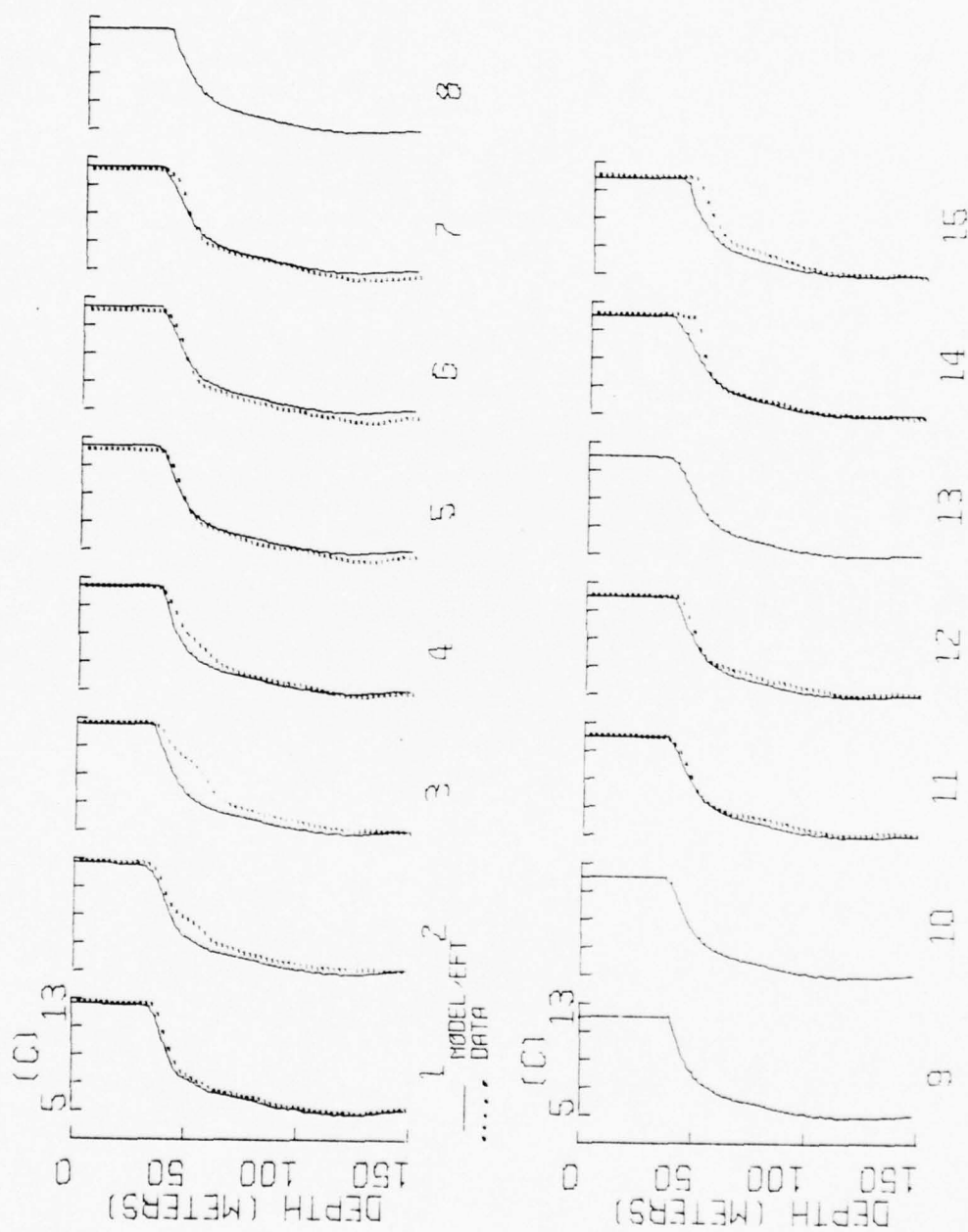


Figure 4-8. Same as Figure 4-2a except for the period 1-15 September 1966.

BEST AVAILABLE COPY

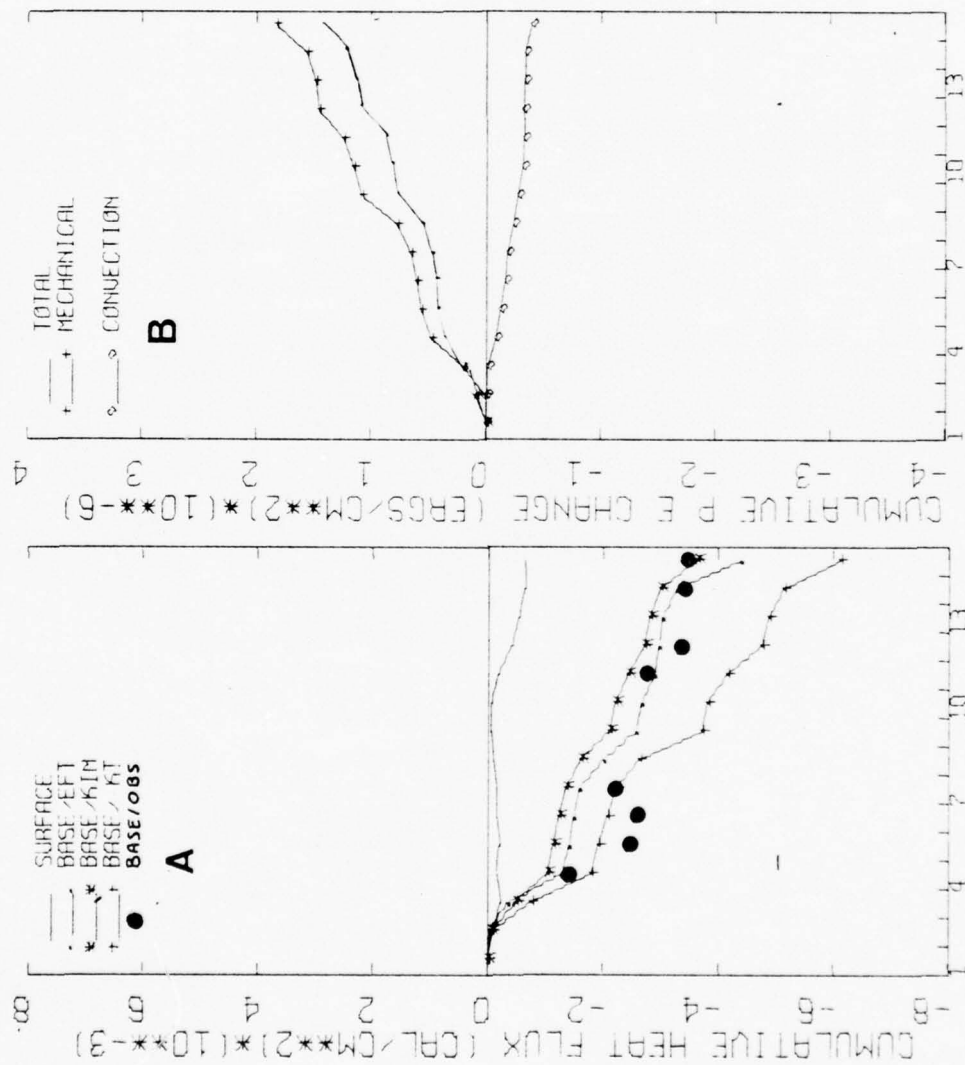


Figure 4-9. Same as Figure 4-3 except for the period 1-15 September 1966.

TABLE 4-3. Model and data comparison at OWS P for the period 1-15 September 1966.
(Asterisks indicate quantities that could not be computed.)

MODEL	ΣQ_n (Langley)	$\Sigma W'T'(-h)$ (Langley)	$\Sigma \Delta PE (x 10^{-6})$ (ergs-cm ⁻²)	$\Sigma \Delta PE_m (x 10^{-6})$ (ergs-cm ⁻²)	$\Sigma \Delta PE_c (x 10^{-6})$ (ergs-cm ⁻²)
KT	- 628	- 6,360	+3.09	+3.48	- 0.47
KIM	- 628	- 3,925	+1.26	+1.53	- 0.33
EFT	- 628	- 4,862	+1.46	+1.78	- 0.39
DATA	- 628	*	*	*	*

a departure from the previous data sets and may be understood by an examination of the dissipation enhancement parameterization in each model.

We may express (2-53) and (2-53a) in the following form

$$\frac{G_* - D_*}{\rho_o w_*^3} = e^{-h/Z} \quad \begin{cases} Z = 0 \text{ for KT} \\ Z = 50 \text{ m for EFT} \end{cases} \quad (4-5)$$

$$\frac{G_* - D_*}{\rho_o w_*^3} = 1.25 \frac{D_b h}{w_*^3} \quad (4-6)$$

Equations (4-5) and (4-6) represent the ratio of turbulent kinetic energy ($G_* - D_*$) available for mixing to the surface production according to the KT model ($\rho_o w_*^3$). The ratios in (4-5) and (4-6) are plotted in Fig. 4-10 as a function of various wind speeds and layer depths. They may be interpreted as the percentage of mechanical production of turbulent energy (relative to surface production of the KT model) available for entrainment in the various models. In the KT model dissipation enhancement is not parameterized and $G_* - D_*$ is always equal to $\rho_o w_*^3$. In the EFT model $G_* - D_*$ is equal to $\rho_o w_*^3$ only for the trivial case of $h \approx 0$. In general $G_* - D_* < \rho_o w_*^3$ according to (4-5) and therefore the KT model always predicts a deeper, cooler mixed layer than the EFT model. However, because the surface production in the KIM model was parameterized according to the Kato and Phillips (1969) experimental results, it is 25% larger than in the KT and EFT models. Dissipation enhancement is parameterized in the KIM model as a linear function of depth and a constant background

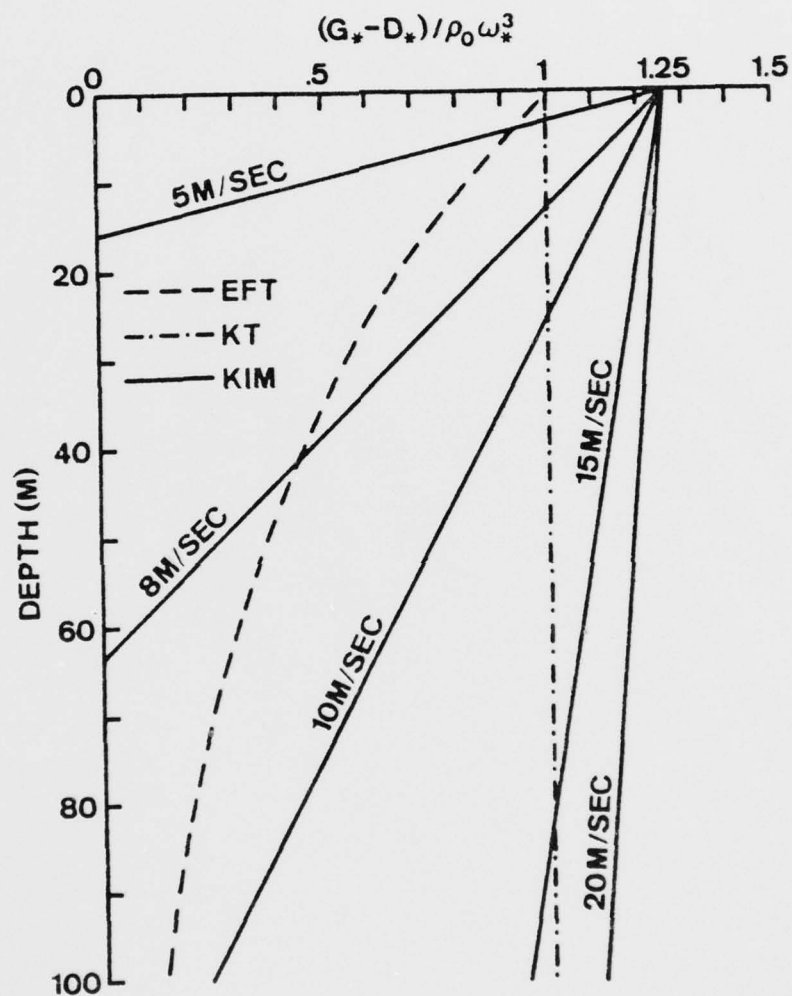


Figure 4-10. Values $G_* - D_*$ normalized by $\rho_0 \omega_*^3$ as a function of depth and wind speed for the EFT, KT, and KIM models.

dissipation (see Eq. 2-53a). In Fig. 4-10 it should be observed that there are combinations of wind speeds and mixed layer depth for which the amount of kinetic energy available for entrainment predicted by the KIM model may be greater or smaller than either the KT or EFT models.

During the events characterized by strong mechanical forcing, the response of the KIM model is very similar to the KT model and excessive mixed-layer depths are predicted. However, during periods of weak mechanical forcing, the mixed-layer depths predicted by the KIM model are too shallow and consequently the mixed-layer temperatures are too warm. These model results further suggest that the exponential parameterization of G_*-D_* , in the EFT model, may be calibrated for a wider range of wind speeds and layer depths than the linear parameterization in the KIM model.

E. IMPORTANCE OF NON-PENETRATIVE CONVECTION

In the previous three examples the percentage of convectively-generated turbulent kinetic energy available for entrainment was set equal to 15% ($r = 0.15$ in Eq. 2-50) following Gill and Turner (1976). In this section it will be demonstrated that non-penetrative convection (cooling of the mixed layer without deepening) should be an integral part of any turbulent bulk model. Furthermore, this property is absolutely essential during the fall and winter cooling seasons to prevent the models from predicting excessive deepening and cooling rates. Gill and Turner reported that the potential energy of the upper 250 m at nine ocean weather stations in the Atlantic reaches a maximum by early October and decreases during the October to March period. They were successful in simulating these potential energy changes with a

modified version of the KT model with $r = 0.15$. The experiments of Deardorff, et al. (1969) and Farmer (1975) suggest that r is of the order 0.01-0.15 but there were uncertainties in their estimates. However, the essential feature that must be simulated by the models is a decrease in the total potential energy during periods when the upward surface heat flux is larger than the entrainment heat flux.

The data set chosen to illustrate this point is from OWS V during the period 7-19 October 1963. It was selected because it is typical of the response of the upper ocean at OWS V during periods when the net surface heat flux is positive and larger than the entrainment heat flux (10 of the 13 data sets examined at OWS V are in this category). In this experiment, only the EFT model was used and the fraction of convectively-generated turbulent kinetic energy available for entrainment was varied between 15% and 100%.

Figures 4-11 to 4-13 depict the calculated forcing and the relative capability of the EFT model with varying amounts of non-penetrative convection. The atmospheric forcing (Fig. 4-11A) is characterized by a peak in the stress and surface cooling (Q_T) centered on 14 October. Compared with the forcing in the first example presented (Fig. 4-1A), the turbulent kinetic energy flux was nearly five times smaller, but the net surface heat flux was larger by 550 ly. In the next chapter it will be demonstrated that large upward heat fluxes are common at OWS V because of the extremely large air-sea temperature and vapor pressure differences during the fall and early winter seasons.

In Fig. 4-11B it should be observed that a significant mixed layer response occurred (42-60 m, 24.3-23.5°C). It should also be noted that the EFT model ($r = 0.15$) simulates this response with excellent agreement

BEST AVAILABLE COPY

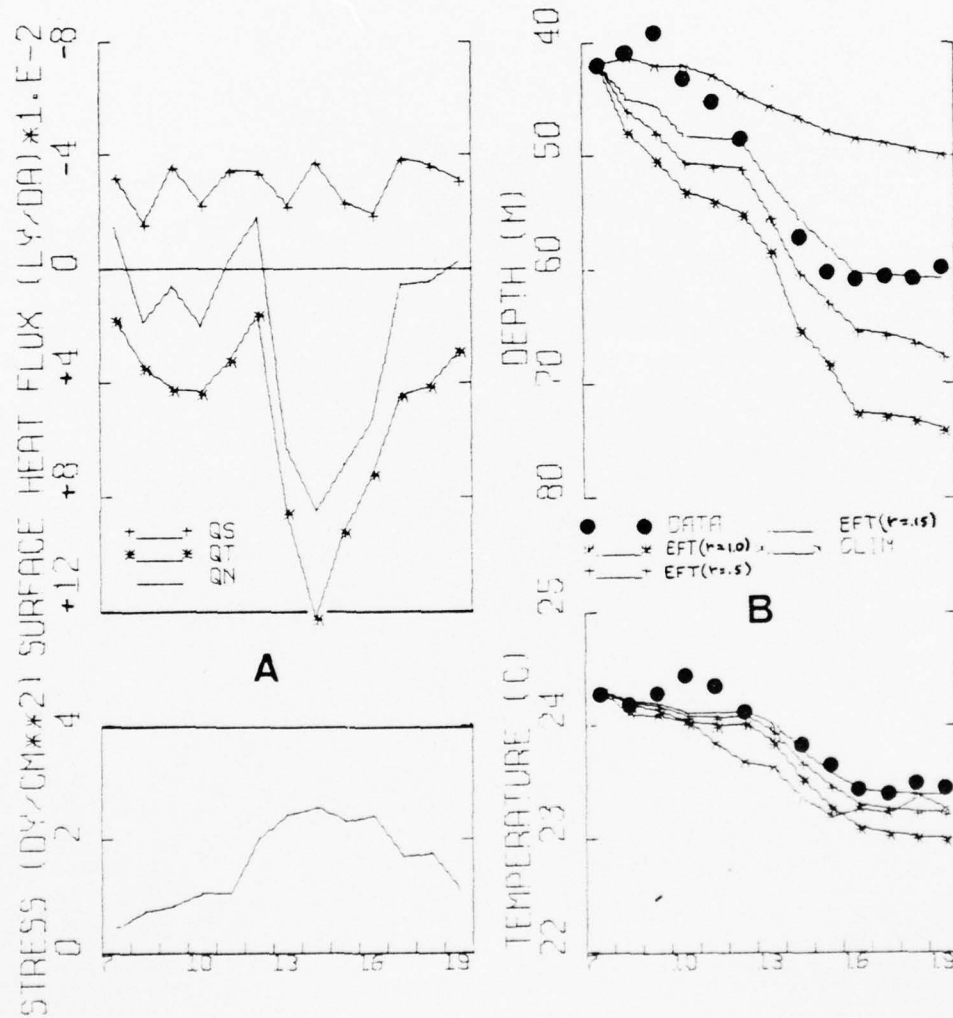


Figure 4-11. Same as Figure 4-1 except for OWS V during the period 7-19 October 1963.

BEST AVAILABLE COPY

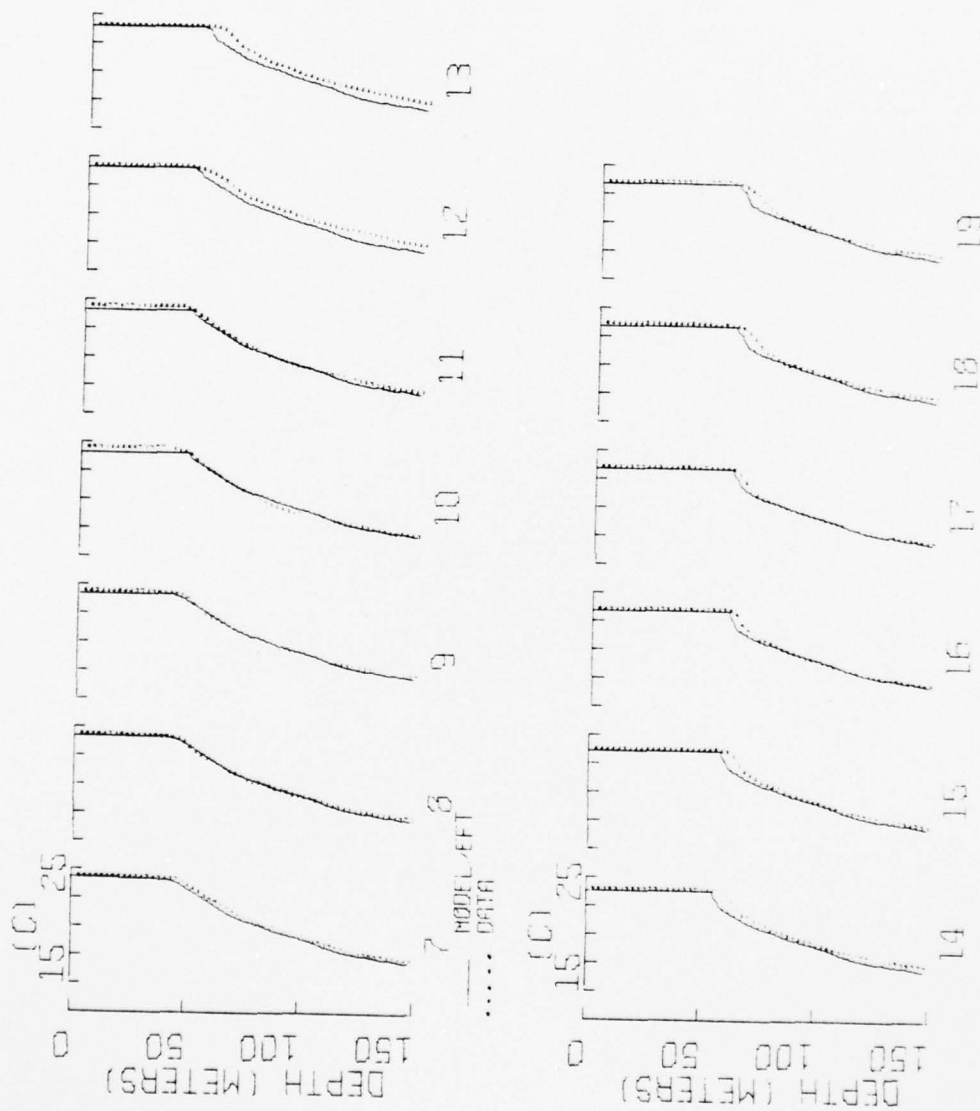


Figure 4-12. Same as Figure 4-2a except for OWS V during the period 7-19 October 1963.

BEST AVAILABLE COPY

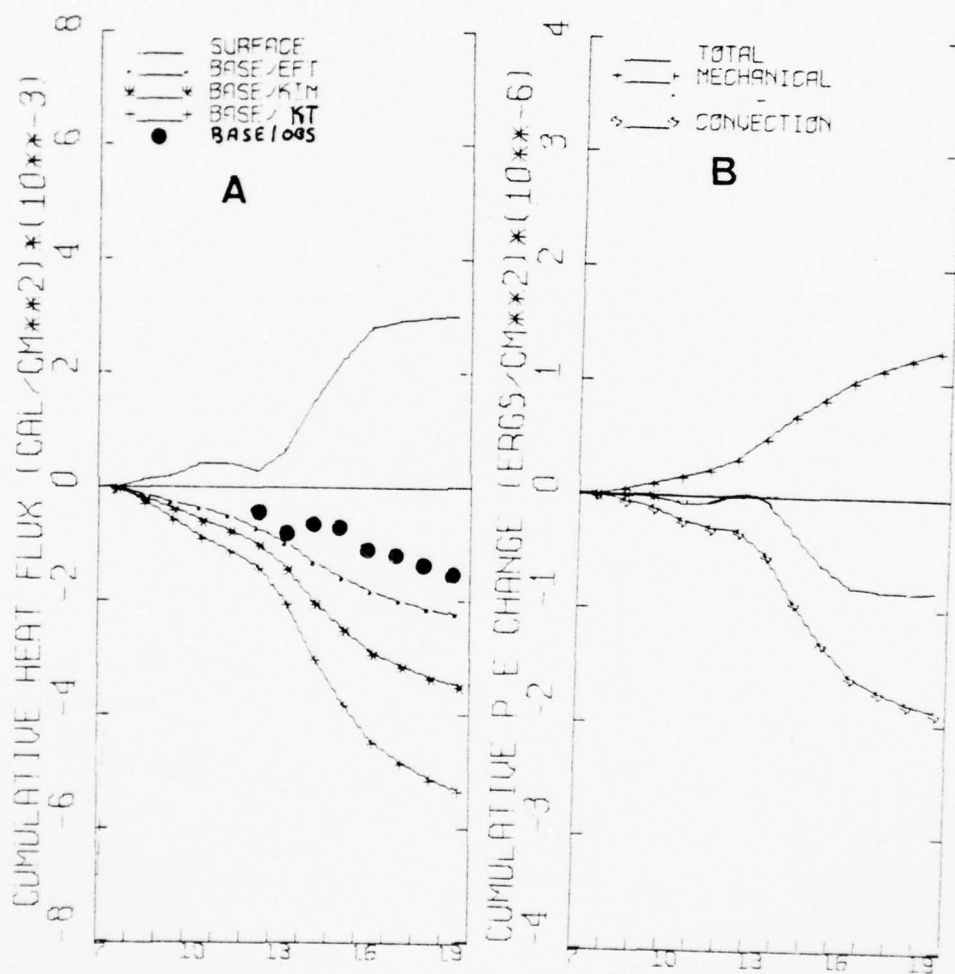


Figure 4-13. Same as Figure 4-3 except for OWS V during the period 7-19 October 1963.

with the data (42-61 m, 24.3-23.4°C). Note also in Fig. 4-12 the good agreement between the EFT model ($r = 0.15$) profiles and the data profiles. However, the EFT model with $r = 0.5$ (42-68 m, 24.3-23.2°C) and $r = 1.0$ (42-74 m, 24.3-23.0°C) predicted deepening and cooling rates that were too large.

In Fig. 4-13A and Table 4-4 it should be observed that the net surface heat flux (+3000) was larger than the entrainment heat flux estimated from the data (-1870). As previously mentioned, this should result in a total decrease in the potential energy and Fig. 4-13B and Table 4-4 show that the EFT model with $r = 0.15$ predicts this response. An examination of the potential energy modifications by the three variations of the EFT model (Table 4-4) illustrates the importance of properly parameterizing non-penetrative convection. It is important to observe that for $r = 0.15$ (15% of the convectively-generated turbulent kinetic energy available for entrainment) and $r = 0.5$ the total potential energy ($\Sigma \Delta PE$) is decreased in the model, while for $r = 1.0$ it is increased. In fact, as discussed in Chapter II (see 2-51), a model with full penetrative convection ($r = 1.0$) must increase the potential energy. In accordance with the findings of Gill and Turner (1976) a model with $r = 1.0$ will not be useful for seasonal integrations. The present results from the EFT model with $r = 1.0$ indicates that, in certain circumstances, it will also be wrong for very short integrations during the cooling season. The results from the EFT model with $r = 0.15$ suggest this model (with an exponential dissipation parameterization) reasonably simulates this process.

An additional reason for presenting this data set is because its time frame (7-19 October) is the same as the first example (Fig. 4-1)

TABLE 4-4. Model and data comparison at OWS V for the period 7-19 October 1963.
(Asterisks indicate quantities that could not be computed.)

MODEL	ΣQ_n (Langley)	$\Sigma W^*T^*(-h)$ (Langley)	$\Sigma \Delta PE (x 10^{-6})$ (ergs-cm ⁻²)	$\Sigma \Delta PE_m (x 10^{-6})$ (ergs-cm ⁻²)	$\Sigma \Delta PE_c (x 10^{-6})$ (ergs-cm ⁻²)
EFT r=.15	+3000	- 2,236	- 0.93	+1.28	- 1.92
EFT r=.5	+3000	- 3,474	- 0.29	+0.91	- 2.40
EFT r=1.0	+3000	- 5,318	+ 0.85	+0.85	- 2.62
DATA	+3000	- 1,870	*	*	*

from OWS P. Since these two examples are typical of the atmospheric forcing events and associated oceanic response at these two stations, they may be compared to illustrate the essential differences in the physical mechanisms that modify the upper ocean at these two stations. Comparing $\Sigma \Delta PE_m$ (for EFT, $r = 0.15$) in Tables 4-1 and 4-4 it is observed that nearly four times as much turbulent kinetic energy was available for entrainment at OWS P as at OWS V. It should be further noted that the deepening rates ($\frac{\partial h}{\partial t}$) were comparable but resulted in a significantly larger decrease in the mixed-layer temperature at OWS P (compare $\frac{\partial h}{\partial t}$ and $\frac{\partial T_s}{\partial t}$ in Figs. 4-1B and 4-11B). Considering the ratio defined by (4-1) $h\Delta b$ must be significantly larger at OWS P. Since the mixed layer is deeper at OWS V during these data sets the below layer gradient (represented in the model as ΔT) at OWS P must account for $h\Delta b$ being larger at OWS P. It may be observed in Figs. 4-2A and 4-12 that the below layer gradient at OWS P is typically much larger than at OWS V. Therefore significantly more work is required to deepen the layer at OWS P. However, for comparable deepening rates as in these two cases, the resulting entrainment heat flux will be much larger at OWS P than at OWS V (compare $\Sigma \overline{w'TT'}(-h)$ in Tables 4-1 and 4-4 during these two cases). The larger entrainment flux at OWS P is the principal reason for the larger sea-surface temperature change, since the net surface heat fluxes (ΣQ_n) are very similar during these two cases. Since these two examples are typical of the response of the mixed layer at these two stations during the fall and winter storm events it is suggested that the entrainment heat flux plays the most dominate role at OWS P. While the entrainment heat flux at OWS V is less important, it is still an essential part of the local heat budget of the mixed layer, and can not be ignored.

In this and the previous section the data sets examined illustrated the different upper ocean responses that occur under various atmospheric forcing and initial oceanic conditions. It should be noted that large upper ocean thermal responses may take place when either the mechanical forcing or upward turbulent heat fluxes are large. It is also important to note once again that both the surface heat flux and the entrainment heat flux must be specified in order to predict the sea-surface temperature. It should also be noted that during these large storm events, the response of the ocean is primarily one-dimensional because the vertical heat fluxes are extremely large during relative short periods. To adequately simulate these large one-dimensional responses it has been demonstrated that an adequate parameterization of dissipation enhancement and non-penetrative convection is absolutely essential. A combination of $r = 0.15$ (after Gill and Turner, 1976) and the EFT model parameterization of dissipation enhancement consistently were in better agreement with the data than the KT or KIM models.

F. IMPORTANCE OF NON LOCAL EFFECTS

In this section the performance of the three models will be examined during a period when the local heat balance was not maintained. The purpose of this presentation is to demonstrate that the one-dimensional model is capable of providing useful temperature structure information during periods characterized by large horizontal heat fluxes. The data set chosen to illustrate these points is from OWS N during the period 9-24 November 1965. Figures 4-14 to 4-16 again depict the nature of the forcing, the observed mixed layer response, and the relative performance of the models. The data set is characterized by two distinct events centered on November 15 and 22 (see Fig. 4-14A) and the turbulent kinetic

BEST AVAILABLE COPY

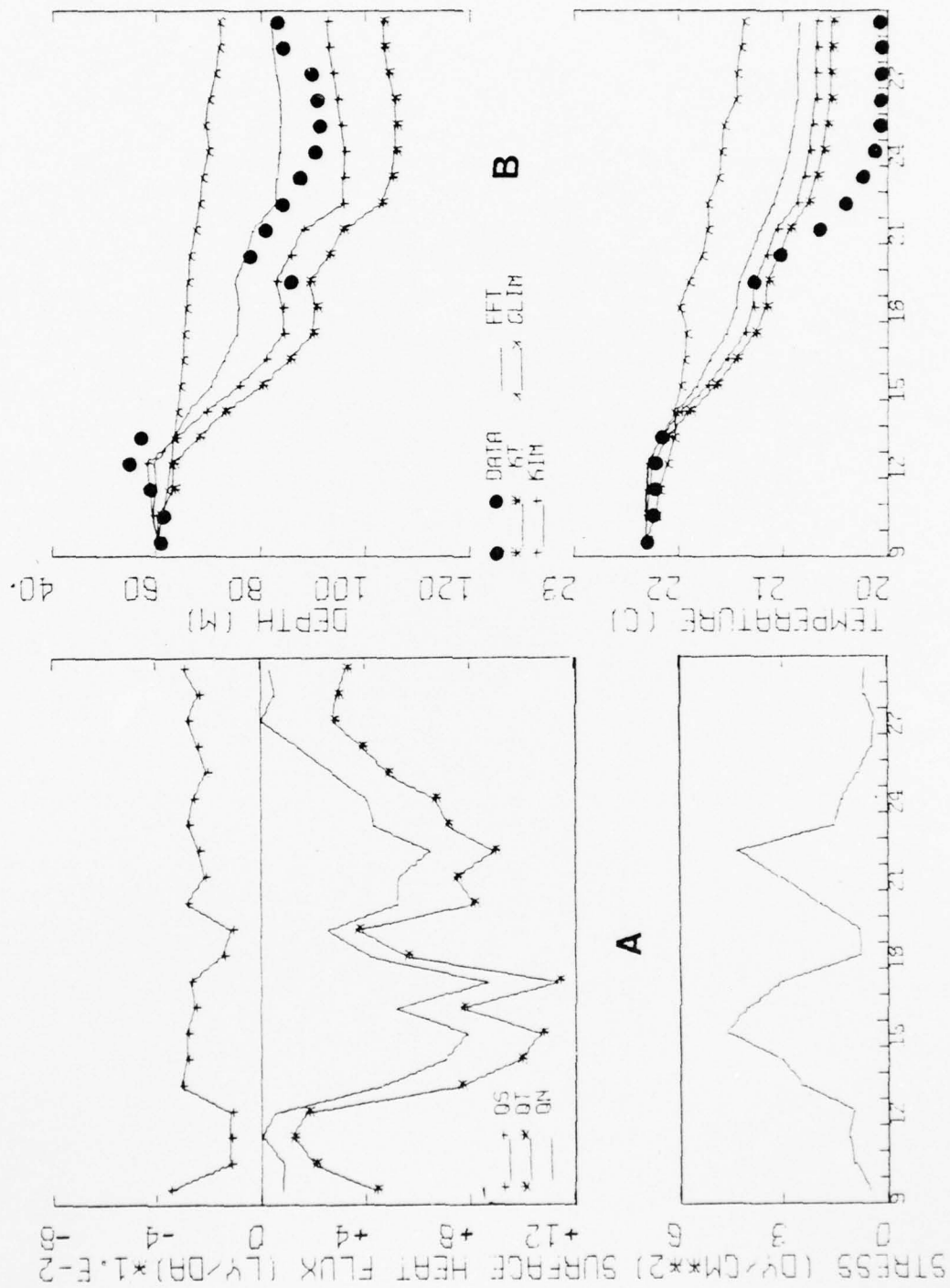


Figure 4-14. Same as Figure 4-1 except for OWS N during the period 9-29 November 1965.

BEST AVAILABLE COPY

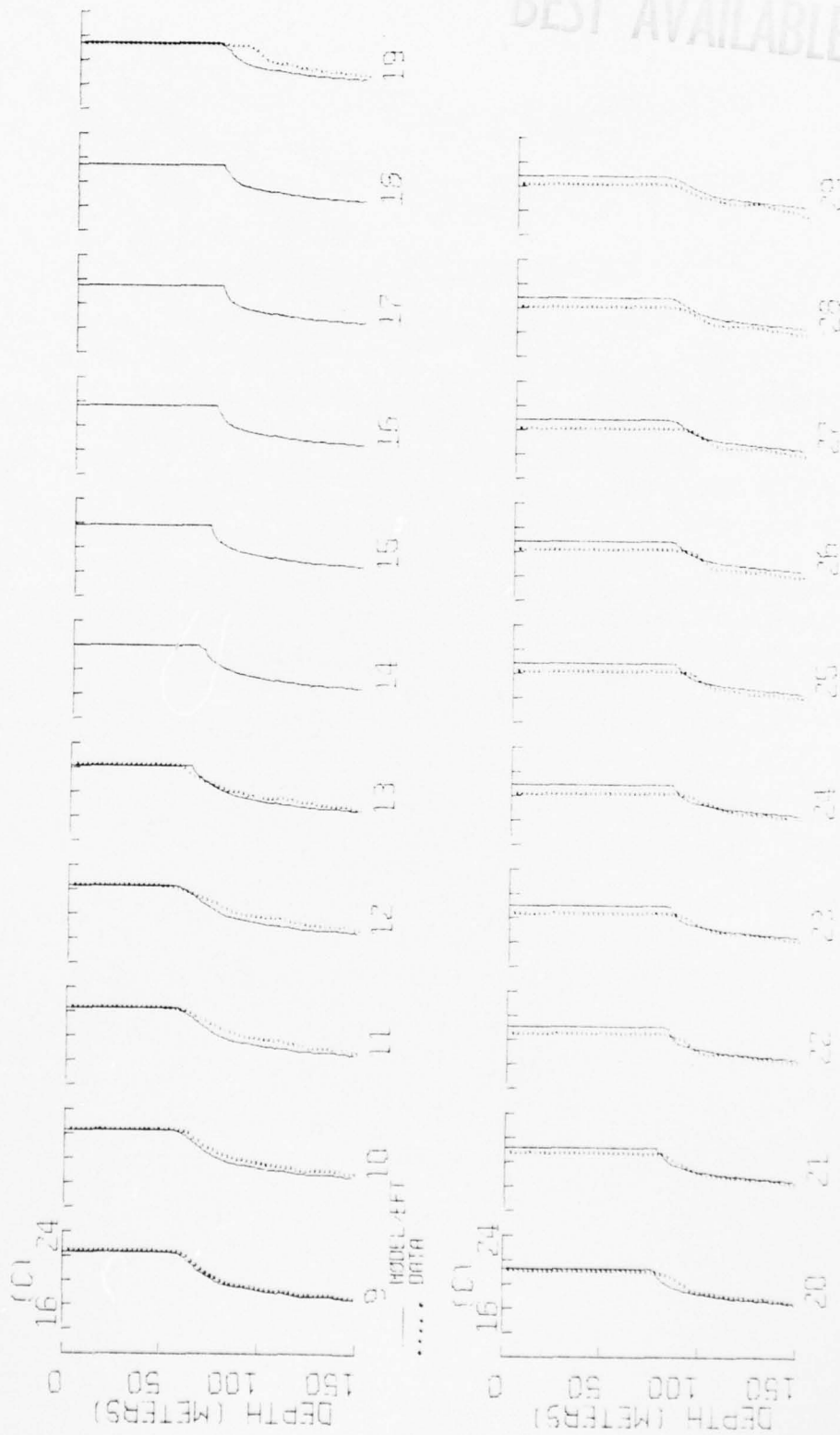


Figure 4-15. Same as Figure 4-2a except for OWS N during the period 9-29 November 1965.

BEST AVAILABLE COPY

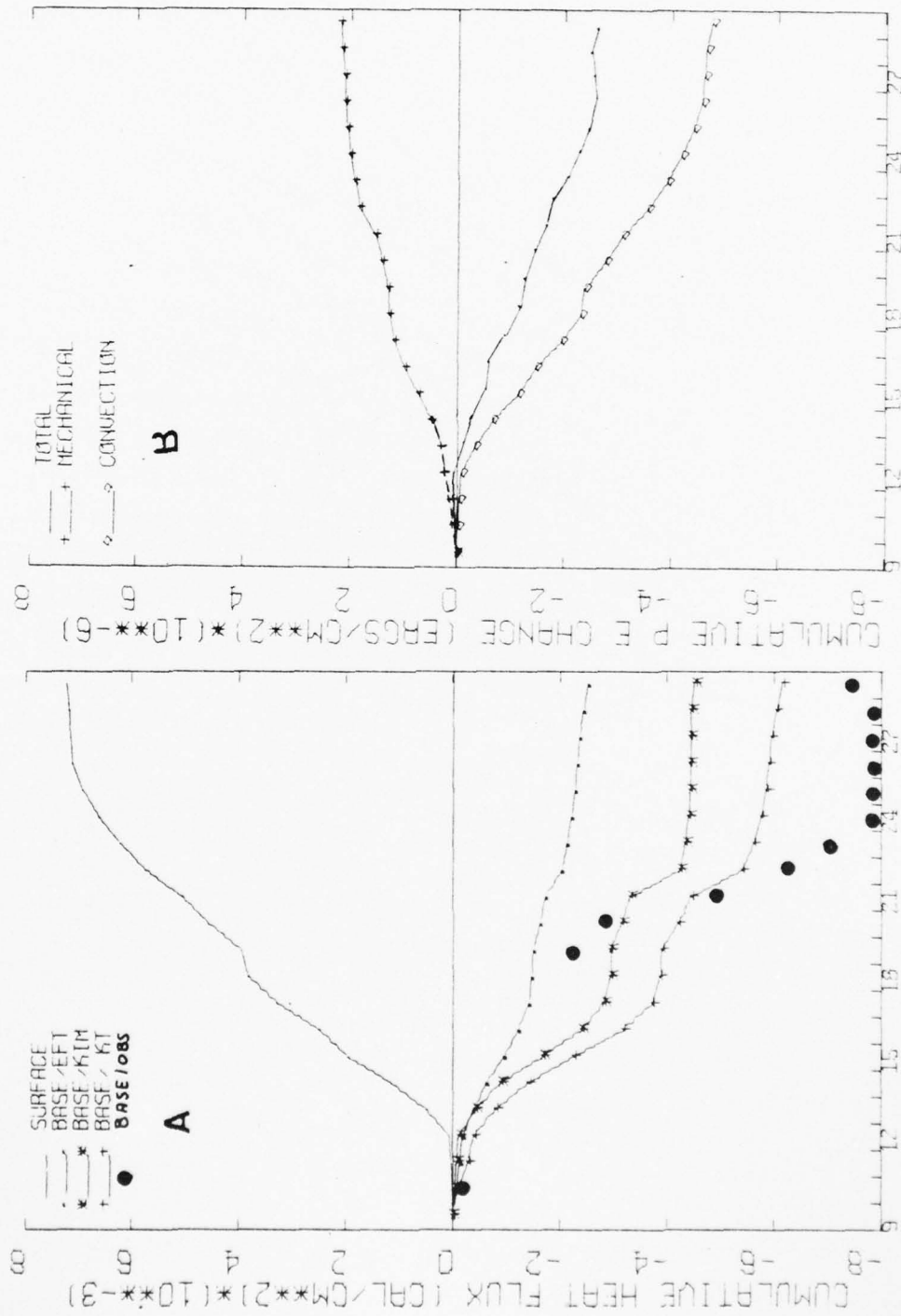


Figure 4-16. Same as Figure 4-3 except for OWS N during the period 9-29 November 1965.

energy and net surface flux exchanged during these events were very strong compared with climatology (total u_*^3 for November 1965 was 205% of the climatological mean for November and total Q_n was 160% of the mean). During the period 9-29 November 1965, 95% of the total monthly turbulent kinetic energy and 80% of the net surface heat flux were exchanged.

It should be observed in Fig. 4-14B and 4-15 that the EFT model accurately simulates the evolution of the mixed layer through November 19 and suggests that the local heat balance was maintained during this period. The estimate of cumulative entrainment heat flux from the data (Fig. 4-15A) on November 19 also supports this suggestion. However after November 19-20 the observed mixed-layer temperature decreased significantly, relative to all the models, while the mixed-layer depth was simulated quite well by the EFT model. Furthermore, in Fig. 4-16A it may be observed that the entrainment heat flux, estimated from the data from November 19-29, appears to be too large. The layer depth, according to the data, only increased 8 m during the period November 19-29. This small $\frac{\partial h}{\partial t}$ coupled with the weak temperature gradient immediately below the mixed layer (Fig. 4-15), would not support BASE/OBS (Fig. 4-15A) during this period.

The reason for the difference between the observed and model mixed layer temperature during November 20-29 is presumed to be due to a horizontal intrusion of a cold water mass into the region. This presumption is based upon the observations from Fig. 4-15 that the entire data profile (even below the mixed layer) is colder relative to the EFT model. During this period the ocean weather ship reported its position to within 10 NM of 30N - 140W and therefore ship drift was not responsible for the temperature changes. Since the temperature changes observed in Fig. 4-15

AD-A039 346

NAVAL POSTGRADUATE SCHOOL MONTEREY CALIF
THE ROLE OF STRONG ATMOSPHERIC FORCING EVENTS IN THE MODIFICATI--ETC(U)
DEC 76 N T CAMP

F/G 8/3

UNCLASSIFIED

NL

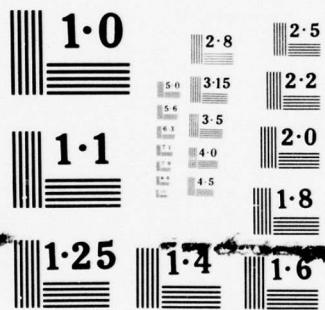
2 OF 2
ADA
039346



END

DATE
FILMED

5-77



NATIONAL BUREAU OF STANDARDS
MICROCOPY RESOLUTION TEST CHART

can not be due to vertical mixing, it is suggestive of a horizontal heat flux.

During this period the EFT model was able to simulate the mixed-layer depth quite well and the characteristic slope of the temperature profile was maintained. If the principal motivation for this forecast was to predict the thermal structure modifications, say for predicting the resulting changes in the acoustic properties, then the EFT model results would be very useful. These model results further suggest that if the horizontal heat fluxes were specified, say from an ocean general circulation model, then the EFT model would be capable of predicting the total response of the upper ocean with adequate accuracy.

G. RELATIVE PERFORMANCE OF THE EFT, KT, AND KIM
MODELS AT OWS P, OWS N, AND OWS V

In this section the relative performance of the EFT, KT, and KIM models will be evaluated at the three ocean weather stations. Figures 4-17 to 4-19 depict the daily observed mixed-layer depths versus the predicted depths for the three models at the three ocean weather stations. The diagonal lines are drawn to aid in relating model results to the locus of perfect prediction. In Table 4-5 the RMS and mean errors for the mixed-layer temperature (MLT) and mixed-layer depth (MLD) are presented for the three models at the three stations. A negative mean error in MLD indicates that the model, on the average, predicted a deeper MLD. A negative MLT indicates that, on the average, the model predicted MLT was warmer than the observations. The RMS and mean errors are based on the daily (morning) observed and predicted MLT and MLD and are based on 313 values at OWS P, 238 at OWS N, and 208 at OWS V (this includes all 49 cases studied).

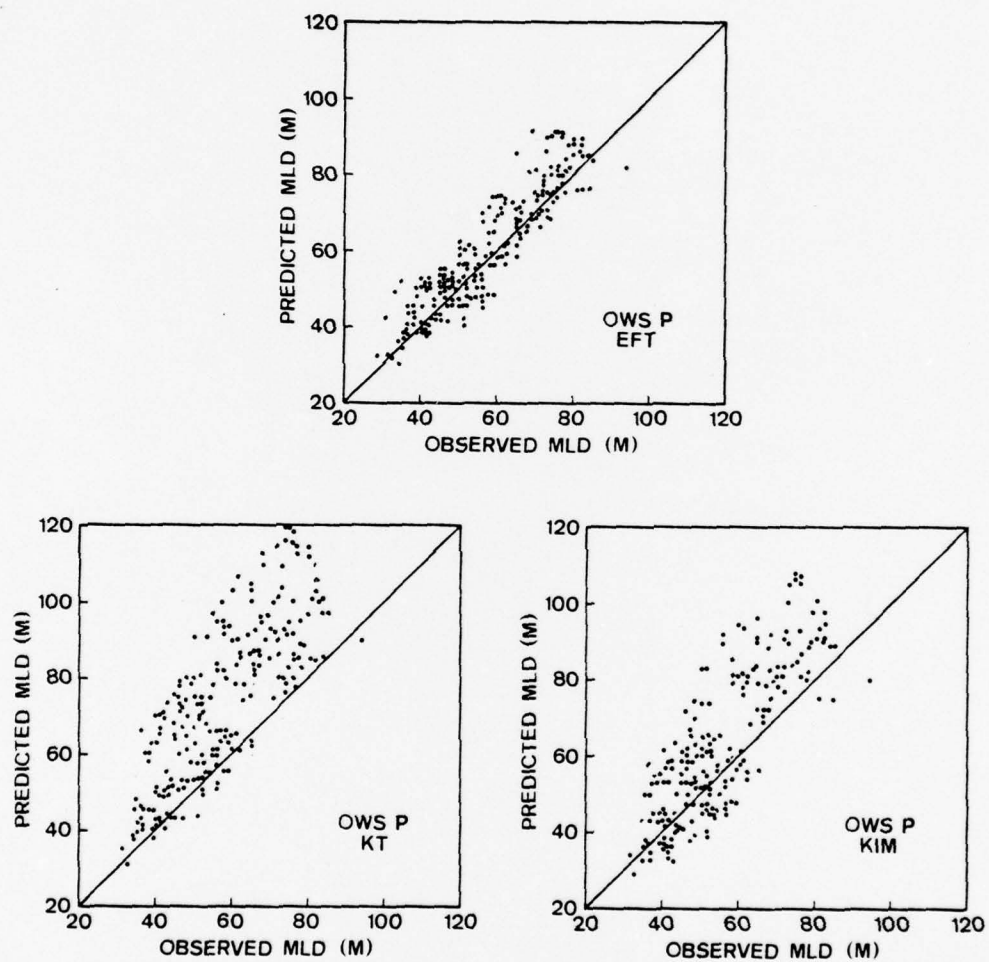


Figure 4-17. Predicted vs. observed mixed layer depths (MLD) at OWS P.

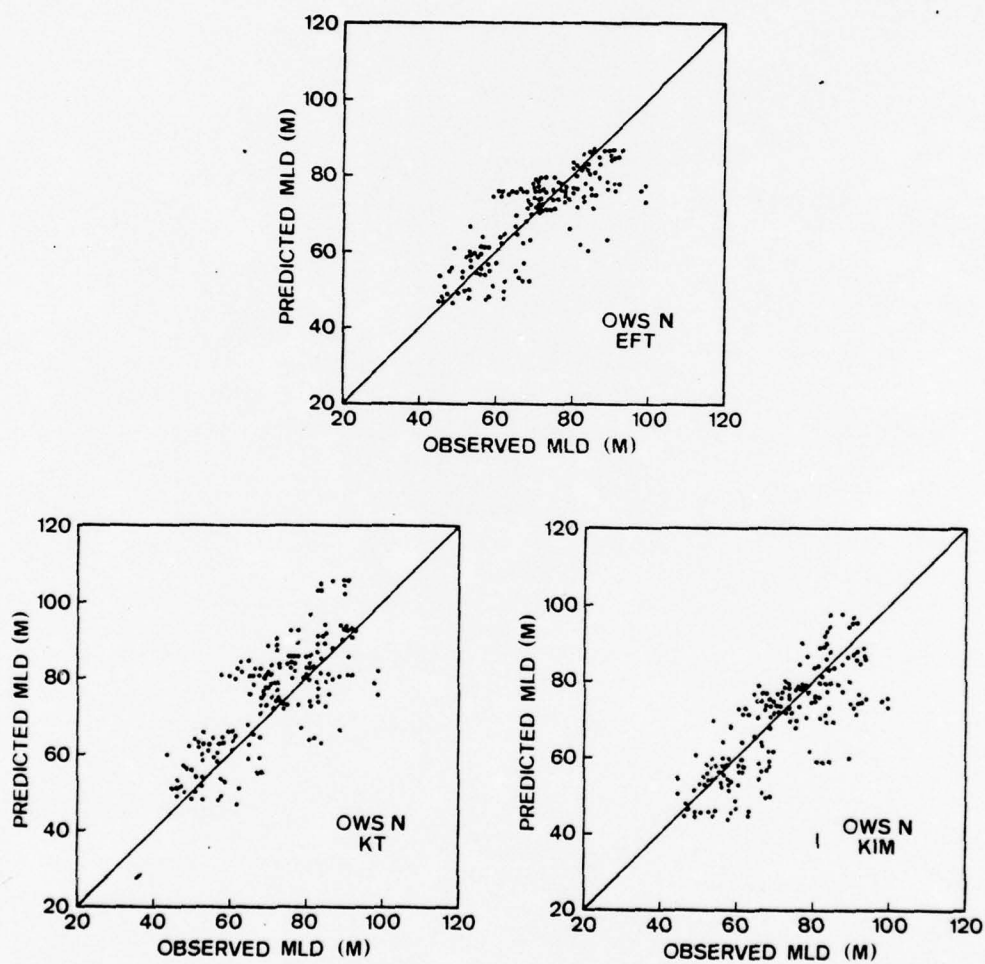


Figure 4-18. Same as 4-17 except for OWS N.

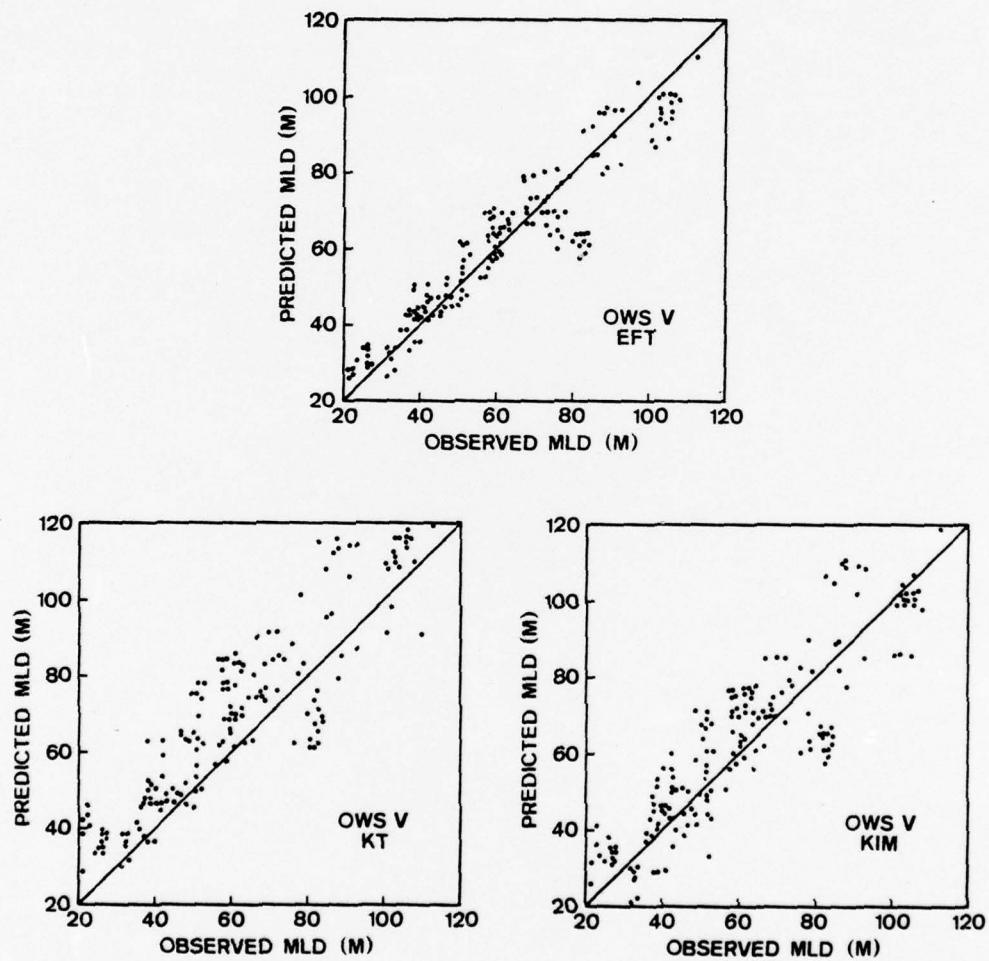


Figure 4-19. Same as 4-17 except for OWS V.

TABLE 4-5. Comparison of mean and RMS errors of the models at the three ocean weather stations.

OWS P				
Model	MLT RMS (°C)	MLT Mean Error (°C)	MLD RMS (m)	MLD Mean Error (m)
EFT	0.36	+0.16	6.8	-2.9
KIM	0.49	+0.32	13.8	-7.6
KT	0.72	+0.54	19.9	-15.6

OWS N				
Model	MLT RMS (°C)	MLT Mean Error (°C)	MLD RMS (m)	MLD Mean Error (m)
EFT	0.34	-0.01	6.7	+1.6
KIM	0.35	-0.02	8.9	+2.2
KT	0.37	+0.04	10.0	-2.8

OWS V				
Model	MLT RMS (°C)	MLT Mean Error (°C)	MLD RMS (m)	MLD MEAN Error (m)
EFT	0.65	+0.02	9.8	-1.3
KIM	0.66	+0.05	11.2	-4.2
KT	0.75	+0.18	14.1	-9.1

* RMS and MEAN ERROR based on comparison of daily observed and predicted mixed-layer depth (MLD) and mixed-layer temperature (MLT). Statistics are computed from 313 comparisons at OWS P, 238 at OWS N and 208 at OWS V.

It should be observed in Table 4-5 that the RMS and mean errors for MLT and MLD are consistently smallest for the EFT model and largest for the KT model. At OWS P, for example, the scatter observed in Fig. 4-17 and the mean MLT and MLD errors in Table 4-5 show that the models are all biased toward predicting a mixed layer that is too cool and too deep. However the RMS and mean errors, and the magnitude of the scatter in Fig. 4-17, demonstrate clearly that the EFT model simulates MLT and MLD more accurately at OWS P. During the fall and early winter, OWS P is characterized by the largest mechanical forcing observed at the three stations (see Fig. 3-1C). The performances of the EFT model relative to the KT and KIM models suggest that the exponential parameterization of dissipation enhancement (EFT) was most effective in preventing excessive deepening.

At OWS N the mean errors in MLT and MLD, observed in Table 4-5, and the scatter in Fig. 4-18 indicate that the EFT and KT predict MLT and MLD, on the average, too warm and too shallow. The KT model is again biased toward predicting MLT and MLD too deep and too cool. At OWS N considerably less mechanical energy is transferred to the ocean than at OWS P (again see Fig. 3-1C). Therefore, at OWS N, one would expect convection to play a more dominate role in the mixed-layer evolution and the performance of the three models to be more similar. The similarity in the scatter in Fig. 4-18 and the RMS and mean errors in Table 4-5 should be observed to be very similar at OWS N. An interesting observation may be made by comparing the relative magnitude of the RMS and mean errors at OWS P and OWS N. At OWS P the relationships between the mean and RMS MLT and MLD errors suggest that the increasing RMS errors are largely due to the increasing bias of the EFT, KT, and KIM models. At

OWS N, however, the large RMS errors, relative to the mean errors (most obvious in MLT), would suggest that the errors are more random at OWS N than at OWS P.

At OWS V the scatter observed in Fig. 4-19 and the RMS and mean errors in Table 4-5 indicate that the models are all biased toward predicting MLD and MLT too deep and too cool. Again it should be observed that the scatter in Fig. 4-19 and the RMS and mean error for MLD are smallest for the EFT model and largest for the KT model. As indicated previously, mechanical energy and convection are strong at OWS V. The increasing RMS and mean MLD errors for the EFT, KT, and KIM may once again be related to the parameterization of dissipation enhancement in each model. Again it should be observed that the relationship between the RMS and mean errors in MLT would suggest that a considerable amount of the RMS MLT error is random.

The data presented in Figs. 4-17 to 4-19 and Table 4-5 clearly indicate that the EFT model is capable of predicting a larger percentage of the observed MLT and MLD changes observed in the data sets modeled in this study. The exponential parameterization of dissipation enhancement coupled with an adequate estimate of non-penetrative convection appears to be most reasonable for predicting the changes associated with large atmospheric forcing events.

Table 4-6 presents a comparison of the accuracy with which the EFT model predicted the total observed MLT change during the 49 data sets examined in this study. The values in Table 4-6 represent the number of data sets during which the EFT model predicted the various percentages of the total observed MLT change. For example, at OWS P, in 7 out of the 20 data sets, greater than 90% of the observed MLT change was predicted by the EFT model. It may be observed in Table 4-6 that the EFT

TABLE 4-6. Comparison of MLT predictions by the EFT model at the ocean weather stations.

OWS	Percentage of MLT Change Predicted				Number of Data Sets
	>90%	>75%	>50%	>25%	
P	7*	12	18	18	20
N	2	7	12	14	16
V	6	7	10	11	13

*Values in the table are the number of data sets which predict the prescribed percentage of MLT.

model showed reasonably good capability in predicting the MLT. For example, in nearly 50% of the data sets modeled, the EFT model was capable of predicting greater than 75% of the observed MLT changes. Additionally in 18 out of 20 cases at OWS P, 12 out of 16 at OWS N, and 10 out of 13 at OWS V the one-dimensional model accounted for greater than 50% of the observed MLT change. It should be noted that in this study only a minimum of calibration was performed with the EFT model. The performance of the model was still quite good and suggests that greater reliability could be obtained with more extensive calibration.

In addition to providing reasonable estimates of MLT and MLD changes, the one-dimensional model provides a means of separating the contributions of the vertical heat fluxes to the total heat budget of the mixed layer. As may be seen in Fig. 4-16A (BASE/OBS), the estimation of the entrainment heat flux from the data is very unreliable during periods when non-local processes are important. In the next section we will examine ΣQ_n and $\Sigma \overline{w'T'}(-h)$ from the EFT model results in an attempt to determine the relative importance of these heat fluxes at the three weather stations.

H. RELATIVE IMPORTANCE OF THE SURFACE AND ENTRAINMENT HEAT FLUXES

In this section an attempt will be made to determine the relative importance of the surface and entrainment heat fluxes during the periods modeled in this study. In the first four examples presented in this chapter, it was demonstrated that during periods when the local heat budget was maintained, the EFT model predicted the mixed layer depth and temperature quite accurately. Furthermore estimates of the entrainment heat flux from the data were in good agreement with model calculations.

Since the thermal structure modifications calculated by the model agreed closely with the data, it is assumed the potential energy changes calculated in the model are representative of the potential energy changes occurring in the ocean. Additionally it will be assumed that during periods when non-local processes are important the vertical turbulent heat fluxes are still represented accurately by the EFT model.

Figure 4-20A depicts the relative magnitudes of the total cumulative net surface and entrainment heat fluxes calculated by the EFT model. In Fig. 4-20B the total potential energy change ($\Sigma \Delta PE$) is plotted against the total upper ocean heat content change (ΣQ_n) calculated by the EFT model. Since the model is one-dimensional $\Delta H \approx \Sigma Q_n$. The data in Figs. 4-20A,B is representative of the total changes calculated by the model in all but three data sets at the ocean weather stations. One data set at OWS P, presented earlier in this chapter, and two at OWS V were examples of weak surface heating periods and the entrainment heat flux totally dominated the heat budget of the mixed layer.

These two figures may be interpreted in light of the four one-dimensional data sets previously presented. If $\Sigma \Delta PE > 0$ (Fig. 4-20B) during these periods, then the mechanical mixing by the wind was the dominant vertical turbulent process, and normally this will be indicated in Fig. 4-20A by $|\Sigma \overline{w'T'}(-h)| > |\Sigma Q_n|$. If, however, $\Sigma \Delta PE < 0$ then convection was the dominant vertical turbulent process and $|\Sigma \overline{w'T'}(-h)| < |\Sigma Q_n|$. The relationships depicted in Figs. 4-20 indicate that the atmospheric forcing events examined at OWS P were mainly dominated by mechanical mixing. In 15 of the 19 cases examined, $|\Sigma \overline{w'T'}(-h)| > |\Sigma Q_n|$ and $\Sigma \Delta PE \geq 0$. At OWS N and OWS V, however, the large majority of the atmospheric forcing events were dominated by convection. In 12 of the

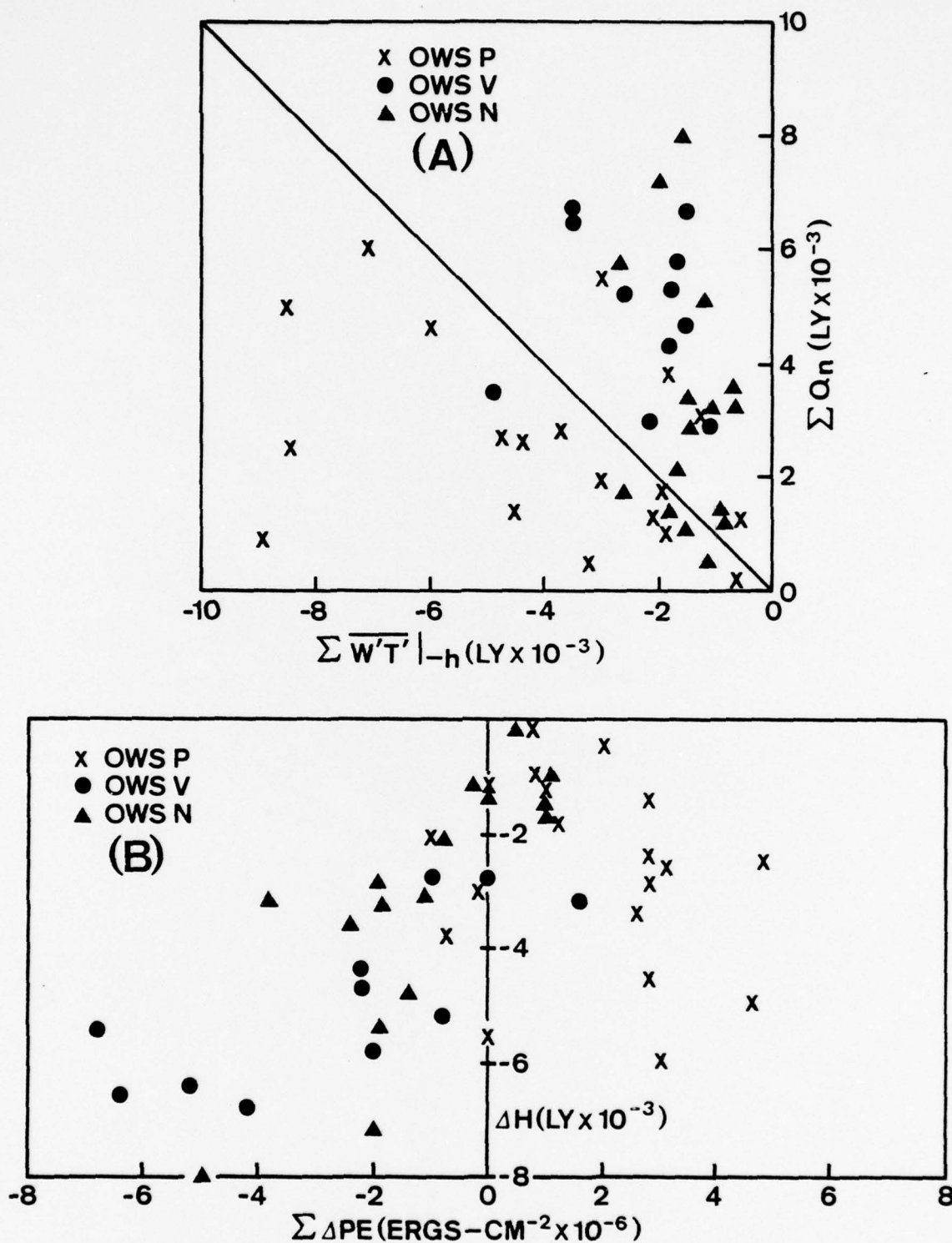


Figure 4-20. Relative magnitude of the cumulative heat fluxes and total potential energy change at the three ocean stations. (A) Cumulative net surface heat flux (ΣQ_n) vs. cumulative entrainment heat flux ($\Sigma \overline{w'T'}|_{-h}$) (B) Total potential energy change ($\Sigma \Delta PE$) vs. ocean heat content change (ΔH). All points calculated by EFT model for total duration of data set.

16 data sets at OWS N $|\Sigma \overline{w'T'}(-h)| < |\Sigma Q_n|$ and $\Sigma \Delta PE \leq 0$, and at OWS V 10 of 11 cases indicated $|\Sigma \overline{w'T'}(-h)| < |\Sigma Q_n|$ and $\Sigma \Delta PE \leq 0$.

It has been demonstrated that the large forcing events, whether dominated by mechanical forcing or surface cooling, are capable of causing extremely large changes in the mixed layer in relatively short periods. It has further been illustrated that the response during these large events is largely one-dimensional. Additionally, it has been shown that a one-dimensional model, properly parameterized to include dissipation enhancement and non-penetrative convection, is capable of predicting a large percentage of the observed changes. In the next chapter we will attempt to determine how significant is the role of the large forcing events in the total seasonal evolution of the upper ocean.

V. ROLE OF STRONG ATMOSPHERIC FORCING
EVENTS IN THE SEASONAL EVOLUTION OF
THE UPPER OCEAN

A. INTRODUCTION

In the previous chapter it was demonstrated that significant changes may take place in the upper ocean thermal structure in response to strong atmospheric forcing events. Further it was shown that the one-dimensional processes, when modeled properly, are capable of predicting a large percentage of these observed changes in the three locations studied. In this chapter the historical series of surface and near-surface marine observations will be examined in a new and rather unique way, and the principal objectives will be to:

1. determine the significant characteristics of the atmospheric forcing during the fall and early winter cooling season at the three ocean weather stations;
2. demonstrate that the major features of the upper ocean thermal response during the cooling season are explainable in terms of one-dimensional processes;
3. quantify the relative importance of strong atmospheric forcing events to the total evolution of the upper ocean at OWS P, OWS N, and OWS V.

B. CHARACTERISTICS OF THE MARINE ATMOSPHERE
AT THE OCEAN WEATHER STATIONS

To determine the distribution and variability of the atmospheric forcing at the three ocean weather stations, values representative of wind speed (u_*), turbulent kinetic energy flux (u_*^3), and upward turbulent heat flux (Q_a) were computed from every available three-hourly record. These values were grouped into equal (32) class intervals (ranked in order of increasing values) and the resulting frequency distributions are

depicted in Figs. 5-1 and 5-2. Additionally Table 5-1 lists the significant statistical quantities which characterize these distributions. In all future discussions a negative heat flux will represent a heat loss by the ocean.

The non-gaussian nature of these distributions is evidenced by their characteristic shape and the values of skewness and kurtosis presented in Table 5-1. It will be demonstrated that the large, relatively rare values (reflected by the long tails in the distributions) account for a considerable amount of the total energy exchange. The means of the u_* and u_*^3 distributions show that the strongest winds and largest turbulent kinetic energy exchanges occur at OWS P while the weakest mechanical interactions are observed at OWS N. From the distribution of Q_a it is observed that the largest turbulent heat fluxes take place at OWS V and the smallest at OWS P. Additionally, Table 5-1 shows that the mean of the u_* distribution, at all stations, is approximately double its standard deviation. This relationship is also valid for Q_a at OWS N, while at OWS P and OWS V the distribution of Q_a has more relative variance than u_* . This implies that the variability of the turbulent heat fluxes is more closely coupled to the variability of the wind at OWS N than at the other stations. It will be demonstrated that the increased variance in Q_a at OWS P and OWS V is the result of a larger variability in the air-sea temperature and vapor pressure differences at these stations. These distributions indicate that the characteristics of the marine atmospheric forcing are similar at OWS P and OWS V but quite different at OWS N. The similarities and differences in these characteristics may be explained by considering the principal air-sea parameters in terms of the geographical locations of the three ocean weather stations.

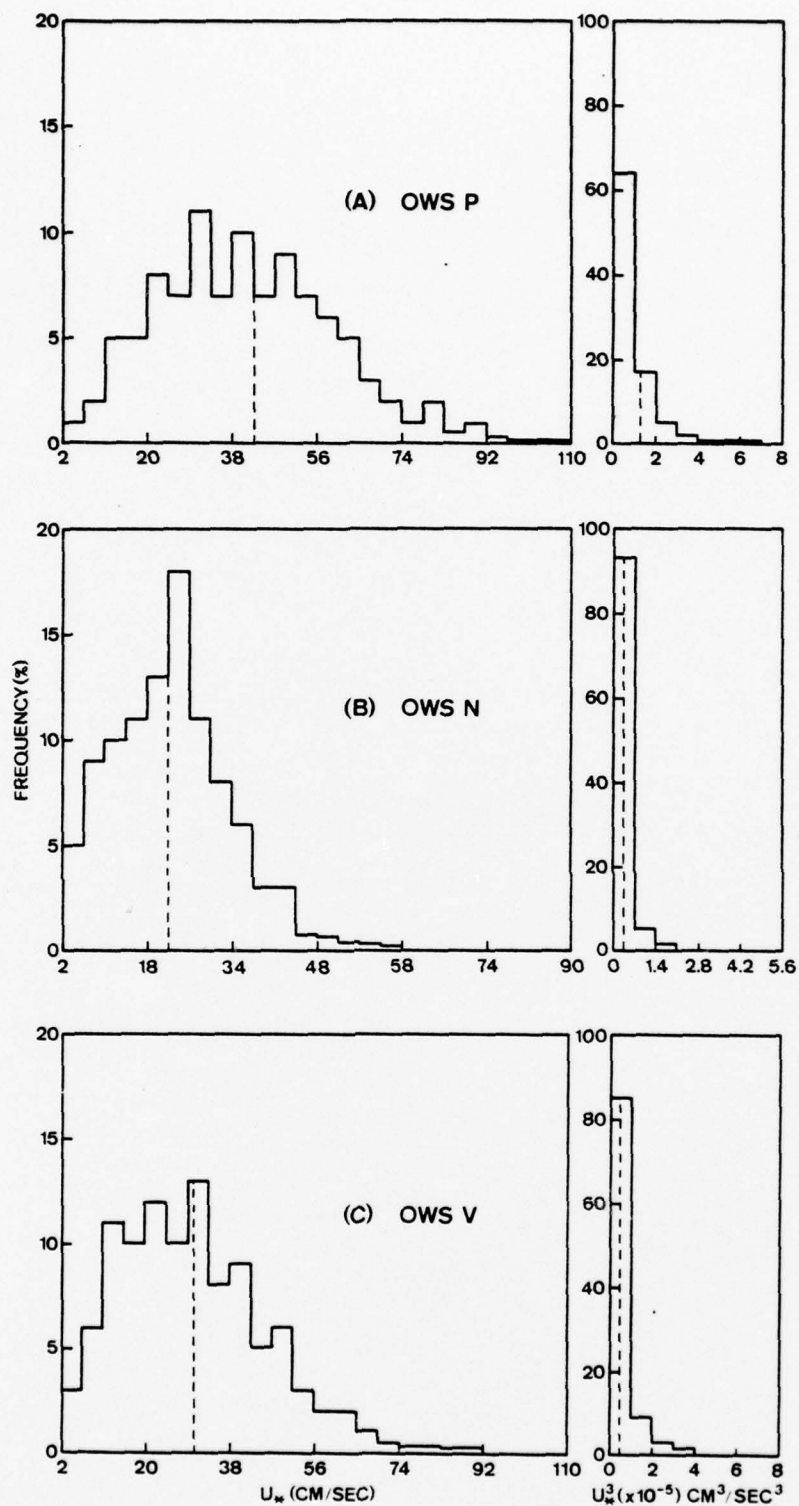


Figure 5-1. Histograms of wind speed (u_*) and turbulent kinetic energy flux (u_*^3) at OWS P, OWS N, and OWS V. Vertical dashed lines represent the mean of the distribution.

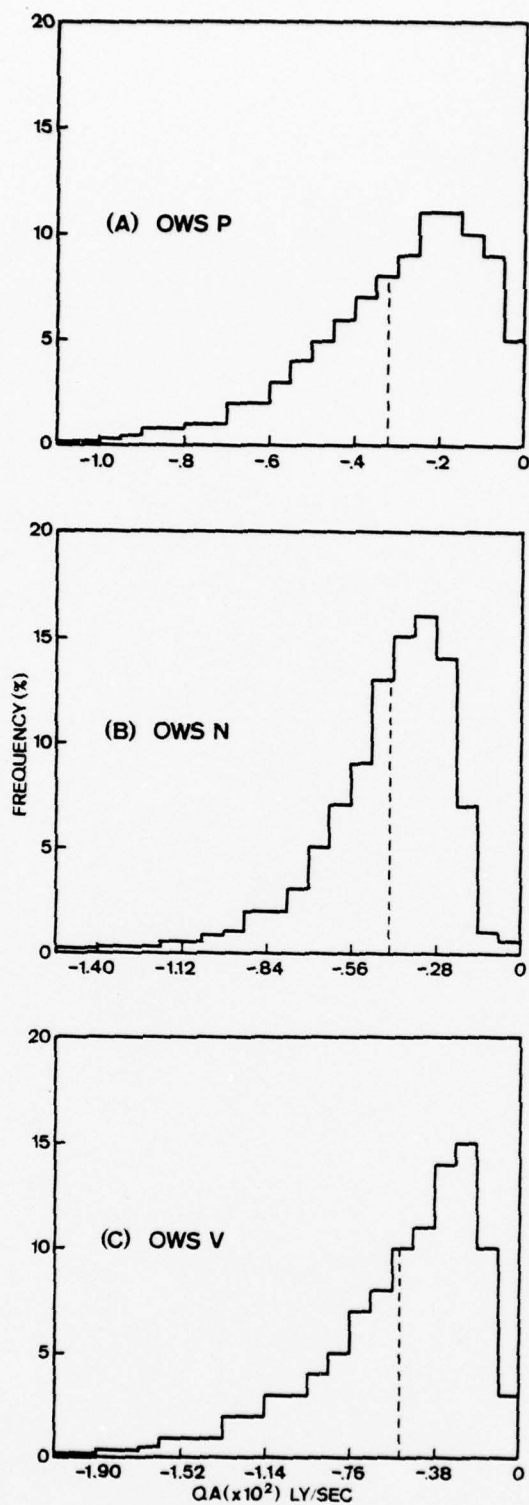


Figure 5-2. Histograms of upward turbulent heat flux (Q_a) at OWS P, OWS N, and OWS V. The vertical dashed lines represent the mean of the distribution.

TABLE 5-1. Statistical characteristics of the histograms of wind (u_*), turbulent kinetic energy (u_*^3), and turbulent heat flux (Q_a).

Distribution	OWS P			
	Mean	Std. Dev.	Skewness	Kurtosis
u_* (cm/sec)	41.9	20.0	0.5	3.5×10^{-1}
u_*^3 (cm ³ /sec ³)	1.3×10^5	1.8×10^5	4.2	32.5
Q_a (ly/sec)	-3.2×10^{-3}	2.2×10^{-3}	-1.1	1.6

Distribution	OWS V			
	Mean	Std. Dev.	Skewness	Kurtosis
u_* (cm/sec)	30.3	15.8	0.9	1.6
u_*^3 (cm ³ /sec ³)	5.4×10^4	1.1×10^5	11.7	264
Q_a (ly/sec)	-5.5×10^{-3}	3.7×10^{-3}	-1.3	2.1

Distribution	OWS N			
	Mean	Std. Dev.	Skewness	Kurtosis
u_* (cm/sec)	23.2	11.7	0.9	2.3
u_*^3 (cm ³ /sec ³)	2.3×10^4	5.0×10^4	19.9	680
Q_a (ly/sec)	-4.3×10^{-3}	2.2×10^{-3}	-1.4	3.3

Tables 5-2 to 5-4 present a summation of the monthly means, and standard deviations about these means, of the principal air-sea parameters used to determine the atmospheric forcing depicted in the histograms. A smaller percentage of vapor pressure differences ($E_w - E_a$) were calculated (see note 2) because atmospheric moisture information was not always recorded.

The marine winds (u_a) are strongest at OWS P and weakest at OWS N, which accounts for the relative magnitudes of the u_* and u_*^3 distributions. However a more significant observation is that at OWS P and OWS V the increase in the magnitude of the winds, from September to December, is nearly double that observed at OWS N. The air-sea temperature difference ($T_w - T_a$) and saturated vapor pressure difference ($E_w - E_a$) are the additional parameters that are important for determining the turbulent heat fluxes. Tables 5-2 to 5-4 show that both of these parameters are significantly larger at OWS V and OWS N than at OWS P. As a consequence the smallest turbulent heat fluxes occur at OWS P, despite the largest observable winds.

The magnitudes of these air-sea differences are related to the location of the three stations relative to the mean atmospheric circulation in the North Pacific. The general westerly flow at OWS V and northeasterly flow at OWS N, together with the subsidence associated with the subtropical high pressure belt, continuously brings cold, relatively dry air in contact with the warm ocean at these two stations. At OWS P, however, the mean flow is westerly, the air mass has had considerable contact with the underlying ocean, and consequently the air-sea temperature and vapor pressure differences are small. Additionally it should be observed that these differences are much more variable at OWS P and V than at OWS N (compare the means and standard deviations at each station in Table 5-1). This

TABLE 5-2. Variability of atmospheric and oceanic parameters at OWS P.

VARIABLE	SEPT	OCT	NOV	DEC
u_a (m/sec)	9.5 (4.6)	11.7 (5.5)	12.5 (5.7)	12.6 (5.6)
$T_w - T_a$ ($^{\circ}\text{C}$)	0.1 (1.0)	0.5 (1.3)	0.7 (1.4)	0.5 (1.5)
$E_w - E_a$ (mb)	1.9 (1.8)	2.6 (2.0)	2.3 (1.6)	1.5 (1.4)

NOTE:

- (1) First value represents the monthly/seasonal mean of the three-hourly readings while the second (in parenthesis) is the standard deviation.
- (2) Statistics are based upon 90% (21,030) of the possible three-hourly observations of $E_w - E_a$ and 96% (25,524) of the remainder of the variables.

TABLE 5-3. Variability of atmospheric and oceanic parameters at OWS V.

VARIABLE	SEPT	OCT	NOV	DEC
u_a (m/sec)	6.7 (3.7)	7.8 (3.8)	9.2 (4.4)	10.1 (4.8)
$T_w - T_a$ ($^{\circ}$ C)	1.0 (1.4)	1.3 (1.6)	2.0 (2.0)	2.4 (2.2)
$E_w - E_a$ (mb)	8.1 (4.2)	7.9 (4.4)	8.7 (4.3)	8.0 (4.2)

NOTE:

- (1) First value represents the monthly/seasonal mean of the three-hourly readings while the second (in parenthesis) is the standard deviation.
- (2) Statistics are based upon 75% (10,930) of the possible three-hourly observations of $E_w - E_a$ and 96% (14,065) of the remainder of the variables.

TABLE 5-4. Variability of atmospheric and oceanic parameters at OWS N.

VARIABLE	SEPT	OCT	NOV	DEC
u_a (m/sec)	5.6 (2.9)	5.9 (2.9)	6.9 (3.3)	7.3 (3.4)
$T_w - T_a$ ($^{\circ}$ C)	0.9 (1.0)	1.2 (1.2)	1.5 (1.3)	1.5 (1.4)
$E_w - E_a$ (mb)	8.1 (2.3)	8.4 (2.7)	8.2 (2.9)	7.2 (3.0)

NOTE:

- (1) First value represents the monthly/seasonal mean of the three-hourly readings while the second (in parenthesis) is the standard deviation.
- (2) Statistics are based upon 76% (17,146) of the possible three-hourly observations of $E_w - E_a$ and 95% (23,377) of the remainder of the variables.

would explain the additional variance in Q_a at these two stations.

The magnitude and variability in these data suggest strongly that the characteristics of the marine atmosphere at OWS P and OWS V are closely related to the frequency and intensity of the large winter storms that occur at these locations. The atmospheric forcing at OWS N, on the other hand, is more closely coupled to the properties of the mean circulation.

To examine the relative distribution of the turbulent kinetic energy and the turbulent heat fluxes, the percentage of these quantities along with the percentage of observations in each class interval were computed. For example

$$PE_j = 100 \sum_{i=1}^n u_{*i}^3 / \sum_{k=1}^N u_{*k}^3 \quad (5-1)$$

represents the percentage of turbulent kinetic energy that occurs in the j^{th} interval, n is the number of observations in the interval, and N is the total number of observations. Percentages of the turbulent heat fluxes (Q_a) and wind (u_*) were calculated with similar expressions. These percentages were accumulated from the smallest to the largest values and are compared in Fig. 5-3 in the form of cumulative frequency diagrams. The values for the cumulative percentage of u_*^3 and Q_a are determined from the upper scale of the abscissa, while the cumulative percentage of observations are obtained from the lower scale. For example, Fig. 5-3A indicates that all observations of u_*^3 less than $10^5 \text{ cm}^3\text{-sec}^{-3}$ account for 74%/90%/97% of the total observations at OWS P/V/N, but account for only

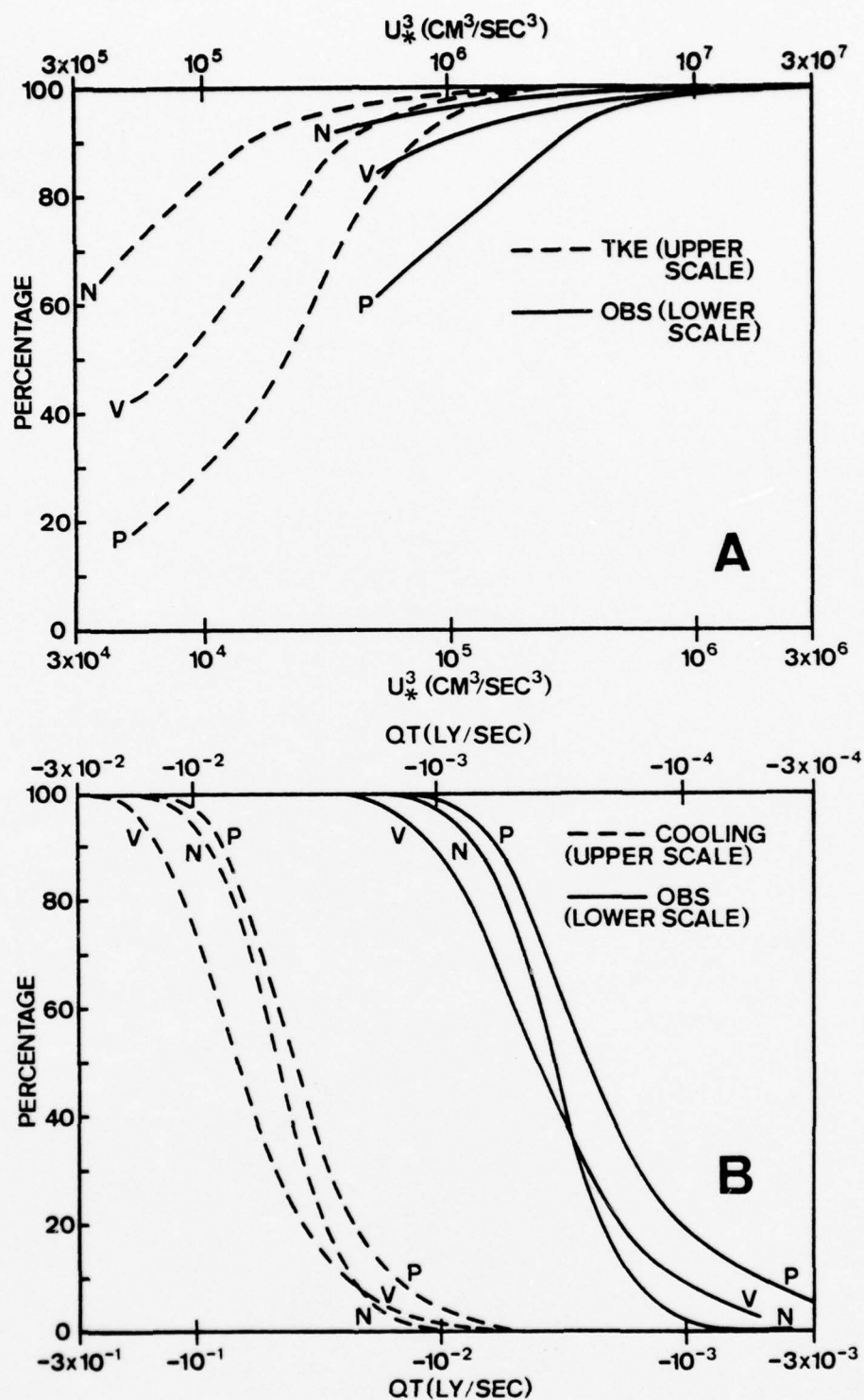


Figure 5-3. Cumulative percentage of turbulent kinetic energy (TKE), surface cooling, and observation at OWS P, OWS N, and OWS V. (See text for explanation.)

30%/56%/83% of the turbulent kinetic energy flux computed from these records. Similar comparisons can be made regarding the distribution of the turbulent heat fluxes from Fig. 5-3B (except that increasing values are read to the left). The horizontal displacement in these curves indicates that the turbulent kinetic energy exchange at the three stations increases from a minimum at OWS N to a maximum at OWS P, while the turbulent heat fluxes are smallest at OWS P and largest at OWS V. The example just presented indicates that at all stations a large percentage of the observations account for a relatively smaller percentage of the turbulent kinetic energy fluxes.

It is easily verified from Fig. 5-2B that this is also valid for the turbulent heat fluxes. Furthermore the characteristic shape of the u_*^3 curves suggest that although the magnitude of the turbulent kinetic energy flux is different at each station its distribution is quite similar. The shape of the Q_a curves would indicate that the distributions of turbulent heat fluxes are similar at OWS V and OWS P but slightly different at OWS N.

Additional information may be obtained by plotting the cumulative percentages of u_*^3 , Q_a , and u_* against the cumulative percentages of observations, as in Fig. 5-4. The first important observation from these curves is the relative invariance in the distribution of u_* and u_*^3 at the three stations (in these figures there is less than 3% scatter). Although these curves were constructed from the entire sample of values, curves drawn from the individual monthly values were nearly identical, and indicate that these distributions are also invariant with respect to month during the cooling season. The distribution of Q_a was identical to u_* at OWS N while at OWS P and OWS V the curves indicate a higher percentage of

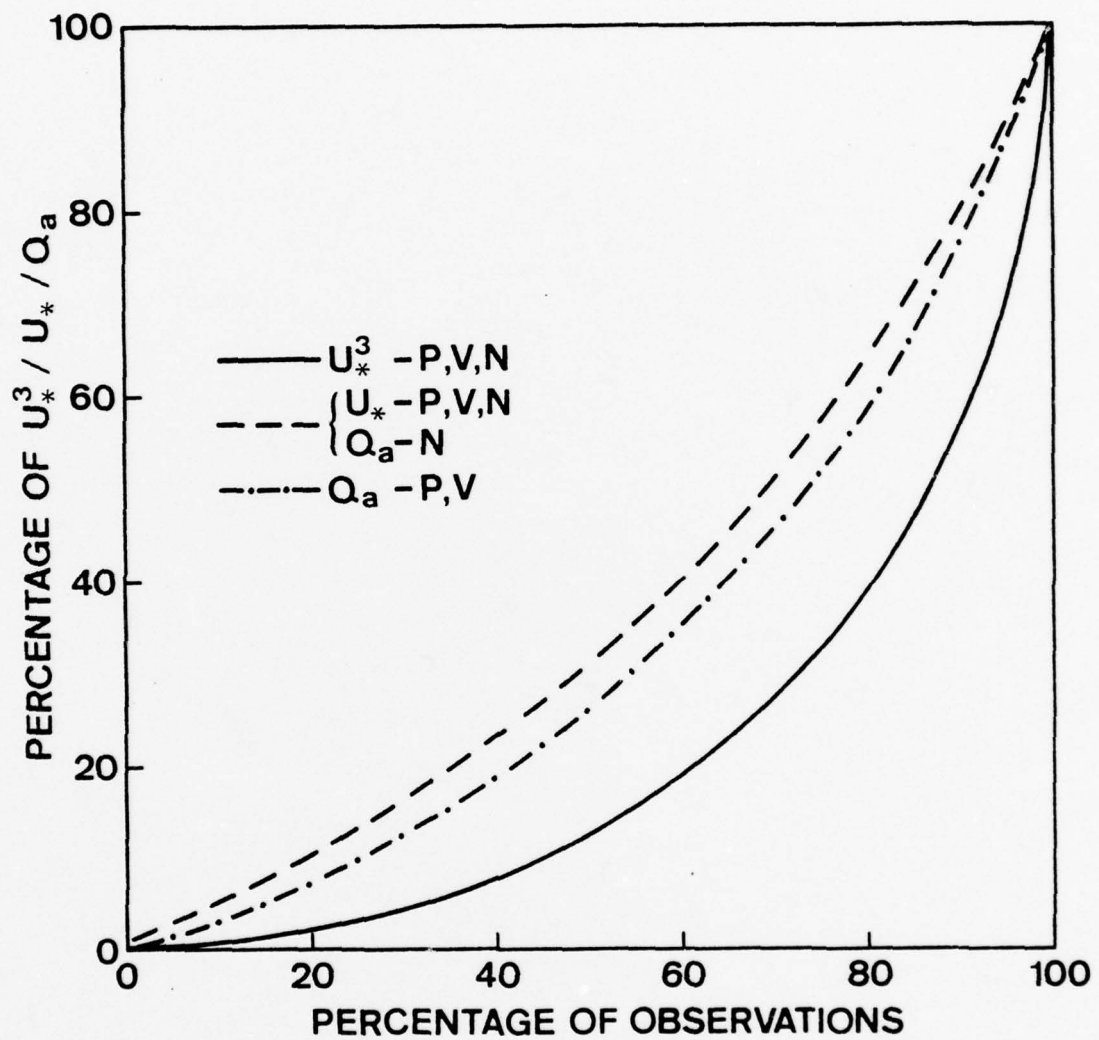


Figure 5-4. Percentage of $u_*^3 / Q_a / u_*$ as a function of percentage of observations.

large turbulent heat fluxes. For example 60% of the observations account for 40% of the cooling at OWS N but only 35% at OWS P and OWS V. Again this is due to the additional variance introduced by the air-sea temperature and vapor pressure differences at OWS P and OWS V.

An interesting observation from the u_*^3 curve is that it is represented by the function $FE^2 = 200 PE - PE^2$, where FE is the cumulative percentage of observations and PE is the cumulative percentage of u_*^3 . This function represents the locus of the circle centered at (0,100) with a radius equal to 100. A simple geophysical interpretation of this property is that a considerable number of small values of the wind account for only a small percentage of the total turbulent kinetic energy flux, while a few large values represent a considerable percentage of the total flux. Additionally, but to a lesser extreme, the Q_a curves demonstrate a similar relationship for the turbulent heat fluxes.

These relationships suggest strongly that a significant percentage of the turbulent kinetic energy and surface heat flux is exchanged at the air-sea interface during relatively short, but strong, atmospheric forcing events. Furthermore it is postulated that these events are directly associated with the passage of extratropical cyclones at OWS P and OWS V. At OWS N, however, these events are probably related to a pulsing in the mean flow, resulting from an alternate strengthening and weakening of the north-south pressure gradient as these storms pass to the north of OWS N. Additional evidence to support this assumption will be presented in the final section of this chapter when the distinguishing characteristics of these events are examined.

C. COMPARISON OF THE LONG-TERM MEAN FORCING AND OCEANIC RESPONSE AT THE OCEAN WEATHER STATIONS

In this section the long-term mean daily averages, depicted previously in Fig. 3-1, will be examined to determine the mean energetics of the forcing at the three ocean weather stations and the magnitude of the mean oceanic thermal response. The quantities will be used in subsequent analysis as a basis for determining what constitutes strong forcing and strong oceanic response. We will also present additional evidence from these data that is supportive of the assumption that the character of the atmospheric forcing at OWS P and OWS V is determined by the synoptic storm patterns, and at OWS N by the mean flow. Finally simple one-dimensional reasoning will be applied to these data to demonstrate that the major features of the long-term mean thermal response are explainable in terms of simple vertical processes.

To obtain the energetics of the forcing, the daily mean values of u_*^3 , Q_a , Q_s , and Q_n were summed and the monthly totals are presented in the first four columns of Tables 5-5 to 5-7. The next two columns show the long-term mean monthly changes in the sea-surface temperature (ΔSST) and the mixed layer depth (ΔMLD). The relative contribution of the net surface heat flux (ΣQ_n) to the mean sea-surface temperature change is presented in the last column as $\Delta SST(\Sigma Q_n)$. This contribution was estimated by distributing ΣQ_n over the mean layer depth at the beginning of the month (upper value), and at the end of the month (lower value). Since the layer deepens between these two depths, the actual contribution of ΣQ_n is somewhere between these two extremes.

The seasonal trends in the forcing may be examined to show that both the magnitude and variability of these quantities correlates well with the locations of the ocean weather ships relative to the major storm

TABLE 5-5. Long-term mean forcing and mixed layer response at OWS P (24 year average).
Value in parenthesis is the standard deviation about the monthly mean. (See
text for explanation.)

MONTH	$\Sigma u_z^3 (\times 10^{-12})$ (cm^3/sec^2)	$\Sigma Q_a (\times 10^{-5})$ (ly/month)	$\Sigma Q_s (\times 10^{-5})$ (ly/month)	$\Sigma Q_n (\times 10^{-4})$ (ly/month)	ΔSST ($^{\circ}\text{C}/\text{mo}$)	ΔMLD (M/mo)	$\Delta \text{SST}(\Sigma Q_n)$ ($^{\circ}\text{C}/\text{mo}$)
SEPT	0.177 (0.062)	-0.046 (0.015)	0.063 (0.014)	0.169 (0.089)	-1.0 (1.0)	-10	+0.6 +0.4
OCT	0.333 (0.131)	-0.079 (0.025)	0.047 (0.011)	-0.325 (0.190)	-2.8 (1.3)	-24	-0.8 -0.5
NOV	0.387 (0.149)	-0.081 (0.023)	0.025 (0.056)	-0.564 (0.187)	-2.0 (0.9)	-21	-0.9 -0.7
DEC	0.375 (0.133)	-0.077 (0.034)	0.016 (0.036)	-0.613 (0.316)	-1.2 (0.7)	-17	-0.7 -0.6

TABLE 5-6. Long-term mean forcing and mixed layer response at OWS V (15 year average).
Value in parenthesis is the standard deviation about the monthly mean. (See text for explanation.)

MONTH	$\Sigma u_*^3 (\times 10^{-12})$ (cm^3/sec^2)	$\Sigma Q_a (\times 10^{-5})$ (ly/month)	$\Sigma Q_s (\times 10^{-5})$ (ly/month)	$\Sigma Q_n (\times 10^{-4})$ (ly/month)	ΔSST ($^{\circ}\text{C}/\text{mo}$)	ΔMLD (M/mo)	$\Delta \text{SST}(\Sigma Q_n)$ ($^{\circ}\text{C}/\text{mo}$)
SEPT	0.074 (0.042)	-0.106 (0.020)	0.114 (0.009)	0.075 (0.218)	-1.0 (1.2)	-1.0	+0.3 +0.2
OCT	0.104 (0.038)	-0.127 (0.026)	0.087 (0.008)	-0.406 (0.285)	-2.1 (1.1)	-17	-1.2 -0.8
NOV	0.160 (0.046)	-0.149 (0.031)	0.058 (0.004)	-0.906 (0.296)	-2.2 (1.8)	-27	-1.7 -1.1
DEC	0.211 (0.041)	-0.165 (0.037)	0.048 (0.005)	-1.174 (0.340)	-2.5 (1.8)	-12	-1.5 -1.3

TABLE 5-7. Long-term mean forcing and mixed layer response at OWS N (23 year average).
Value in parenthesis is the standard deviation about the monthly mean. (See
text for explanation.)

MONTH	$\Sigma u_*^3 (x10^{-12})$ (cm^3/sec^2)	$\Sigma Q_a (x10^{-5})$ (ly/month)	$\Sigma Q_s (x10^{-5})$ (ly/month)	$\Sigma Q_n (x10^{-4})$ (ly/month)	ΔSST ($^{\circ}C/mo$)	ΔMLD (M/mo)	$\Delta SST(\Sigma Q_n)$ ($^{\circ}C/mo$)
SEPT	0.035 (0.036)	-0.096 (0.014)	0.119 (0.010)	0.234 (0.196)	0 (0.9)	-11	+0.8 +0.6
OCT	0.041 (0.015)	-0.108 (0.016)	0.096 (0.007)	-0.111 (0.161)	-0.9 (0.9)	-19	-0.3 -0.2
NOV	0.065 (0.029)	-0.118 (0.023)	0.071 (0.007)	-0.480 (0.235)	-1.2 (0.7)	-17	-0.8 -0.6
DEC	0.078 (0.027)	-0.113 (0.025)	0.059 (0.005)	-0.539 (0.246)	-1.3 (1.2)	-14	-0.7 -0.6

tracks in the North Pacific. As expected, the largest flux of turbulent kinetic energy (Σu_*^3) is received at OWS P and the smallest at OWS N, with a general increase in magnitude during the season at all stations. At OWS P and OWS V, however, Σu_*^3 increases rather abruptly in October and November respectively. It is quite evident that at OWS N no abrupt changes in Σu_*^3 occur during the cooling-season in any month. This is rather suggestive that at OWS P and OWS V these abrupt increases in Σu_*^3 mark the onset of the winter storm season at these stations. At OWS N the trend in Σu_*^3 would suggest a slow intensification of the wind, which would be indicative of the wintertime strengthening of the mean circulation.

The monthly Q_a values at the three stations show the same relationships as previously noted in the histograms (Fig. 5-2). The most intense turbulent heat fluxes occur at OWS V and the weakest at OWS P. By comparing the mean and standard deviations of ΣQ_a at the three stations, it may be noted again that the turbulent heat fluxes are more variable at OWS P and OWS V than at OWS N. As expected, the effective solar insolation, ΣQ_s , decreases throughout the season and with latitude. Additionally it should be observed that the insolation at OWS P has much more variability than at the other stations. Since this can only be introduced by the total cloud cover (see Appendix A), it is indicative of the changes in the cloud patterns that accompany the cyclonic storms at OWS P. At OWS P the cloud-types are normally low stratus and the sky frequently covered by heavy overcast throughout this season. The exception to this pattern occurs in the cold, dry air mass behind the cold front where the cloud patterns are broken and, therefore, allow more insolation to reach the sea surface. At OWS V and OWS N, however, the sky is not normally overcast

and the storm systems do not introduce as much variability in the total cloud amounts. Finally the net heat gain or loss by the ocean is reflected in the fourth column of Tables 5-5 to 5-7 as ΣQ_n . There is a net heat gain, at all stations, during September and this downward heat flux is largest at OWS N and smallest at OWS V. During the remaining three months ΣQ_n is increasingly negative, at all stations, and is most negative at OWS V and least negative at OWS N.

The oceanic thermal response has characteristic trends, at each station, that we will attempt to explain with one-dimensional reasoning. The total mixed layer depth change (ΔMLD) is largest at OWS P and smallest at OWS N; however, the trend is similar at all three stations. The deepening rate increases early in the season and is reduced at the end. The seasonal sea-surface temperature change (ΔSST) is comparable at OWS V and OWS P, but significantly smaller at OWS N. It should be noted that the trend in ΔSST is different at OWS P than at OWS V and OWS N. At OWS V and OWS N, ΔSST increases throughout the season, while at OWS P ΔSST increases during October and decreases in the final two months.

If one-dimensional reasoning is applied to the long-term forcing and oceanic response, a considerable amount of the observed changes are explainable. Consider first the amount of the monthly sea-surface temperature change (ΔSST) that may be explained by the net surface flux (ΣQ_n). September, at all stations, marks the transition between the heating and cooling seasons and the data indicate that the surface fluxes increase the heat content of the upper ocean at all stations. This occurs during a period when the sea-surface temperature is normally decreasing at OWS P and OWS V, and unchanging at OWS N. Therefore the sea-surface temperature change, during September, cannot be explained (and certainly not predicted) in terms of the surface heat fluxes alone. The net surface

fluxes become increasingly negative from October to December; however, $\Delta SST(\Sigma Q_n)$ increases from October to November and then decreases in December. This is because the ratio of the net surface fluxes to the mixed layer depth increases from October to November and decreases in December (i.e. $\Delta SST(\Sigma Q_n) \pm \frac{1}{h} \Sigma Q_n$). This illustrates the importance of the mixed layer depth in determining the effect of surface fluxes on the sea-surface temperature change.

The relative importance of the surface fluxes to the total sea-surface temperature change may be ascertained by comparing the cumulative contribution of $\Delta SST(\Sigma Q_n)$ in Tables 5-5 to 5-7, for the final three months, with the total sea-surface temperature change during these months. At OWS V and OWS N greater than one-half of ΔSST may be directly explainable by $\Delta SST(\Sigma Q_n)$, while at OWS P only one-third is explainable. Finally, as a measure of the dominance of the surface fluxes, consider the months during which $\Delta SST(\Sigma Q_n)$ accounts for greater than 50% of ΔSST . At OWS V and OWS N these fluxes become dominant during November while at OWS P this does not occur until December. It is evident that, even during the months when these surface fluxes appear dominant, they are not capable of explaining the total sea-surface temperature change.

The other significant vertical process which might explain the difference between ΔSST and $\Delta SST(\Sigma Q_n)$ is the heat flux at the base of the mixed layer that occurs during entrainment. In fact, during large deepening events, the entrainment heat flux may actually dominate the surface heat flux, as was demonstrated in the previous chapter. Since this heat flux cannot be computed from these data, we must infer its relative magnitude from the turbulent kinetic energy flux (Σu_*^3), the mixed layer depth change (ΔMLD), and the characteristic thermal structure at the three ocean weather stations.

It is important to observe that nearly twice the turbulent kinetic energy is transferred to the ocean at OWS P as at OWS V, and greater than five times as much as at OWS N. Additionally, the maximum seasonal residuals between ΔS_{ST} and $\Delta S_{ST} (\Sigma Q_n)$ that must be explained are -5.2°C , -3.7°C , and -2.4°C at OWS P, OWS V, and OWS N respectively. The relative magnitudes of these fluxes and residuals are understandable in terms of (2-49), (2-50), and the fundamental differences in the thermal structure at the three stations, illustrated in Fig. 5-5. The characteristic shape of the profiles at OWS V and OWS N are quite similar, but considerably different than the profile at OWS P. This is because at both OWS V and OWS N the parent water mass is North Pacific Central (Sverdrup, 1942), while the water mass at OWS P is Pacific Subarctic. However, the important difference to be observed in the three profiles is the magnitude of the temperature gradient immediately below the mixed layer. The temperature change from 70-80 meters is approximately $2.5^\circ\text{C}/2.1^\circ\text{C}/1.5^\circ\text{C}$ at OWS P/OWS V/OWS N. The relative magnitudes of the temperature difference (ΔT) at the base of the mixed layer is in the same proportion at the beginning of September.

Equations (2-49) and (2-50) indicate that the largest amount of turbulent kinetic energy would be required to mix the upper layers of the ocean at OWS P and the least at OWS N. This is completely consistent with the relative magnitudes of Σu_*^3 noted previously in Tables 5-5 to 5-7. Additionally, comparing ΔMLD and ΔT at each station, we should expect the largest entrainment heat flux ($\frac{\partial h}{\partial t} \Delta T$) at OWS P and the smallest at OWS N. This is consistent with the relative magnitudes of the sea-surface temperature residuals computed at the three stations.

The seasonal trend in the mixed-layer depth is understandable in terms of the magnitude of Σu_*^3 and the concept of dissipation enhancement,

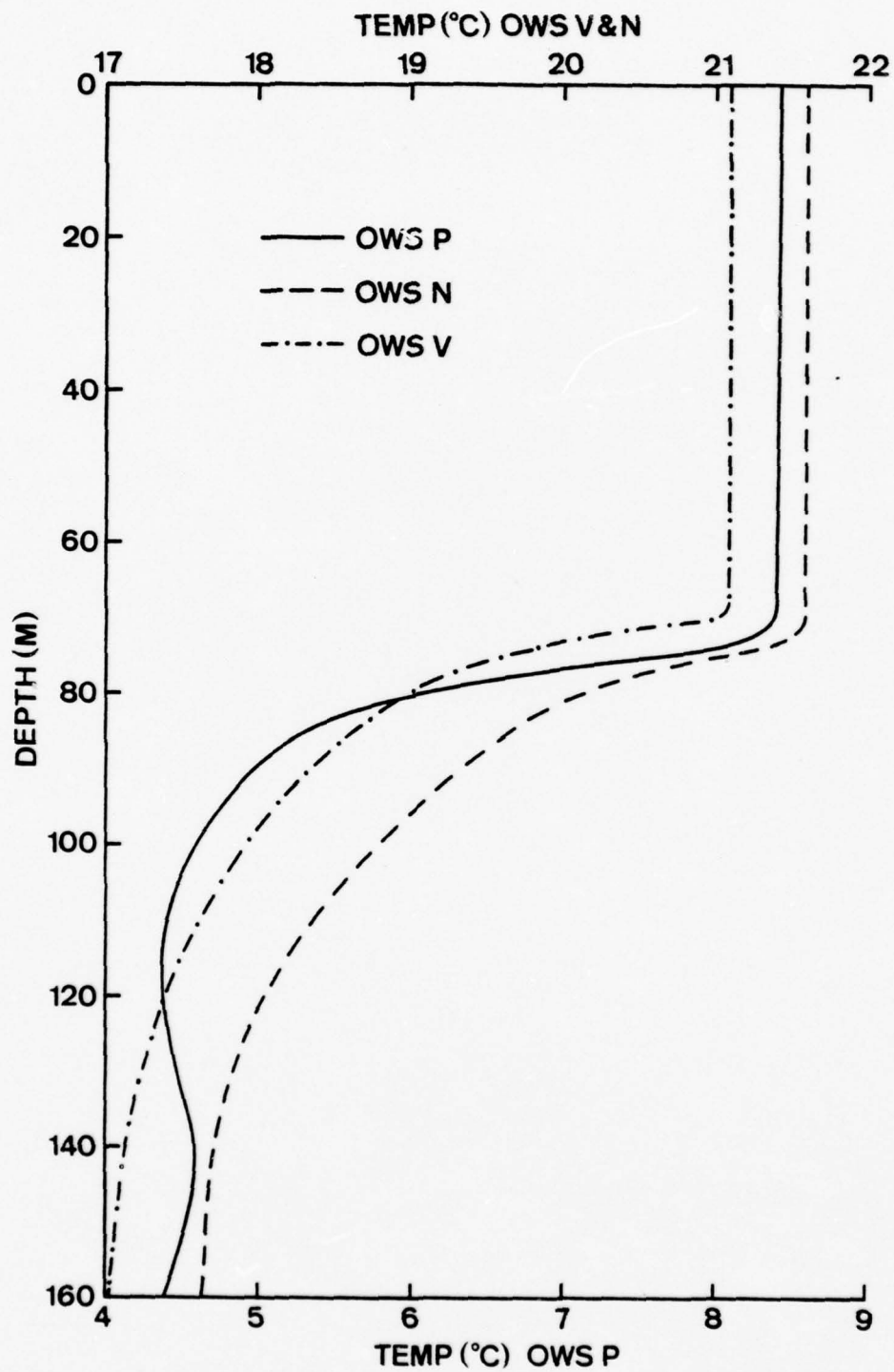


Figure 5-5. Typical mid-season temperature profiles at the three ocean weather stations.

discussed in the previous chapter. As the layer deepens, the entrainment zone is displaced from the surface production zone, and a greater percentage of the turbulent kinetic energy is dissipated. In accordance with (2-33) as the ratio of G_*-D_* and h decreases the mixed layer deepening rate also decreases. This occurs in November at OWS P and OWS N and in December at OWS V.

It is encouraging to note the major trends in these data are consistent with simple one-dimensional reasoning. However, it is important to realize that these trends are not explainable solely in terms of the surface forcing. It is necessary to be able to specify both the surface heat flux and the entrainment heat flux to accurately describe the seasonal mixed layer evolution. The entrainment heat flux will dominate the surface heat flux early in the season when $\frac{\partial h}{\partial t}$ and ΔT are large and the surface heat fluxes are small. By the end of the season the large surface heat fluxes become the dominant factor in changing the sea-surface temperature.

D. IMPORTANCE OF LARGE ATMOSPHERIC FORCING EVENTS IN DETERMINING THE SEASONAL EVOLUTION OF THE MIXED LAYER

In this section the seasonal evolution of the mixed layer will be examined relative to the long-term mean trend to illustrate the importance of large atmospheric forcing events in changing the upper ocean thermal structure. The purpose of this analysis will be to demonstrate that the timing of the first large storms (whether they occur early or late in the season) is very important to the seasonal evolution of the mixed layer. Evidence will be presented to illustrate that the underlying thermal structure is as important as the surface forcing. Two cooling seasons, taken from the OWS P record, were chosen to demonstrate these principles,

because both the atmospheric forcing and the thermal structure were very different during these two years.

Mid-October temperature profiles (Fig. 5-6) illustrate that the mixed layer was deeper and cooler during 1963 than during 1959. Notice also that the temperature gradient at the base of the layer during 1963 was considerably weaker than during 1959. The final observation is that in 1963 there was a much stronger thermal gradient below 60 meters during 1963 than in 1959.

Figures 5-7 and 5-8 depict the observed forcing and oceanic response during these two seasons, with the long-term mean trends superimposed. In Table 5-8 the strength of the forcing and response characteristics are presented and compared with the long-term mean. In Figs. 5-7A,B it is observed that at the start of the 1959 season the mixed layer was considerably deeper and cooler than the long-term mean. However, at the beginning of September 1963 a very warm, shallow layer is present (Figs. 5-8A,B).

The character and timing of the atmospheric forcing during these two seasons may be observed in Figs. 5-7C,D and 5-8C,D. During 1963, the period from 15 October to 1 November marks the beginning of the winter storm season. In 1959, with the exception of the one significant event in mid-October, the large forcing events do not begin until mid-November. The difference in these storm patterns coupled with the different initial temperature structures result in the evolution of the upper ocean being quite different during these two seasons (compare Figs. 5-7A,B and 5-8A,B). In the previous chapter, it was demonstrated that large forcing events that occur early in the season produce much larger oceanic thermal responses than events occurring late in the season. This is consistent with what is observed in Figs. 5-7 and 5-8, and we will examine the

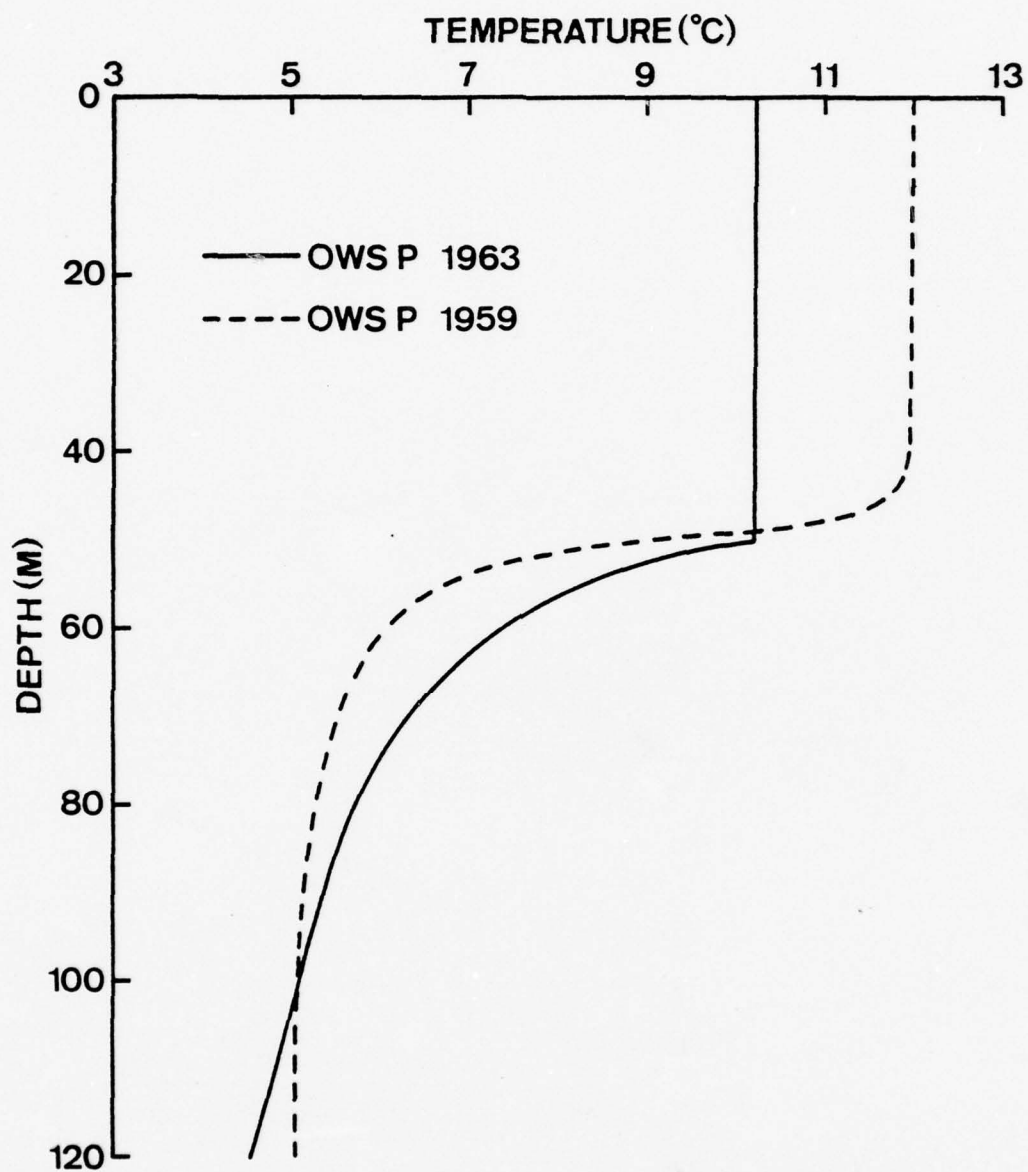


Figure 5-6. Mid-October temperature profile at OWS P.

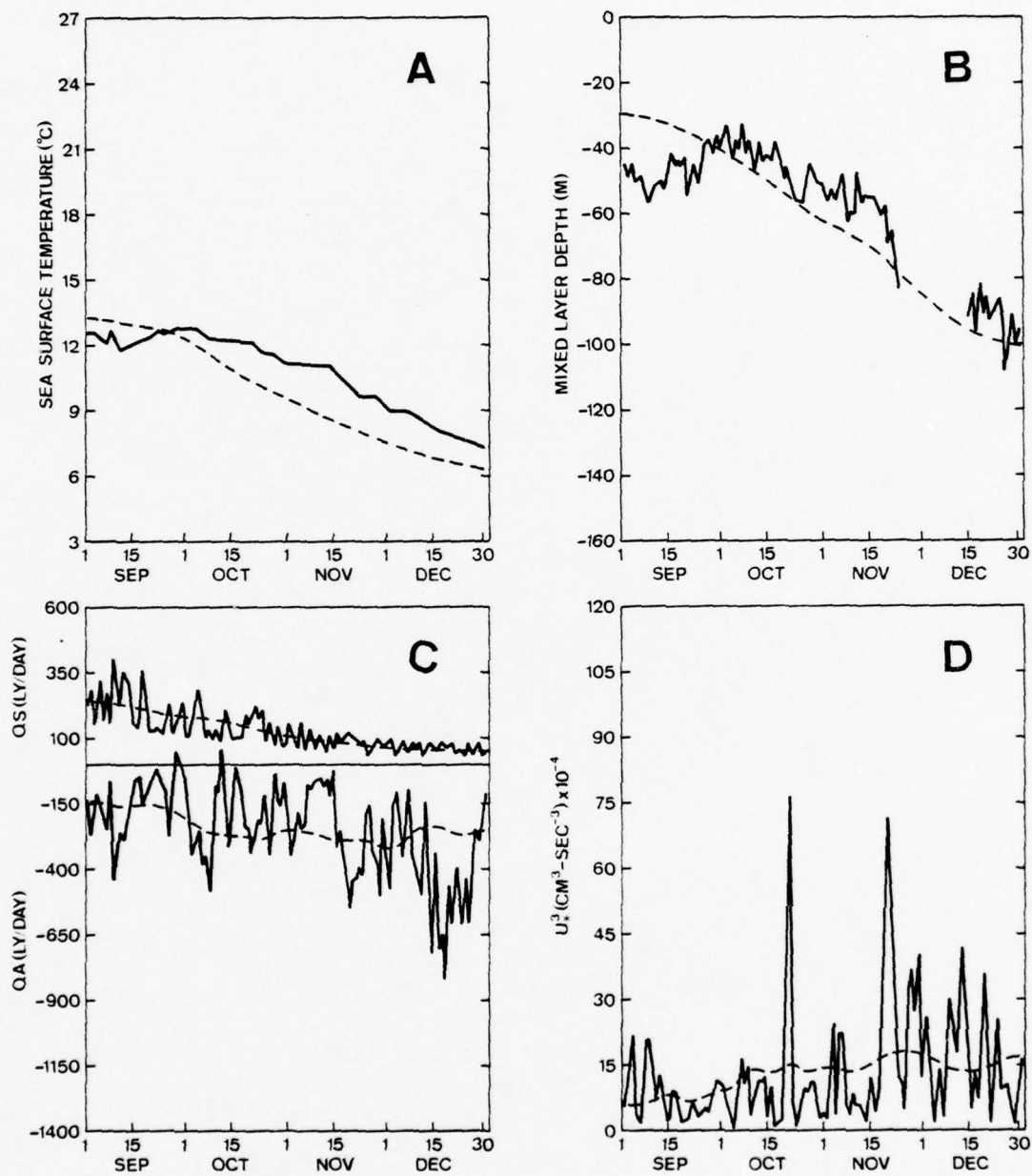


Figure 5-7. Atmospheric forcing and oceanic response at OWS P for the 1959 cooling season.

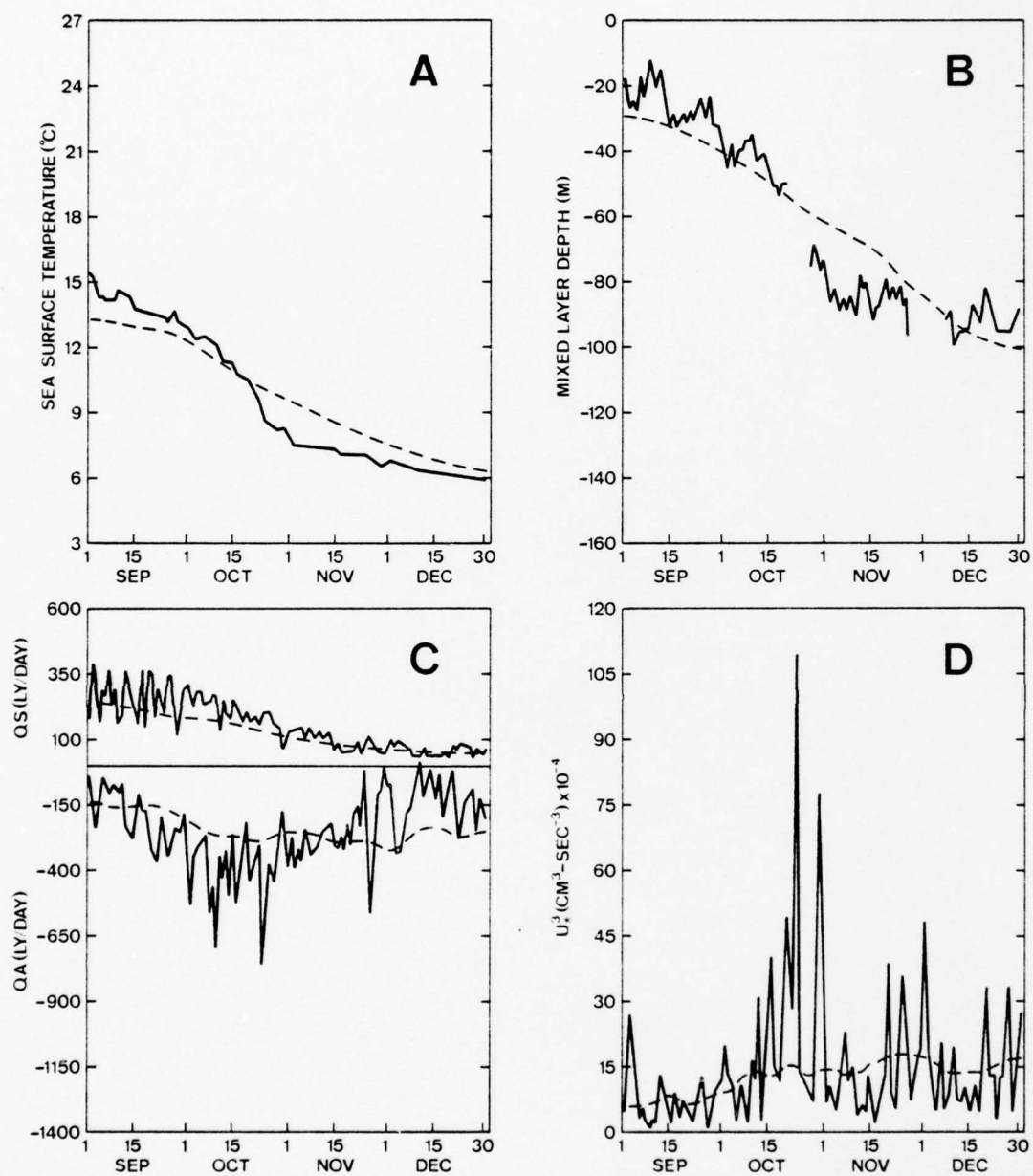


Figure 5-8. Same as Figure 5-7 except for the 1963 cooling season.

TABLE 5-8. Atmospheric forcing and response at OWS P for the years 1959 and 1963.

Forcing and Response (as a percentage of the seasonal total)													
1963							1959						
Month	%u _* ³	%Q _a	%Q _s	%Q _n	%ΔMLT	%ΔMLD	Month	%u _* ³	%Q _a	%Q _s	%Q _n	%ΔMLT	%ΔMLD
Sept	12	20	42	-11	25	21	Sept	15	14	42	-12	-6	-16
Oct	40	40	34	49	51	51	Oct	21	21	30	14	27	27
Nov	23	26	15	41	16	*	Nov	35	25	16	33	38	*
Dec	25	14	9	21	8	*	Dec	29	40	12	65	41	*

*Missing Data

Forcing and Response (as a percentage of the long-term mean)													
1963							1959						
Month	%u _* ³	%Q _a	%Q _s	%Q _n	%ΔMLT	%ΔMLD	Month	%u _* ³	%Q _a	%Q _s	%Q _n	%ΔMLT	%ΔMLD
Sept	95	134	119	81	248	150	Sept	115	93	99	116	-28	-80
Oct	176	156	130	13	174	154	Oct	83	84	95	69	51	58
Nov	86	96	107	41	75	*	Nov	121	95	97	94	98	*
Dec	99	56	106	43	66	*	Dec	104	150	118	171	181	*
Season	114	108	120	94	137	100	Season	106	109	99	121	76	71

Oceanic Response (1963)		
Month	MLT(°C)	MLD(M)
Sept	15.3-12.9	38-43
Oct	12.9- 8.1	54-70
Nov	8.1- 6.6	70-77
Dec	6.6- 5.8	* -90

Oceanic Response (1959)		
Month	MLT(°C)	MLD(M)
Sept	12.5-12.8	45-37
Oct	12.8-11.4	37-51
Nov	11.4- 9.4	51-*
Dec	9.4- 7.2	* -96

Oceanic Response (long-term mean)		
Month	MLT(°C)	MLD(M)
Sept	13.3-12.3	28-38
Oct	12.3- 9.5	38-62
Nov	9.5- 7.5	62-83
Dec	7.5- 6.3	83-100

oceanic evolution during these two seasons to show that the major features are explainable by one-dimensional reasoning.

During 1963 the month of September had weaker than normal downward fluxes of turbulent kinetic energy (u_*^3) and heat (Q_n) (compare percentage of long-term mean in Table 5-8). The mixed layer, however, deepened and cooled more than the long-term mean. The larger than normal deepening and cooling rate was the result of the layer being warm and very shallow at the beginning of the period. Because the layer was shallow, only a relatively small amount of turbulent kinetic energy was dissipated, which resulted in the large entrainment rate. As would be expected, the vertical re-distribution of the heat in this warm layer resulted in a larger than normal entrainment heat flux and consequently abnormal sea-surface temperature change. During October 1963 the large winter storms are responsible for an energy exchange between the atmosphere and ocean which is significantly larger than the long-term mean. These large fluxes force the mixed layer to deepen and cool, such that by the end of the month the layer is deeper (8 m) and cooler (1.4°C) than the long-term mean. During these first two months 52%(60%) of the seasonal $u_*^3(Q_a)$ was received by the ocean, which is 10% greater than the long-term average. However, this abnormal forcing accounted for 75% of the mixed layer response during the season, which is 25% greater than normal. This large response occurred because the strong forcing came early in a season when a large heat storage had taken place in a very shallow mixed layer.

The final two months of 1963 were characterized by weaker than normal forcing. The upward heat fluxes (Q_n) account for only 40% of the seasonal total (10% less than normal) and this is a consequence of the anomalously cool sea-surface temperatures. The turbulent kinetic energy flux (u_*^3) received during the final two months is less than the long-term average

but is actually about the same amount received during the first two months (48% of the seasonal total). However, the response of the layer is only 25% of the seasonal total. The turbulent kinetic energy flux received during the final two months is simply not sufficient to accomplish any significant deepening. Evidently this is because the entrainment zone is deeper than normal, a larger percentage of the turbulent kinetic energy is dissipated, and the ratio of $G_* - D_*$ to h is less than normal.

Examination of the total seasonal forcing (Table 5-8) shows that greater turbulent kinetic energy and smaller net heat fluxes were exchanged at the air-sea interface during the 1963 season, which resulted in a normal seasonal deepening rate but a larger-than-normal sea-surface temperature change. This is consistent with our earlier findings that a temperature structure that has a large heat storage in the near surface layers will require a large amount of energy flux to deepen the layer. Additionally this deepening will be accompanied by a large entrainment heat flux and, consequently, a large sea-surface temperature change.

This example demonstrates clearly that the energy fluxes received early in the season results in a much larger mixed layer response than comparable energy fluxes received late in the season. An additional observation is that during September and October the anomalously large upward heat fluxes (Q_a) are accompanied by significantly larger-than-normal downward fluxes of solar radiation (Q_s). This supports our previous suggestion that the large variance in Q_s (Table 5-5) at OWS P is due to the large winter storms. The air mass is generally cold and dry during stormy periods and there is usually less cloud cover than the mean winter conditions.

The evolution of the mixed layer during the 1959 season was quite different than during 1963 (Figs. 5-8A,B). Since the mixed layer was deeper and cooler than normal at the start of the season, it is presumed that a significant re-distribution of the heat was accomplished by strong summer forcing (evidence will be presented to support this presumption). The turbulent kinetic energy was stronger than normal during September 1959, but so was the downward net surface heat flux (see Table 5-8). As a result, the mechanical energy was insufficient to mix this additional heat to the old mixed layer depth and a new shallower mixed layer formed above the old one (see Figs. 5-8A,B). By the end of the month the layer depth had retreated to near the long-term mean while the temperature is warmer than normal. The forcing received during October 1959 is much weaker than normal and only a weak mixed layer response takes place. The forcing received during the month of November is characterized by extremely strong mechanical forcing while the upward heat fluxes are smaller than normal. Because of the gap in the bathythermograph record it was not possible to determine the mixed layer depth at the end of the month. However, Fig. 5-8B would seem to indicate that the deepening rate is larger than normal. Because the net surface flux (Q_g) is less than normal the sea-surface temperature decreases only a normal amount and at the end of the month the layer is probably deeper but significantly warmer than normal. December 1959 is characterized by average mechanical forcing but extremely larger upward turbulent heat fluxes. The sea-surface temperature change is much larger than the long-term mean as a result of the large surface heat fluxes. At the end of the season the layer depth is about normal but the sea-surface temperature is approximately 1°C warmer than normal.

The seasonal totals in Table 5-8 show that the forcing was actually stronger than the long-term mean and yet less than normal oceanic response occurred. This is primarily the result of the deep mixed layer that was present at the beginning of the season. The forcing during the first two months was not sufficient to establish the normal deepening and cooling rate. The large winter storms came late in the season and were not able to reduce the sea-surface temperature the additional amount necessary to bring the ocean back to the long-term mean.

These two examples illustrate that the timing of the strong atmospheric forcing events coupled with the characteristics of the underlying thermal structure are of primary importance in determining the evolution of the upper ocean during the cooling season. Once again it should be noted that the large forcing events produce a much greater oceanic response when the mixed layer depth is shallow (usually early in the season).

It may be seen in Fig. 5-5 that the temperature structure is quite different at OWS P than at OWS N and OWS V. Furthermore Fig. 5-6 shows that the thermal structure may have considerable variability from year to year at a particular location. Since the seasonal thermocline is established during the spring and summer, these figures would suggest that the mechanisms responsible for its formation may vary depending on location and year. The spring and summer forcing, observed during 1959 and 1963 at OWS P, were compared to see if the differences in the temperature structure, depicted in Figs. 5-6, 5-7A,B, and 5-8A,B, are explainable in terms of one-dimensional processes. The mechanical forcing observed during the spring in 1959 was much weaker than observed in 1963. However, the synoptic patterns observed during the summer indicates that the 1959 season was characterized by a high incidence of strong storm activity

while the forcing was extremely weak during 1963. Consequently the layer retreated very rapidly during the spring of 1959 and because very little heat was mixed below 60 meters, the seasonal thermocline below this level was nearly isothermal. On the other hand, during 1963 a considerable amount of heat was mixed into the deep layers by the strong spring forcing, and a relatively strong thermal gradient was established below 60 meters (see Fig. 5-6). The strong summer forcing during 1959 caused a large downward transfer of heat and resulted in a very deep, cool mixed layer at the beginning of September (see Fig. 5-7A,B). The weak forcing during the summer of 1963 was insufficient to maintain a normal summertime mixed layer depth and a very warm, shallow layer developed (see Fig. 5-8A,B).

This simple analysis suggests that the synoptic storms may be as important to the establishment of the seasonal thermocline during the heating season as they are to the subsequent erosion that takes place during the fall and winter cooling season. The evolution of the upper ocean during the cooling season is determined to a large extent by the nature of the stability of the thermocline. Therefore it is important to realize that the entrainment process may be influenced by the nature of the forcing during the previous spring. A simple conclusion would be that the spring and summer heating season should be examined in detail to determine the relationship between the principal mechanisms that govern the formation of the seasonal thermocline.

E. IMPORTANCE OF THE STRONG ATMOSPHERIC FORCING EVENTS AT THE THREE OCEAN WEATHER STATIONS

In this final section the total record (see Table 3-1) of the surface and near-surface parameters will be examined to determine the relative

importance of large forcing events to the total evolution of the upper ocean thermal structure. The objectives of this analysis will be to determine:

- (1) the principal characteristics of the large events at the three stations;
- (2) the percentage of the total energy that is exchanged during these events.

Figure 5-9 is presented to explain how the analysis was performed. An event will be defined as those individual periods when the forcing was greater than the long-term mean. For example, in Fig. 5-9 there are 12 individual events during the season. If the forcing is greater than the long-term mean at the beginning or end of the season it is counted as an event. If an event takes place during two months (for example events 3 and 9), the amount of energy received during each month is calculated and the event is credited to the month in which the largest energy exchange occurs. For example the third event in Fig. 5-9 would be credited to October and the ninth event to November. The duration of an event is defined as the time during which the forcing is greater than the long-term mean. An additional parameter was the ratio of the peak value of the forcing to the long-term daily mean. This peak-to-mean ratio (P_k) was used to examine the effects of the larger events. For instance we might only examine events where $P_k \geq 1.5$, etc. The analysis was performed first by defining the forcing events in terms of the u_*^3 curves (mechanical events). Next the analysis was repeated with the events defined by the Q_a curves (cooling events). The results from both of these definitions will be presented.

The response of the ocean thermal structure was estimated from the seasonal sea-surface temperature change (based on the surface marine

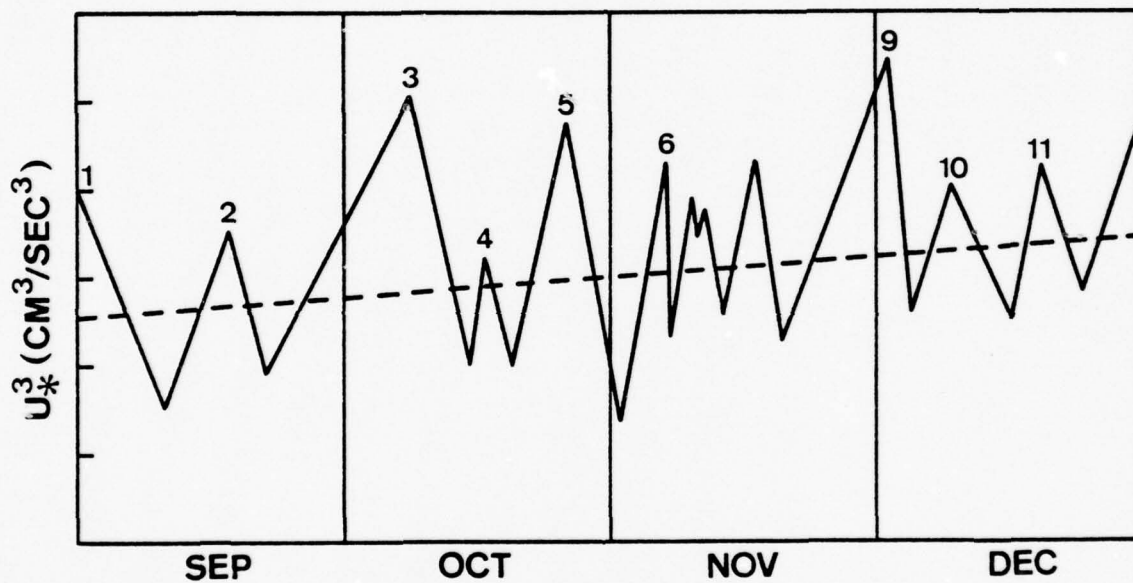


Figure 5-9. Characteristic of events.

observations) that occurred during each event. The ratio of the cumulative changes in sea-surface temperature taking place during the events to the total seasonal change is the percentage of the total response that occurs during the events. In a similar manner, the percentage of the total duration, u_*^3 and Q_n occurring during these events was calculated. The large data gaps in the bathythermograph record would not permit analysis of mixed layer depth during these events. However, the examples presented earlier in this chapter, and the results from the numerical models indicate that large changes in sea-surface temperature are normally accompanied by large changes in the mixed layer depth.

In the first part of this analysis we will examine the percentage of the monthly forcing and response that takes place when the forcing (either u_*^3 or Q_a) is greater than the long-term mean. The results of this analysis is presented in Tables 5-9 to 5-11 and is based upon the 24/23/15 seasonal records considered at OWS P/OWS N/OWS V.

The data presented in these tables is consistent with our original hypothesis that a significant percentage of the atmospheric forcing and oceanic response takes place during periods when the forcing is strong. The first observation is the relative invariance in the duration of the forcing at all stations. The mechanical events characteristically are shorter in duration than the cooling events because large air-sea temperature and vapor pressure differences persist longer than the strong winds. The relationship between the duration and the percentage of turbulent kinetic energy exchanged during these periods is also very consistent at all stations. At all stations a large percentage of u_*^3 takes place during a relatively short time frame. Although the magnitudes of these large energy events are significantly different at the three

TABLE 5-9. Atmospheric forcing and sea-surface temperature response at OWS P. Tabular values represent percentages of the monthly totals that occurred when the forcing (u_*^3 or Q_n) was greater than the long-term mean.

Forcing Variable	Percentage of forcing and response when u_*^3 greater than long-term mean				Percentage of forcing and response when Q_n greater than long-term mean			
	SEPT	OCT	NOV	DEC	SEPT	OCT	NOV	DEC
Duration (%)	35	36	36	37	44	49	49	46
u_*^3 (%)	70	69	71	70	62	93	62	69
Q_n (%)	20	58	49	52	-6	102	81	97
ASST (%)	103	68	56	66	121	77	73	83

TABLE 5-10. Atmospheric forcing and sea-surface temperature response at OWS V. Tabular values represent percentages of the monthly totals that occurred when the forcing (u_*^3 or Q_n) was greater than the long-term mean.

Forcing Variable	Percentage of forcing and response when u_*^3 greater than long-term mean				Percentage of forcing and response when Q_n greater than long-term mean			
	SEPT	OCT	NOV	DEC	SEPT	OCT	NOV	DEC
Duration (%)	28	35	34	35	36	40	45	37
u_*^3 (%)	70	74	70	63	59	62	62	54
Q_n (%)	-182	72	52	51	-333	118	79	67
ΔSST (%)	70	61	66	40	147	81	71	54

TABLE 5-11. Atmospheric forcing and sea-surface temperature response at OWS N. Tabular values represent percentages of the monthly totals that occurred when the forcing (u_3^* or Q_n) was greater than the long-term mean.

Forcing Variable	Percentage of forcing and response when u_3^* greater than long-term mean				Percentage of forcing and response when Q_n greater than long-term mean			
	SEPT	OCT	NOV	DEC	SEPT	OCT	NOV	DEC
Duration (%)	35	37	37	37	46	43	41	42
u_3^* (%)	80	76	76	75	84	71	66	61
Q_n (%)	-27	150	66	59	-15	167	86	80
ΔSST (%)	436	94	69	58	1838	103	78	61

stations, these data would support the suggestion, made from the histograms, that the distribution of u_*^3 is fairly invariant at the three stations. Because Q_n includes both Q_a and Q_s it is much more variable than u_*^3 . During September, for instance, when there is normally a net downward heat flux, a net upward heat flux takes place during these strong forcing periods (compare Q_n at each station). This simply means that in September the surface cooling that does take place probably occurs during these strong forcing periods. It is also evident from these data that there is net heating taking place during October at all stations. This is reflected by Q_n being greater than 100% during these months. As expected u_*^3 is larger in the mechanical events and Q_n is larger in the cooling events.

The final, and most significant observation, is that during all months (mechanical and cooling events) a significant percentage of the sea-surface temperature changes (ΔSST) takes place during a relatively short duration. Also the general trend in these data is that ΔSST decreases as the seasons progress. This is true for both the mechanical and the cooling events. This once again supports the argument that the large atmospheric forcing produces a larger oceanic response early in the season when the mixed layer is shallow.

The second part of the analysis was designed to determine the characteristics of these large events and their relative importance to the seasonal evolution of the thermal structure. The results of this analysis are presented in Tables 5-12 to 5-14 in the order of increasing peak-to-mean ratios (P_k). Therefore the statistics in Table 5-12 represent every period in the record identified as an event, while those in Tables 5-13 and 5-14 represent only those events where $P_k \geq 1.5$ and

TABLE 5-12. Characteristic forcing and response during events with peak-to-mean ratios greater than 1.0. (Values in parenthesis are standard deviations about the mean.)

Variable	Mechanical Events			Cooling Events		
	OWS P	OWS V	OWS N	OWS P	OWS V	OWS N
Duration (%)	36	33	36	46	41	43
u_*^3 (%)	70	68	77	69	59	69
Q_n (%)	56	61	97	97	90	119
ΔSST (%)	68	57	85	83	78	91
Number Events/Month	5.1 (1.8)	4.4 (1.7)	3.8 (1.4)	4.4 (1.8)	4.3 (1.6)	3.8 (1.4)
Duration of Event (Days)	2.2 (1.7)	2.3 (1.7)	2.9 (2.4)	3.2 (3.1)	2.8 (2.2)	3.6 (3.4)
Peak-to-Mean Ratio	1.8 (.93)	1.9 (1.6)	2.1 (5.3)	1.4 (.39)	1.4 (.42)	1.3 (.35)

TABLE 5-13. Characteristic forcing and response during events with peak-to-mean ratios greater than 1.5. (Values in parenthesis are standard deviations about the mean.)

Variable	Mechanical Events			Cooling Events		
	OWS P	OWS V	OWS N	OWS P	OWS V	OWS N
Duration (%)	22	20	22	19	17	15
u_*^3 (%)	48	44	55	34	30	33
Q_n (%)	35	37	71	45	46	63
ASST (%)	50	31	57	37	33	43
Number Events/Month	2.4 (1.4)	2.4 (1.5)	1.9 (1.3)	1.4 (1.1)	1.4 (1.2)	.75 (.08)
Duration of Event (Days)	2.8 (1.8)	2.6 (1.6)	3.6 (2.7)	4.3 (3.5)	3.6 (2.0)	6.1 (4.7)
Peak-to-Mean Ratio	2.4 (1.0)	2.5 (2.0)	3.0 (7.4)	1.9 (.39)	1.9 (.38)	1.9 (.36)

TABLE 5-14. Characteristic forcing and response during events with peak-to-mean ratios greater than 2.0. (Values in parenthesis are standard deviations about the mean.)

Variable	Mechanical Events			Cooling Events		
	OWS P	OWS V	OWS N	OWS P	OWS V	OWS N
Duration (%)	13	11	14	7	5	5
u_*^3 (%)	31	28	41	11	9	13
Q_n (%)	21	23	52	21	15	22
ASST (%)	35	22	38	14	10	13
Number Events/Month	1.2 (1.2)	1.3 (1.1)	1.1 (1.0)	.42 (.67)	.47 (.62)	.21 (.46)
Duration of Event (Days)	3.2 (2.0)	2.8 (1.6)	4.1 (3.2)	5.2 (4.2)	3.5 (1.9)	6.8 (5.1)
Peak-to-Mean Ratio	3.1 (1.1)	3.2 (2.5)	4.0 (9.8)	2.4 (.34)	2.4 (.34)	2.3 (.36)

$P_k \geq 2.0$ respectively. The first four entries in these tables (duration, u_*^3 , Q_n , ΔSST) are the percentage of the seasonal totals that occur during these events. The final three entries are useful for comparing the characteristics of the events at each station.

The data in these tables supports the hypothesis that a significant percentage of the energy exchange takes place during these large atmospheric forcing events and results in a large oceanic thermal response. This may be easily verified by comparing the relationship between duration, u_*^3 , Q_n , and ΔSST for both the mechanical and cooling events listed in Table 5-12. Once again it may be observed from this table that, considering all possible events, the percentage of duration of the cooling events is larger than the mechanical events. Comparing these same relationships in Tables 5-13 and 5-14 shows the importance of the larger events to the upper ocean evolution. The general trend is for the larger mechanical events to remain significant while the larger cooling events become less important. For example the cooling events with $P_k \geq 2.0$ are almost insignificant. The exception to this trend is OWS V. It should be observed in Tables 5-13 and 5-14 that for $P_k \geq 1.5$ ΔSST is only 31% at OWS V, and for $P_k \geq 2.0$ ΔSST is reduced to only 22%. These percentages are significantly smaller than at OWS P and OWS N. It was noted previously that the intensification of the atmospheric forcing does not occur until November at OWS V. Therefore it is possible that the large events ($P_k \geq 1.5$) occur later in the season at OWS V and this would account for the smaller sea-surface temperature response. Before discussing the characteristics of the events one additional observation may be made by comparing u_*^3 and Q_n during the mechanical events in the three tables. At OWS P and OWS V, the percentage of u_*^3 is consistently larger than Q_n

while at OWS N it is consistently smaller. This is additional evidence that the surface cooling at OWS N is more closely coupled to the wind at OWS N than at OWS P and OWS V.

The final part of this analysis was to determine the principal characteristics of the large events. The final three quantities (number of events/month, duration of the events, and peak-to-mean ratio) will demonstrate that the character of the events is very similar at OWS P and OWS V but quite different at OWS N. In fact these quantities support the hypothesis that these events are directly related to the properties of the large winter storms at OWS P and OWS V, while they are related to changes in the mean circulation at OWS N. Table 5-12 shows that the average number of mechanical and cooling events is largest at OWS P and smallest at OWS N. At all stations a larger number of mechanical events occur than cooling events but have a shorter duration and a larger peak-to-mean ratio. However it is important to observe that, for the mechanical events, the duration and Pk (mean and standard deviation) are very similar at OWS P and OWS V and noticeably different at OWS N. This becomes even more apparent for the larger events as may be seen in Tables 5-13 and 5-14. The larger mechanical events at OWS P and OWS V appear to be well organized on time scales of 2-3 days, have similar Pk, and occur at the same frequency each month. These large events at OWS N however, occur less frequently, are of longer duration, and exhibit a very large and variable peak-to-mean ratio. These are exactly the nature of the statistics that would be expected if the events at OWS P and OWS V were directly associated with the passage of extratropical cyclone systems. The statistics at OWS N are compatible with the presumption that the events are related to a pulsing of the mean circulation.

The important implication from this analysis is that these large events occur frequently during the fall and winter at all stations. Furthermore they play a significant role in determining the characteristic evolution of the upper ocean thermal structure. Therefore they deserve special attention in any prediction scheme that attempts to reproduce this evolution.

VI. CONCLUSIONS

The principal objective of this research was to examine the upper ocean thermal structure modifications that take place in response to strong atmospheric forcing events during the fall and early winter cooling seasons. The motivation was the fact that there was a serious gap in our fundamental knowledge regarding the role that these strong events play in the total thermal structure evolution during the fall and early winter.

The one-dimensional hypothesis was evaluated at the three North Pacific Ocean weather stations using modified versions of the Kraus and Turner (1967), Kim (1976), and Elsberry, et al. (1976) models. The performance of the three models was evaluated using 49 independent data sets from the historical series of marine observations at OWS P, OWS N, and OWS V. Additionally the EFT model was used to isolate and examine the relative importance of the principal one-dimensional mechanisms at the three stations. Finally, the large body of surface and near-surface marine observations were examined at the three North Pacific Ocean weather stations. A new analysis technique was employed to determine the relative importance of strong atmospheric forcing events in the total fall and early winter thermal structure modifications at these stations. From the analysis the following significant conclusions were drawn.

1. The integrated effect of the strong fall and winter atmospheric forcing events is the dominant factor in the modification of the upper ocean thermal structure at OWS P, OWS N, and OWS V. For example, these strong events occurred during approximately 35% of the time at the three

ocean weather stations. However, 85%/68%/57% of the sea-surface temperature change at OWS N/OWS P/OWS V occurred during these periods. Observations from the individual data sets indicate that one can expect similar responses for mixed layer depth changes. It was therefore concluded that these strong events can not be excluded from any forecast scheme developed to simulate upper ocean response during the cooling season.

2. The response of the upper ocean during the strong events investigated in this study was largely one-dimensional. Additionally, a modified version of the EFT model consistently demonstrated better agreement with observations than either the KT or KIM models. The KT model consistently predicted mixed-layer temperature and depth changes which were much larger than the observations. This result suggests that the fraction of turbulent kinetic energy that is available for entrainment is not a constant fraction of the turbulent kinetic energy transferred to the ocean by the wind, as postulated by Turner (1969). The superior performance of the EFT and KIM models relative to the KT model suggests that the amount of wind-generated turbulent kinetic energy arriving at the mixed layer interface decreases as the mixed-layer depth increases. However, the exponential parameterization of dissipation enhancement employed in the EFT model was found to be more effective in preventing excessive deepening rates than the linear representation in the KIM model. It was further concluded that the convectively-generated turbulent kinetic energy is largely non-penetrative, in agreement with Gill and Turner (1976).

3. During these strong forcing events a large component of the sea-surface temperature change is due to the vertical fluxes of heat at the surface and at the base of the deepening mixed layer. Depending on the magnitude of the turbulent fluxes of kinetic energy, the heat exchanged

at the air-sea interface, and the depth of the mixed layer, either of these heat fluxes may dominate the local heat budget of the mixed layer. However the important conclusion that may be drawn from this research is that an accurate specification of both fluxes is essential to understanding and predicting the sea-surface temperature changes. The effect of entrainment mixing is most evident during early season events when the sea-surface temperature decreases while the net surface heat flux is downward. This means that a forecast scheme must be capable of predicting the changes in the mixed layer depth to predict the sea-surface temperature evolution.

4. The data sets examined in this study suggest that at OWS P the large forcing events are largely dominated by mechanical mixing. This is evidenced by the entrainment heat flux exceeding the surface heat flux, and the increase of potential energy of the upper ocean. At OWS V and OWS N, however, the large majority of the cases showed that the strong forcing events are dominated by the convective process.

5. The adequacy with which the EFT model simulated the evolution during these strong events suggests that a properly parameterized turbulent bulk model will be useful for predicting the thermal structure changes over a period of a few weeks. Even during periods when non-local processes were important, the EFT model was capable of predicting changes in the thermal gradient. This property should be useful for estimating the changing acoustic properties of the upper ocean due to storm activity.

6. In agreement with the findings of Dorman (1974) the modeling of data sets at OWS N and OWS V suggests that the inclusion of salinity effects may not be necessary to simulate the upper ocean thermal structure changes in the subtropics. Moreover, the results at OWS P suggest that a model that neglects salinity effects is capable of simulating the

changes in the temperature structure during the early cooling season in the subarctic region as well.

7. The examination of the seasonal trends in the mixed layer evolution suggests that a large percentage of the changes are understandable in terms of one-dimensional processes. Additionally, the capability of the modified EFT model to simulate layer retreat suggests that it should be useful for simulating thermal structure changes during the spring and summer heating seasons.

8. The examination of the forcing terms showed that the distribution of the marine winds and turbulent heat fluxes are non-Gaussian at the three ocean weather stations. The analysis showed that although the magnitude of the mechanical forcing is largest at OWS P and smallest at OWS N, its frequency distribution is similar at all stations. The distribution of the turbulent heat fluxes were similar at OWS P and OWS V, but different at OWS N. It was demonstrated that this is related to the fact that the large forcing events at OWS P and OWS V are very similar and are closely correlated to the extratropical cyclones that pass in close proximity to these two stations. At OWS N, however, cyclone activity is rare and the events are related to a pulsing of the mean flow. This pulsing is probably due to a strengthening of the north-south pressure gradient as the large storms pass north of OWS N.

9. The final conclusion is that the timing of the large fall and winter events and the characteristics of the underlying thermal structure are important to the seasonal evolution of the upper ocean. It was demonstrated that the strong forcing events that occur early in the cooling season result in a much larger mixed layer response than comparable events occurring later in the season. This is because less turbulent

kinetic energy is available for entrainment when the layer is deep (dissipation enhancement). It was further demonstrated that changes in the mixed layer will be quite different depending on the strength of the thermocline. cursory examination of records from OWS P suggests that the strength or weakness of the seasonal thermocline depends on the characteristics of the forcing during the spring and summer heating season. It is possible, therefore, that the large forcing events are equally important in the formation of the thermocline, during the spring and summer, as they are in its subsequent erosion during the fall and winter. It is recommended that future research be conducted during the spring and summer periods to demonstrate the role of strong events during these seasons.

APPENDIX A
COMPUTATIONAL FORMULAS FOR SURFACE FORCING

A. RADIATIVE FLUXES AT THE SEA SURFACE

The heat gained or lost by the oceans at the air-sea interface by radiant energy falls into two spectral regions. The first, ranging from 0.1 to 4 microns (10^{-4} cm), is the short wave radiation received from the sun. The long wave, 4 to 50 microns, is commonly known as the back radiation and represents a net loss of heat from the ocean to the atmosphere or space. These two spectral ranges are virtually exclusive, thus permitting computations of these radiative fluxes to be performed separately.

A number of empirical formulas are available for computing the insolation arriving at the sea surface and Reed (1975) has reviewed and evaluated the most commonly used expressions. Reed found that results obtained from the formula developed by Seckel and Beaudry (1973), were consistently in better agreement with data collected at five coastal stations. Therefore this expression is used to calculate the clear-sky radiation (Q_0) in this study.

$$Q_0 = A_0 + A_1 \cos \phi + B_1 \sin \phi + A_2 \cos 2\phi + B_2 \sin 2\phi \quad (A-1)$$

where Q_0 is in langley (ly) per day,

$$\phi = \frac{2\pi}{365} (t-21) ,$$

and t is the julian day of the year. The coefficients (A_0 , etc.) were calculated by a harmonic representation of the values presented in the

Smithsonian Meteorological Tables (List, 1958). This clear-sky value must be corrected for the presence of clouds and reflection from the sea surface. Gunter Seckel (personal communication) has suggested that the cubic cloud correction of Laevastu (1960) and a reflection coefficient modeled after Anderson (1952) are suitable at the ocean stations. Therefore,

$$Q_s = Q_o K (1 - R) \quad (A-2)$$

calculates the solar energy penetrating the air-sea interface and

$$K = 1 - .66 C^3$$

$$R = a \alpha^b$$

The coefficient C is the total observed cloud cover (in tenths) and α is the mid-day elevation angle of the sun. The constants, a and b , are adopted from Tabata (1964), and for $C < 0.5$, $a = 0.33$ and $b = -0.42$, while for $C \geq 0.5$, $a = 0.21$ and $b = -0.29$.

The largest source of error in (A-2) is the parameterization of the effects of cloud cover and the subjectivity involved in observation. Moreover, the application of this expression for averages less than mean monthly values introduces another possible source of error, as discussed by Reed and Halpern (1975). In this research (A-2) was used to estimate Q_s on a daily basis with C taken as the mean cloud cover during the daytime.

The net long wave radiation (Q_b) is a function of the radiation emitted from the sea surface to the atmosphere, minus the energy radiated from the air mass and absorbed by the ocean. Both of these quantities depend upon the fourth power of the absolute temperature of the emitting

body (Stephan Boltzman Law) with suitable correction factors for cloud cover and vapor content of the atmosphere. A representative formula reported by Husby and Seckel (1975) is

$$Q_b = 1.14 \times 10^{-7} (273.16 + T_s)^4 (0.39 - 0.05 \sqrt{E_a}) (1 - 0.6C^2) \quad (A-3)$$

where Q_b is in ly/day, T_s is the sea-surface temperature ($^{\circ}\text{C}$), and E_a is the saturated vapor pressure of the atmosphere (at a height of 10 m) in millibars. This vapor pressure was calculated using the Goff-Gratch (1946) formulation of the Clausius-Clapeyron equation, using the dew point temperature (T_d) as the entering argument. Equation (A-3) is the modified Brunt (1932) formula with the empirical constants of Budyko (1956), and the largest uncertainties are introduced through the cloud correction factor and the use of overland constants.

B. TURBULENT FLUXES OF HEAT AND MOMENTUM

The turbulent fluxes of latent heat (Q_e), sensible heat (Q_h), and momentum (τ_s) at the air-sea interface were represented by the so-called bulk aerodynamic formulas.

$$\tau_s = \rho_a C_D (\bar{u}_a \times 10^2) \text{ (dynes/cm}^2\text{)} \quad (A-4)$$

$$Q_e = 3,767 C_D (0.98 E_s - E_a) \bar{u}_a \text{ (ly/day)} \quad (A-5)$$

$$Q_h = 2,488 C_D (T_s - T_a) \bar{u}_a \text{ (ly/day)} \quad (A-6)$$

where \bar{u}_a is the mean wind speed (m/sec), T_a is the air temperature ($^{\circ}\text{C}$), E_s is the saturated vapor pressure of the marine air directly in contact with the sea surface (0.98 corrects for salt effects), and C_D is the non-dimensional drag coefficient. A constant drag coefficient

(1.3×10^{-3}) is used in all computations in this thesis and is consistent with the range of values reported in the literature.

The accuracy of these expressions has been the subject of many detailed studies and the main sources of error are the underlying assumptions of a neutrally stable atmosphere and constant and equal exchange coefficients (moisture, momentum, and heat). Businger, et al. (1971), from overland values, and Paulson, et al. (1972), from data collected at sea, have demonstrated that the moisture and heat coefficients are nearly equal but quite different from the coefficients of momentum exchange. Furthermore, studies by Deardorff (1968), DeLeonibus (1971), and Davidson (1974) have found that these coefficients are very dependent on the stability of the marine boundary layer and the roughness of the sea surface. Nevertheless, they afford the only practical means for computing these fluxes, using the meteorological observations available in the ocean weather station file, and are used throughout this research.

APPENDIX B

THE NUMERICAL SCHEME FOR THE ONE-DIMENSIONAL TURBULENT BULK MODELS

A simple numerical scheme was developed which is capable of incorporating the various assumptions of the Kraus-Turner (1967), Elsberry, et al. (1976), and Kim (1976) models in a consistent manner. This routine is a modification of the algorithm presented by Thompson (1976), and is designed to calculate the potential energy modifications due to the vertical fluxes of heat and turbulent kinetic energy.

The NODC mechanical bathythermographs that were used to initialize and validate the models were digitized in five meter increments starting at the sea-surface. In the model, this temperature profile is stored in N equally-spaced grid intervals $[-(n-1)\Delta Z, -n\Delta Z]$, where $n=1,2,\dots,N$, and $\Delta Z = 2.5$ m. For a profile in which the temperature is well mixed to a depth of $-n\Delta Z$, the first n -values of T are equal to T_1 . During initialization it was assumed that the temperature varied linearly with depth in each five meter increment in the BT profile, and the model profile was chosen to conserve the heat content of the BT profile.

In the model the potential energy (PE) per unit area may be expressed as

$$PE = -\rho_0 g \alpha \int_{-D}^0 T dz \quad (B-1)$$

where D is a depth which is deeper than the maximum penetration of the vertical turbulent processes (typically the deepest level in the model). If non-local processes are small relative to the vertical fluxes, and if density changes due to salinity changes can be ignored, and α is

constant, changes in the potential energy calculated by (B-1) will be representative of the changes in the potential energy per unit area of the ocean.

After mixing the top n grid intervals a further mixing of the layer to a depth $-(n+1)\Delta Z$ will result in a change in potential energy (ΔPE) of the column by

$$\Delta PE(n) = \frac{1}{2} \rho_o g n (\Delta Z)^2 (T_n - T_{n+1}) \quad (B-2)$$

For $T_n - T_{n+1} > 0$, this mixing increases the potential energy and $\Delta PE_m(n)$ will represent the amount of turbulent kinetic energy that must be expended to accomplish the mixing. However, if the column is unstable ($T_n - T_{n+1} < 0$), this mixing will release potential energy, and $\Delta PE_c(n)$ will represent the turbulent kinetic energy generated by free convection.

At the beginning of each time step ($\Delta t = 1$ hr) the surface heat fluxes are added to obtain

$$T_1(t+\Delta t) = T_n(t) + \Delta t [Q_a(t^*) + Q_s(0, t^*) - Q_s(\Delta Z, t^*)] / \rho_o C_p \quad (B-3)$$

$$T_n(t+\Delta t) = T_n(t) + \Delta t [Q_s(-n\Delta Z, t^*) - Q_s(-(n+1)\Delta Z, t^*)] / \rho_o C_p \quad (B-4)$$

for $n=2, 3, \dots, N$, and $t^* = t + \frac{1}{2} \Delta t$. The effective insolation (Q_s) was distributed by assuming 50% absorption in the first meter and the remainder taken to decay as $\exp(-\gamma Z)$. The average extinction coefficient (γ) was assumed constant at 0.003 cm^{-1} , which is the value used by Denman and Miyake (1973). If the resulting temperature profile is unstable ($T_1 < T_2$) the first two intervals are mixed and the resulting turbulent kinetic energy (ΔPE_c) generated by the convection is calculated according

to (B-1). This process continues until a stable temperature profile is established ($T_k > T_{k+1}$) and the upper layer is isothermal to a depth $Z = -k\Delta Z$. At the end of this evolution the potential energy of the column will be reduced by

$$\sum_{n=1}^{k-1} \Delta PE_C(n), \quad (B-5)$$

which is also equal to the total generation of turbulent kinetic energy by free convection.

Further mixing will require an expenditure of turbulent kinetic energy.

The algorithm must also be modified to account for dissipation enhancement (EFT and KIM), the storage of turbulent kinetic energy (KIM), and the fraction of convectively generated turbulent kinetic energy that is utilized for entrainment (KT, EFT, and KIM). We start by defining the total amount of turbulent kinetic energy, $E_T(n)$, available for mixing the first n levels with level $n+1$ as

$$E_T(n) = E_m(n) + E_C - E_p(n) - E_s(n) \quad (B-6)$$

The mechanically generated turbulent kinetic energy is $E_m(n)$; E_C is the fraction of (B-5) available for entrainment, $E_p(n)$ is the amount of turbulent kinetic energy previously expended to mix the layer to level n , and $E_s(n)$ is the amount of turbulent kinetic energy that is stored as the layer deepens to a depth $-n\Delta Z$.

For the KIM model,

$$E_m(n) = (1.25 \rho_o w_*^3(t^*) - \rho_o D_b n \Delta Z) \Delta t, \quad (B-7)$$

where D_b is a constant background dissipation equal to $2 \times 10^{-4} \text{ cm}^2 \text{ sec}^{-3}$. For the KT and EFT models,

$$E_m(n) = [\rho_o w_*^3(t^*) \exp(-n\Delta Z/Z)] \Delta t, \quad (\text{B-8})$$

with

$$Z = \begin{cases} \infty & \text{for KT} \\ 50 \text{ m} & \text{for EFT} \end{cases} \quad (\text{B-9})$$

Therefore (B-7), (B-8), and (B-9) express the depth dependence of dissipation (dissipation enhancement) formulated by Kim (1976) and Elsberry, et al. (1976). In the Kraus and Turner (1967) model dissipation is neglected, and the amount of surface production, $\rho_o w_*^3(t^*)$, available for mixing is independent of depth.

Further,

$$E_c = -r \sum_{n=1}^{k-1} \Delta PE_c(n) \quad (\text{B-10})$$

where r is the fraction of the convectively generated turbulent kinetic energy utilized for entrainment. In all models used in this study $r = .15$ following Gill and Turner (1976). Therefore the KT model here is equivalent to a modified version discussed by Gill and Turner (1976).

Finally,

$$E_p(n) = \sum_{i=k}^{n-1} \Delta PE_m(i), \quad (\text{B-11})$$

$$\text{and } E_s = \begin{cases} \sum_{i=l}^{n-1} 4.5 \rho_0 \Delta Z w_*^3(t^*), \text{ for KIM} \\ 0, \text{ for KT and EFT} \end{cases} \quad (\text{B-12})$$

Thus (B-11) is used to calculate the turbulent kinetic energy expended to deepen the layer from the free-convection depth to $-n\Delta Z$. For KIM, (B-12) calculates the amount of turbulent kinetic energy stored as the mixed layer deepens beyond the mixed layer depth of the previous time step [i.e., $l\Delta Z(t+\Delta t) > h(t)$].

If $E_T(n) \geq \Delta PE_m(n)$, there is enough energy to mix T through T_{n+1} . If there is insufficient energy to mix completely, $E_T(n) < \Delta PE_m(n)$, then we follow Thompson (1976) and partially mix; i.e., set

$$a = \frac{nE_T(n)}{(n+1)\Delta PE_m(n)}$$

$$\bar{T} = [aT_{n+1} + (n-a)T_n]/n$$

$$\bar{T}' = aT_n + (1-a)T_{n+1}$$

then set $T_i = \bar{T}$, for $i=1,2,\dots,n$, $T_{n+1} = \bar{T}'$. The mixed-layer temperature at each time step is equal to T_1 , but since the algorithm does not calculate the mixed layer depth, it is defined as the depth at which the temperature is 0.2°C less than T_1 .

The relative importance of mechanical mixing and free convection to the evolution of the mixed layer were investigated by comparing the relative contribution of ΔPE_m and ΔPE_c to ΔPE . An important part of this study was to quantify the relative magnitudes of the surface and entrainment heat fluxes. The surface heat fluxes were calculated, as

described in Appendix A, from the surface marine observations. The entrainment heat flux ($-\Lambda \frac{\partial h}{\partial t} \Delta T$) was calculated, in the models, as the heat gained by the profile (during each time step) in levels $n+1$ to $n+m$ as the mixed layer deepens between levels n and $n+m$.

BIBLIOGRAPHY

1. Anderson, E. R., 1952: Energy budgets studies. Water loss studies: Volume I, Lake Hefner studies. U. S. Navy Electron Lab., Tech. Rep. 327, pp. 71-112.
2. Brunt, D., 1932: Notes on radiation in the atmosphere. Meteorol. Soc. Lond., 58, 389-420.
3. Budyko, M. I., 1956: The heat balance of the earth's atmosphere. (Teplovoi balans zemnoi poverkhuosti) Gidrometeorologicheskoe izdatel'stvo, Leningrad, 255 p.
4. Businger, J. A., J. C. Wyngaard, Y. Izumi, and E. F. Bradley, 1971: Flux-profile relationships in the atmospheric surface layer. J. Atmos. Sci., 28, 181-189.
5. Davidson, K. L., 1974: Observational results on the influence of stability and wind-wave coupling on momentum transfer and turbulent fluctuations over ocean waves. Boundary-Layer Meteorol., 6, 305-331.
6. Deardorff, J. W., G. E. Willis, and D. K. Lilly, 1969: Laboratory investigations of nonsteady penetrative convection. J. Fluid Mech., 35, 7-31.
7. Deardorff, J. W., 1968: Dependence of air-sea transfer coefficients on bulk stability. J. Geophys. Res., 73, 2545-2577.
8. DeLeonibus, P. S., 1971: Momentum flux and wave spectra observations from an ocean tower. J. Geophys. Res., 76, 6506-6527.
9. Denman, K. L., 1973: A time-dependent model of the upper ocean. J. Phys. Oceanogr., 3, 173-184.
10. Denman, K. L., and M. Miyake, 1973: Upper layer modifications at ocean station PAPA: Observations and simulations. J. Phys. Oceanogr., 3, 185-196.
11. Dorman, C. E., 1974: Analysis of Meteorological and Oceanographic Data from Ocean Station Vessel N (30N 140W). Ph.D. thesis, Oregon State University, 136 pp.
12. Elsberry, R. L., T. S. Fraim, and R. N. Trapnell, 1976: A mixed layer model of the oceanic thermal response to hurricanes. J. Geophys. Res., 81, 1153-1162.
13. Farmer, D. M., 1975: Penetrative convection in the absence of mean shear. Quart. J. R. Met. Soc., 101, 869-891.
14. Gill, A. E., and J. S. Turner, 1976: A comparison of seasonal thermocline models with observations. Deep-Sea Res., 23, 391-401.

15. Gill, A. E., and P. P. Niiler, 1973: The theory of the seasonal variability in the ocean. Deep-Sea Res., 20, 141-177.
16. Goff, J. A., and S. Gratch, 1946: Trans. Amer. Soc. Heat. and Vent. Eng., Vol. 52, p. 95.
17. Grant, H. L., A. Moilliet, and W. M. Vogel, 1968: Some observations of the occurrence of turbulence in and above the thermocline. J. Fluid Mech., 34, 443-448.
18. Halpern, D., 1974: Observations of the deepening of the wind-mixed layer in the northeast Pacific Ocean. J. Phys. Oceanogr., 4, 454-466.
19. Haney, R. L., and R. W. Davis, 1976: The role of surface mixing in the seasonal variation of the ocean thermal structure. J. Phys. Oceanogr., 6, 504-510.
20. Husby, D. M., and G. R. Seckel, 1975: Large-Scale Air-Sea Interactions at Ocean Weather Station V, 1951-1971, NOAA Tech. Rep. NMFS SSRF-696, 44 pp.
21. Jerlov, N. G., 1968: Optical Oceanography, Elsevier Publishing Co., New York, 194 pp.
22. Kraus, E. B., and J. S. Turner, 1967: A one-dimensional model of the seasonal thermocline, II. The general theory and its consequences. Tellus, 19, 98-106.
23. Kato, H., and O. M. Phillips, 1969: On the penetration of a turbulent layer into a stratified fluid. J. Fluid Mech., 37, 643-655.
24. Kitaigorodsky, S. A., 1960: On the computation of the thickness of the wind-mixed layer in the ocean. Bull. Acad. Sci. U.S.S.R., Geophys. Ser., 7, 284-287.
25. Kim, J. W., 1976: A generalized bulk model of the oceanic mixed layer. J. Phys. Oceanogr., 6, 686-695.
26. Niiler, P. P., 1975: Deepening of the wind-mixed layer. J. Marine Res., 33, 405-422.
27. Paulson, C. A., E. Leavitt, and R. G. Fleagle, 1972: Air-sea transfer of momentum, heat, and water determined from profile measurements during BOMEX. J. Phys. Oceanogr., 2, 487-497.
28. Pollard, R. T., P. B. Rhines, and R.O.R.Y. Thompson, 1973: The deepening of the wind-mixed layer. Geophys. Fluid Dyn., 3, 381-404.
29. Pollard, R. T., 1970: On the generation by winds of inertial waves in the ocean. Deep Sea Res., 17, 795-812.

30. Pollard, R. T., and R. C. Millard, Jr., 1970: Comparison between observed and simulated wind-generated inertial oscillations. Deep-Sea Res., 17, 813-821.
31. Reed, R. K., 1975: An evaluation of formulas for estimating clear-sky insolation over the ocean. NOAA Tech. Rept. ERL 352-PMEL26, 25 pp.
32. Reed, R. K., and D. Halpern, 1975: Insolation and net long-wave radiation off the Oregon coast. J. Geophys. Res., 80, 839-844.
33. Seckel, G. R., and F. H. Beaudry, 1973: The radiation from sun and sky over the North Pacific Ocean. (Abstract O-33) EOS, Trans. Am. Geophys. Union, 54:1114.
34. Simpson, J., 1969: On some aspects of sea-air interaction in middle latitudes. Deep-Sea Res., Suppl. to Vol. 16, 233-261.
35. Stull, R. B., 1975: Temperature inversions capping atmospheric boundary layers. Ph.D. thesis, University of Washington.
36. Sverdrup, H. V., M. W. Johnson, and R. H. Fleming, 1942: The Oceans Their Chemistry, Physics, and General Biology. Prentice-Hall, New York, 1087 pp.
37. Tabata, S., 1964: A study of the main physical factors governing the oceanographic conditions of station P in the northeast Pacific Ocean, Doctor, Sci. thesis, Univeristy of Tokyo, 264 p.
38. Thompson, S. M., and J. S. Turner, 1975: Mixing across an interface due to turbulence generated by an oscillating grid. J. Fluid Mech., 64, 349-367.
39. Thompson, R.O.R.Y., 1976: Climatological numerical models of the surface mixed layers of the ocean. J. Phys. Oceanogr., 6, 496-503.
40. Townsend, A. A., 1968: Excitation of internal waves in a stably-stratified atmosphere with considerable wind-shear. J. Fluid Mech., 32, 145-171.
41. Tully, J. P., 1964: Oceanographic regions and assessment of temperature structure in the seasonal zone of the North Pacific Ocean, 21(5), 941-970.
42. Turner, J. S., and E. B. Kraus, 1967: A one-dimensional model of the seasonal thermocline, I. A laboratory experiment and its interpretation. Tellus, 19, 88-97.
43. Turner, J. S., 1969: A note on wind mixing at the seasonal thermocline. Deep-Sea Res., Suppl. to Vol. 16, 297-300.
44. Turner, J. S., 1973: Buoyancy Effects in Fluids, Cambridge University Press, London, 367 pp.

INITIAL DISTRIBUTION LIST

	No. Copies
1. Defense Documentation Center Cameron Station Alexandria, Virginia 22314	2
2. Library (Code 0142) Naval Postgraduate School Monterey, California 93940	2
3. Department of Oceanography, Code 68 Naval Postgraduate School Monterey, California 93940	3
4. Department of Meterology, Code 63 Naval Postgraduate School Monterey, California 93940	1
5. Oceanographer of the Navy Hoffman Building No. 2 200 Stovall Street	1
6. Office of Naval Research Code 410 NORDA, NSTL Bay St. Louis, Mississippi 39520	1
7. Dr. Robert E. Stevenson Scientific Liaison Office, ONR Scripps Institution of Oceanography La Jolla, California 92037	1
8. Library, Code 3330 Naval Oceanographic Office Washington, D. C. 20373	1
9. SIO Library University of California, San Diego P. O. Box 2367 La Jolla, California 92037	1
10. Department of Oceanography Library University of Washington Seattle, Washington 98105	1
11. Department of Oceanography Library Oregon State University Corvallis, Oregon 97331	1

- | | | |
|-----|---|---|
| 12. | Commanding Officer
Fleet Numerical Weather Central
Monterey, California 93940 | 1 |
| 13. | Commanding Officer
Naval Environmental Prediction Research Facility
Monterey, California 93940 | 1 |
| 14. | Department of the Navy
Commander Oceanographic System Pacific
Box 1390
FPO San Francisco 96610 | 1 |
| 15. | Director
Naval Oceanography and Meteorology
National Space Technology Laboratories
Bay St. Louis, Mississippi 39520 | 1 |
| 16. | NORDA
Bay St. Louis,
Mississippi 39520 | 1 |
| 17. | Assoc, Prof. R. L. Elsberry, Code 63Es
Department of Meteorology
Naval Postgraduate School
Monterey, California 93940 | 5 |
| 18. | Lcdr N. T. Camp, USN
Staff, Commander Fleet Air Mediterranean
FPO New York 09521 | 3 |
| 19. | Professor C. Comstock, Code 53Zk
Department of Mathematics
Naval Postgraduate School
Monterey, California 93940 | 1 |
| 20. | Assoc. Prof. E. B. Thornton, Code 68Tn
Department of Oceanography
Naval Postgraduate School
Monterey, California 93940 | 1 |
| 21. | Assoc. Prof. R. L. Haney, Code 63Hy
Department of Meteorology
Naval Postgraduate School
Monterey, California 93940 | 1 |
| 22. | Asst. Prof. R. H. Bourke, Code 68Bf
Department of Oceanography
Naval Postgraduate School
Monterey, California 93940 | 1 |

- | | | |
|-----|---|---|
| 23. | Professor G. H. Jung, Code 68Jg
Department of Oceanography
Naval Postgraduate School
Monterey, California 93940 | 1 |
| 24. | Assoc. Prof. W. Denner, Code 68Ds
Department of Oceanography
Naval Postgraduate School
Monterey, California 93940 | 1 |
| 25. | Adjunct Asst. Prof. R. W. Garwood, Code 68Gd
Department of Oceanography
Naval Postgraduate School
Monterey, California 93940 | 1 |
| 26. | Mr. Gunter Seckel
National Marine Fisheries
Monterey, California 93940 | 1 |